7-8-2009

Time dependent non-extinction probability for fast burst reactors

Michael Gregson

Michael W. Gregson
Candidate

Chemical and Nuclear Engineering
Department

This dissertation is approved, and it is acceptable in quality and form for publication on microfilm:

Approved by the Dissertation Committee:

, Chairperson

Anil K. Prinja

Gary W. Cooper

Evangelos A. Coutsias

Taro Ueki

Accepted:

Dean, Graduate School

Date

TIME DEPENDENT NON-EXTINCTION PROBABILITY FOR FAST BURST REACTORS

BY

MICHAEL W. GREGSON

B.S., Mechanical Engineering, University of Texas at Austin, 2001
M.S., Engineering, University of Texas at Austin, 2003.

DISSERTATION

Submitted in Partial Fulfillment of the
Requirements for the Degree of

Doctor of Philisophy
Engineering

The University of New Mexico
Albuquerque, New Mexico

May 2009

DEDICATION

To my MG's that supported and bore the burden of this work. May the hours spent on this work enrich all of our lives. Thanks are given to those who provided the inspiration, encouragement, and the confidence necessary for me to complete this work. Finally much appreciation to the Almighty for opening the necessary windows such that this work could be completed and for giving me the perseverance to see it to completion.

ACKNOWLEDGEMENTS

Sandia National Laboratories - Sandia Educational Assistance Program

Radiation Sciences Center

Matt Burger

Dick Coats

Phil Cooper

Jim Dahl

Sid Dominguez

Mike Folsom

John Ford

Autumn Higgins

Ed Parma

Curtis Peters

Ken Reil

TIME DEPENDENT NON-EXTINCTION PROBABILITY FOR FAST BURST REACTORS

BY

MICHAEL W. GREGSON

ABSTRACT OF DISSERTATION

Submitted in Partial Fulfillment of the
Requirements for the Degree of

Doctor of Philisopy
Engineering

The University of New Mexico
Albuquerque, New Mexico

May 2009

TIME DEPENDENT NON-EXTINCTION PROBABILITY FOR FAST BURST REACTORS

by

Michael W. Gregson

B.S., MECHANICAL ENGINEERING

M.S., ENGINEERING

Ph. D., ENGINEERING

ABSTRACT

Sandia National Laboratories has successfully operated fast burst reactors over the past four decades. Fast burst reactors refer to a type of reactor that is able to achieve intense neutron pulses in very short periods of time using fissile material. Typically these systems are comprised of enriched metallic uranium fuel. During operation of a fast burst reactor, a phenomena known as a pre-initiation has been known to take place. A pre-initiation occurs when the neutron population exceeds some fiducial prior to achieving the final reactivity state in a pulse operation. Reactivity is determined from the physical configuration of the reactor and governs the average neutron population behavior. The purpose of this study is to examine the probability of initiation (or the pre-

initiation probability) for a fast burst type of system, with emphasis on the Sandia Pulse Reactor-III (SPR-III) for physics parameters. The magnitude of the pre-initiation problem for SPR-III was examined to establish the magnitude of the phenomena. This work focuses on developing and numerically solving an equation that describes the non-extinction probability in a prompt critical assembly when the population is so low that it deviates from the average behavior.

A zero dimensional (0-D) model is derived to describe the neutron non-extinction probability in a system where the reactivity is changing as a function of time. Analytical solutions to the model are provided where solutions could be found. Numerical solutions were obtained for a variety of cases applicable to fast burst reactor operation. Use of 0-D Monte Carlo techniques is also presented as a means to examine the low population stochastic behavior and for comparison to the deterministic solution. The 1-D time dependent equation for slab geometry was evaluated to highlight the importance of neutron leakage. The non-extinction probability equation was solved using a modified form of the standard fixed point iteration method. Other iteration techniques were also analyzed. Particular emphasis was extended to a linearized routine since the performance can be analyzed analytically and it allows for development of acceleration techniques. An accelerated routine was then developed and analyzed. The numerical performance between the iteration routines was thoroughly investigated. The impact of the acceleration routine on the iteration count and the associated decrease in runtime was evaluated.

TABLE OF CONTENTS

LIST OF FIGURES ..... **xi**
LIST OF TABLES ..... **xiii**
LIST OF TABLES ..... **xiii**
CHAPTER 1: INTRODUCTION **1**
1.1 Definitions 5
CHAPTER 2: MOTIVATION AND DATA **8**
2.1 Sandia Pulse Reactor-III 12
2.2 SPR-III Background 12
2.3 Background Neutron Sources 16
2.4 Nuclear Data 18
CHAPTER 3: THEORY **20**
3.1 Stochastic Behavior 21
3.2 Point Model Derivation 23
3.2.1 Forward Equation 23
3.3 Fission Multiplicity Constants 30
3.4 Solutions for $P_N(t)$ Invoking the Quadratic Approximation 31
3.4.1 Zero Source 32
3.4.2 Probability of N neutrons 33
3.4.3 Constant Source 36
3.4.4 Probability of N neutrons 38
3.5 Dynamic Reactivity Insertions 42
3.6 Backward v. Forward 43
3.6.1 Backward Equation 45
CHAPTER 4: NUMERICAL MODELING – 0-D **51**
4.1 Examination of Non-Linear Terms 52
4.2 0-D Iteration Routine 56
4.3 Zero Source - Static Reactivity 58
4.3.1 Timestep Analysis 60
4.3.2 Analytical v Numerical Solution 62
4.4 Zero Source - Dynamic Reactivity 67
4.4.1 Analytical v Numerical Solution 67
4.4.2 Dynamic Reactivity Results 70
4.5 Source Extension 72
4.6 Source Strength Examination 74
4.7 Pre-initiation Examination 78
4.8 Maximum Over-pulse Examination 81
CHAPTER 5: MONTE CARLO MODELING **86**
5.1 Background 86
5.2 Assessing Divergence 89
5.3 0-D Results 90
5.4 Divergent Chain Probability and Time to Divergence Data 93
5.4.1 Comparison to Deterministic Results 98
5.4.2 Determination of Divergent Chains 100

CHAPTER 6: 1-D NUMERICAL MODELING 104
6.1 Fixed Point Iteration Routine 108
6.2 Lagged Fission Fixed Point Routine 116
6.3 Linearized Lagged Fission Fixed Point Routine 118
6.3.1 Diffusion Synthetic Acceleration of Inners 120
6.4 1-D Verification Testing 122
6.4.1 Critical Slab Thickness 123
6.4.2 Infinite Medium Eigenvalue Comparisons 124
6.4.3 Importance of the Quadrature Order 126
CHAPTER 7: 1-D NUMERICAL RESULTS 128
7.1 Timestep Analysis 129
7.2 Importance of Slab Thickness 130
7.3 Linear vs. Adjoint Spatial Profile 135
7.4 Dynamic Reactivity: 138
CHAPTER 8: ITERATION PERFORMANCE 146
8.1 Fixed Point Iteration Routine 147
8.2 Outer Iteration Behavior 149
8.3 Lagged Fission Source Routine 149
8.4 Linearized Lagged Fission Source Routine 154
8.4.1 Spectral Radius – Linearized Routine 158
8.5 Accelerated Linearized Lagged Fission Source Routine 169
8.5.1 Spectral Radius – Accelerated Linearized Routine 177
8.5.2 Reflected Spectral Radius – Accelerated and Unaccelerated 182
8.6 1-D Numerical Performance 188
8.7 Simulation Time 193
8.8 Sources of Error 194
CONCLUSIONS 198
FUTURE WORK 200
LIST OF APPENDICES: 202
APPENDIX A: SPR OPERATIONS AND EXPERIMENT RECORDS 203
REFERENCES 218

LIST OF FIGURES

Figure 1: Graphical view of the SPR-III reactor. 13
Figure 2: Picture of the SPR-III reactor with the experiment shroud removed. 14
Figure 3: SPR-III operating history. 15
Figure 4: U-10 Mo Neutron cross-sections. 19
Figure 5: Comparison of solutions of the quadratic truncation for $P_N(t)$ for static reactivity. 34
Figure 6: Extinction and Non-extinction probability for static reactivity. 35
Figure 7: Comparison of solutions of the quadratic truncation for $P_N(t)$ for static supercritical reactivity with a weak source. 39
Figure 8: Comparison of solutions of the quadratic truncation for $P_N(t)$ for static supercritical reactivity with a strong source. 39
Figure 9: Extinction and non-extinction probability for a prompt critical system with a source. 41
Figure 10: Magnitude of the non-linear terms versus non-extinction probability. 54
Figure 11: Overall importance of the non-linear terms on the fission term. 55
Figure 12: Time dependent non-extinction probability for fixed reactivity. 59
Figure 13: Importance of timestep on time dependent solution. 61
Figure 14: Comparison of analytical and numerical results. 64
Figure 15: Steady state POI solution versus system reactivity. 65
Figure 16: Time dependent non-extinction probability for a step insertion. 68
Figure 17: Non-extinction probability for a ramp insertion v different insertion times. 71
Figure 18: 10¢ pulse in 0-D for bounding source strengths. 77
Figure 19: Source non-extinction probabilities for various pulses. 82
Figure 20: Maximum over-pulse applicable to SPR operations. 84
Figure 21: Monte Carlo results for the neutron population as a function of time. 91
Figure 22: Divergent chain probability comparing Monte Carlo results and Bell 94
Figure 23: Time to divergence v. arbitrary particle number. 95
Figure 24: Integral Monte Carlo results versus S_N results for $k_\infty = 1.0005$. 98
Figure 25: Integral Monte Carlo results for $k_\infty = 1.001$ for different divergence metrics. 101
Figure 26: Numerical eigenvalues for critical slab thicknesses. 123
Figure 27: Time dependent 0-D solution v. 1-D reflected solution. 125
Figure 28: Importance of quadrature order on the time dependent slab midpoint values. 126
Figure 29: Importance of timestep on time and spatially dependent solution. 129
Figure 30: Importance of slab size on the time dependent survival probability. 131
Figure 31: Non-extinction probability as a function of injection point, angle and time. 132
Figure 32: Spatially dependent non-extinction probability at different simulation times. 133
Figure 33: 1-D SS POI versus system multiplication factor. 134
Figure 34: Ratio of k-eigenvalue to non-linear transport solution for k=1.001. 136
Figure 35: Ratio of k-eigenvalue to non-linear transport solution for k=1.01. 137

Figure 36: Graphical depiction of reflector insertion in 1-D. 139
Figure 37: Dynamic reactivity insertion with external reflector element. 139
Figure 38: 2-D non-extinction probability contour plot of the injection point and angle at 10^{-7} sec. 140
Figure 39: 2-D non-extinction probability contour plot of the injection point and angle at 10^{-4} sec. 142
Figure 40: Time dependent non-extinction probability for the slab midpoint and reflector edge. 143
Figure 41: Source non-extinction probability for dynamic reactivity insertion. 145
Figure 42: Number of iterations per timestep for the source iteration routine with full multiplicity. 147
Figure 43: Outers per timestep seven term multiplicity lagged fission source routine, small timestep. 150
Figure 44: Outers per timestep seven term multiplicity lagged fission source routine, large timestep. 151
Figure 45: Outers to SS per timestep for the lagged fission source routine. 153
Figure 46: Outers per timestep seven term multiplicity linearized routine, large timestep, linearization about $p_0 = 2$ 155
Figure 47: Outers to SS per timestep for the linearized lagged fission routine linearization about $p_0 = 2$ 157
Figure 48: Iteration amplitude as a function of the wave number. 162
Figure 49: Spectral radius for different multiplicities and linearization constants with a large timestep. 164
Figure 50: Dispersion functions versus wave number for the accelerated scheme linearizing about $p_0 = 2$ 181
Figure 51: Iteration amplitude versus wave number for different linearization constants. 184
Figure 52: Spectral radius for the accelerated routine for different linearization constants. 185
Figure 53: Diffusion update breakdown. 186
Figure 54: Timestep requirement for acceleration surety. 187
Figure 55: Combined outers to SS for accelerated and unaccelerated cases linearizing about $p_0 = 2$ with full multiplicity. 189
Figure 56: Combined outers to SS for accelerated and unaccelerated cases linearizing about $p_0 = 2$ with quadratic truncation. 190
Figure 57: Error update in the first outer iteration vs. timestep. 192
Figure 58: Non-extinction probability comparison between the linearized and lagged iteration routine. 195
Figure 59: Pulse size v. time lag after assembly for free field conditions. 211
Figure 60: Normalized probability time lag after assembly v. reactivity state for free field conditions. 213
Figure 61: Pulse size v. time lag after assembly for experiments with a large repetition rate 215
Figure 62: 2-D contour plots of the time lag after assembly for various experiments. 216

LIST OF TABLES

Table 1: Spontaneous fission rates for uranium. 17
Table 2: Fission multiplicity data. 18
Table 3: Fission multiplicity constants. 31
Table 4: Comparison of numerical POI to infinite medium values. 66
Table 5: Source non-extinction probability at the reflector insertion time of 0.250 seconds. 83
Table 6: Calculated divergent chain data. 97
Table 7: Divergent chain probability for different divergence metrics. 102
Table 8: Performance of the inner iterations with and without acceleration. 121
Table 9: Importance of quadrature order on the calculated eigenvalue. 127
Table 10: Non-extinction probability after each timestep. 152
Table 11: Non-extinction probability after each timestep. 156
Table 12: Numerical and theoretical spectral radius over the first timestep. 166
Table 13: Spectral radius for multiple timesteps. 168
Table 14: Comparison of accelerated vs. unaccelerated results for reflecting boundary conditions when linearizing about $p_0 = 2$ 183
Table 15: Comparison of accelerated vs. unaccelerated results for reflecting boundary conditions when linearizing about $p_0 = p_\infty$. 183
Table 16: Computer runtime (sec) for small timestep cases full multiplicity. 193
Table 17: Computer runtime (sec) for large timestep cases full multiplicity. 194
Table 18: SS non-extinction probability from different iteration routines with a small timestep. 197
Table 19: SS non-extinction probability from different iteration routines with a large timestep. 197
Table 20: Mean time to initiate a pulse v. pulse size. 209
Table 21: Group binning for assembly time distribution curves. 212

CHAPTER 1: INTRODUCTION

Fast burst reactors (FBRs) have been in operation for many decades with the demonstration of the first fast burst assembly named the Dragon Experiment (Frisch 1969). The successful use of these machines has lead the way for their operation as critical experiments, used for determination of physics constants, as well as operation as an irradiation source. The Sandia Pulse Reactors (SPR I-III) have been primarily used for their irradiation capability, in particular SPR-III with its large central cavity for irradiating objects. FBRs can be operated in a steady state mode at low powers (typically a few kW) or in a pulse mode where high transient powers (~10 MW-sec) are feasible for short periods of time. During operations in pulse mode some fast burst reactors have been shown to undergo a pre-initiation event. Understanding this pre-initiation event was the primary driver behind this work. For experimental operations, a pre-initiation refers to a prompt critical excursion taking place prior to the final desired reactivity state being reached. Prompt critical refers to the point at which the reactor will operate on prompt neutrons. Any delayed neutrons from fission have sufficiently long half-lives that they are not important to the reactor kinetics in the initial pulse buildup.

Pre-initiation events result in lower yield pulses but do not pose any safety risk to the reactor. In these types of systems low background neutron levels are desired such that during assembly of the fissile mass an excursion does not occur prior to the final reactivity state being reached. If the background neutron level is of sufficient intensity, the fissile mass has a larger probability of one of these source neutrons leading to a

divergent chain. Eventually a source neutron will cause a divergent neutron chain to form if the system is above prompt critical. The rate at which these chains buildup is commonly known as the reactor period; in particular, when the number of neutrons is large enough to be considered deterministic. For all assemblies below prompt critical with a source present, an individual fission chain must eventually die off. For assemblies operating above prompt critical, on the average, a persistent fission chain will always exist which initiates the excursion unless there are no sources of neutrons in the system. Due to the stochastic nature of individual chains at low neutron densities, the reactor may be quiescent for some time until a persistent, divergent chain is developed. Depending on the assembly and the background neutron level, it is well known that systems may be idle for up to several seconds before a persistent fission chain develops. Waiting for a pulse to occur does not change the overall yield of the reactor; rather from a safety perspective it represents a period of time in which additional excess reactivity could be accidentally added.

In an ideal system the background source strength would be sufficiently low to allow for the final reactivity state to be reached before the pulse ensued; yet, not so low that excess reactivity states could be achieved. Most reactor systems have sufficient excess reactivity in order to accommodate large negative worth experiments. To ensure the safe operation of these machines, near zero background source strengths are not desired as the maximum over pulse (inadvertently inserting too much reactivity resulting in a larger pulse than intended) used in accident analysis to determine accident consequences greatly increases.

Operation of SPR requires the assembly of a large quantity of fissile material and external reflectors rapidly. As the pulse ensues, inherent passive design features then terminate the excursion to ensure safe operation back to ambient conditions. The prompt excursions occur so quickly that there is insufficient time for delayed neutrons to make an appreciable appearance or have any impact on the reactor kinetics during pulse buildup.

This study began with an examination of the previous operating history for the SPR-III reactor. Of the available data applicable to this work, examination of operating logs was performed to illustrate the magnitude of the pre-initiation rate for SPR. Some of these results are provided in Appendix A. Beyond these experimental results, the focus of this work was on the theoretical treatment of the non-extinction probability due to limited reactor availability at the time of this writing. In particular, a 0-D system was initially considered and relevant equations were derived to describe the resulting non-extinction probability. Analytical and numerical results were generated for the 0-D case to illustrate behaviors for the physics of interest. In particular, cases were considered for static and dynamic reactivity in conjunction with external source treatment. The results were generated with FBR behavior in mind; yet the entire multiplication factor range was also analyzed for completeness. In addition a 0-D time dependent Monte Carlo code was written to investigate the applicability of the technique for solving the pre-initiation problem. Given that the Monte Carlo work faithfully transports entire chains to either death or “divergence” additional time dependent behaviors may be assessed. Divergence is also used loosely as one must truncate fission chains due computational limitations.

From the general form of the non-extinction probability equation, consideration was then extended to a 1-D slab system. Although not identical to the SPR geometry, analysis of a slab provides a better understanding of the importance of the initial neutron injection position and angle. The 1-D equation solved was also monoenergetic in nature. Since most FBRs rely on fast fission, the monoenergetic approximation is not too limiting. Even more important, the focus of this work was to examine the non-extinction probability from a first principles perspective. Inclusion of multiple energy groups is straightforward and thoroughly documented in the open literature for the standard transport equation. Using the 1-D equation, various iteration routines were investigated. Due to the non-linearity of the non-extinction probability equation, the performance of the different routines was thoroughly investigated. A linearized routine was implemented to accommodate theoretical analysis. In addition, linearizing the equation allows one to implement acceleration techniques. Due to the performance of the iteration routine, an acceleration scheme was explored to speed up the computational runtime.

Sandia National Laboratories was the sponsor behind this work, in particular the department which supports the safety basis for operation of SPR and other Sandia reactors. Although the focus of this work is an independent study of the operation and physics behind the reactor, some efforts were extended to support the safety basis of the machine.

1.1 Definitions

The phrase pre-initiation, probability of initiation, and non-extinction probability are often used loosely in many works but can have different meanings depending of the application. Some discussion of these terms is warranted as their use in this document is both explicit and intentional.

Pre-Initiation

Pre-initiation is defined by an experimentally derived definition taken from Sandia's operational experience on SPR. Pre-initiation for reactor operations refers to pulse experiments in which the neutron density reaches sufficiently high values before all the intended prompt reactivity can be inserted into the machine. Note that this definition takes advantage of knowledge of the neutron density and the reactivity insertion time; both of which may be arbitrarily chosen based on operational experience. Experimentally, it is impossible to measure when a divergent chain has developed. At SPR where fission chambers are used to measure fissions (or power), it is leakage neutrons and subsequent fissions in the detector that determines the power in the machine. If a single neutron is injected into the assembly and it leads to a divergent chain, there is no way to discern a difference if it took multiple neutron injections to lead to the divergent chain; information of which neutron caused the divergent chain is unknown. For experimental purposes, this detailed knowledge is not needed. A pre-initiation has occurred when a large number (arbitrarily assigned) of neutrons have built

up in the assembly before the assembly has reached the full reactivity state. At SPR this refers to the buildup occurring prior to one of its reflectors being fully inserted. What upper limit on power is chosen is arbitrary, for SPR-III this value was taken to be ~50 W or $3.7*10^{12}$ n/s (Ford 2008)

Probability of Initiation (POI)

The probability of initiation (POI) refers to the probability that an injected source neutron has multiplied and its progeny have lead to a divergent chain at infinite time. The primary difference between pre-initiation and POI lies with when the initiation event is said to have taken place and at what population divergence is assessed. It will be shown later that if one waits long enough from the initial source neutron injection time, there are two possible end states. Either the source neutron will have multiplied to a sufficient state that a divergent chain has been obtained or the initial neutron and its progeny have died away. The ratio of the number that lead to divergent chains to those injected may be taken to be the POI. Unlike the pre-initiation probability, the POI definition is independent of neutron levels and only is valid for long times (infinite to be exact) from insertion. This may be expressed mathematically as $POI = \lim_{t\to\infty} P_{NE}(\infty)$, where $P_{NE}(\infty)$ is the non-extinction probability at infinite time.

Extinction/Non-extinction probability

The extinction and non-extinction probability are the primary focus in this work. They are not limited to a single neutron; rather, they are focused on the progeny from the initial parent. With a source neutron injected into a system, the probability that it and its subsequent progeny have become extinct at some later time is defined as the extinction probability (Harris 1989). The non-extinction probability can be taken to be the complementary event. Namely, given a source neutron injected at some time, the non-extinction probability describes the probability that either the source neutron or any of its progeny are still present at some later time. There is no knowledge as to the numbers of neutrons present at these times; merely that at least one exists.

Source Non-extinction probability

The source non-extinction probability is closely related to the non-extinction probability. The non-extinction probability discussed above was focused on the probability that a chain has not become extinct from a given single neutron injection point. The source non-extinction probability is focused on the probability that a chain has not become extinct given multiple source neutrons randomly injected into the system. For low numbers of neutrons, it is assumed that each injection can be treated independently of one another. Thus the source non-extinction probability examines the probability that any of the chains have not become extinct following the injection of multiple neutrons into a medium at some time.

CHAPTER 2: MOTIVATION AND DATA

Over the years, the theory behind stochastic neutronics has been well studied. The principle behind stochastic neutronics related to this work may have been first investigated by Feynman with his paper on statistical behavior of neutron chains (Feynman 1946). In addition Courant and Wallace also expanded the initial knowledge base with their paper on fluctuations of neutrons in a reactor (Courant 1947). Treatment of an assembly under weak source conditions was investigated by Hansen with his paper on an assembly with a weak source (Hansen 1960). Hansen's work was focused on trying to determine the probability distribution in time for a neutron population in a supercritical system with the injection of one source neutron. One of the most useful aspects of the paper was what Hansen defines as a weak source condition. His weak source formula is:

$$\frac{2S\tau}{\bar{\upsilon}\Gamma_2} << 1 \qquad (1)$$

where: S is the source strength in neutrons per second (n/s)

τ is the mean neutron lifetime (s)

$\bar{\upsilon}$ is the average number of neutrons emitted per fission

Γ_2 is defined by $\Gamma_2 = \frac{\overline{\upsilon(\upsilon-1)}}{\bar{\upsilon}^2} \approx 0.8$, $\overline{\upsilon(\upsilon-1)}$ provides a measure of the width of the Gaussian fission neutron emission distribution

Assuming a mean neutron lifetime of ~10 nanoseconds (ns), the weak source condition would be satisfied if the source strength is much less than 10^8. The weak source metric was provided to qualitatively understand where one is within a stochastic regime.

In Hansen's work, focus on the requirement to meet weak source conditions was described and the fission probability distribution in time for either a ramp or step insertion of reactivity was evaluated. One of the shortcomings of Hansen's model was that the probability of a persisting chain is treated stochastically, but the subsequent multiplication of the fission chains through $\bar{\nu}$ is not stochastic and the resulting process was treated deterministically. This apparent treatment will tend to narrow the probability distribution of neutrons as it ignores the stochastic buildup which can take place over longer time frames. Pal was one of the first to make use of the probability balance equations (Pal 1962). In 1963, Bell independently developed the probability distribution equations for the number of neutrons and delayed precursors in a multiplying assembly (Bell 1963). The paper was primarily focused on an assembly brought to a supercritical state under weak source conditions. The generating function method is used to transform and simplify the probability balance equation such that it can be solved. Bell extended the work to develop the probability of exactly N neutrons being present in a fissile system as a function of time, or $P_N(t)$, in a more rigorous fashion (Bell 1965). For simplistic assumptions, a few solutions are outlined in his work, of interest are the zero source with initial neutron injection and constant source cases. Bell and Lee published a paper for the probability of initiating a persistent fission chain (Bell 1971). They derive an integro-differential equation for the non-extinction probability as a function of space,

energy, and time. For a time independent case, a problem was solved for a simple stationary system using a λ iteration scaling factor. Lewins has also published a number of papers over the years relating to stochastic fluctuations and adjoint equations (Lewins 1960a, 1960b, 1978, 1981).

Williams published a text on stochastic process in nuclear reactors (Williams 1974). He provides the forward balance equation and discussion is provided for the "birth and death" problem. Although stochastic neutronics have been fully studied in the field of reactor noise, the application and theory is different for time dependent non-extinction probability calculations.

Only within the past few years have additional reports been published on the subject. Monte Carlo techniques to analyze initiation probabilities were performed by Méchitoua (Méchitoua 2000). Monte Carlo methods are ill-suited to solve the initiation probability (this will be addressed in a subsequent chapter), Méchitoua attempts to derive a metric to determine if the neutron chain will ultimately diverge. Since computers cannot track an infinite or very large number of neutrons (which could eventually die away), use of any metric to define an infinite chain induces some bias. The Lawrence Livermore National Laboratory has recently implemented a probability of initiation capability into their parallel processor, continuous energy Monte Carlo code MERCURY (Greenman 2007). Also, Humbert has provided two papers, of interest is the use of the 2-D PANDA deterministic code (Humbert 2000, 2003). The latter paper presents results for the probability of initiation as a spatial and temporal function in a highly super prompt

critical mass (ρ > \$13). Humbert et. al., recently looked at using PANDA to model the Caliban reactor which is similar in design to SPR-II (Humbert 2004). This work also looked at experimental data for comparison to a point model for the mean burst wait time. In addition, Nolen published a work that was geared towards Monte Carlo solutions using the MC++ code and was limited to subcritical assemblies (Nolen 2000). From Nolen's work in subcritical systems, the probability of observing an infinitely long neutron chain length tends to zero. The Los Alamos National Laboratory has implemented the time independent probability of initiation capability into their PARTISN code (Baker 2005). Recently the time dependent capability was extended into PARTISN.

This work was geared towards a foundational buildup of the theory and then through the use of numerical analysis apply it to weakly prompt critical systems. The focus of the modeling effort was to fully understand the fundamentals of the theory and the application, an area which has not been well documented in the open literature. An additional focus of this work will be to examine the time importance of the reactivity insertion and the overall impact on the non-extinction probability.

2.1 Sandia Pulse Reactor-III

Sandia National Laboratories has successfully operated the SPR-I, SPR-II, and SPR-III fast reactor systems. During the time of this research, SPR-III was operational; but the security costs proved to be sufficiently great that the reactor has since been shutdown. To understand the operation of the reactor which was the driver of this work, a brief description of the reactor and the parameters of interest to this work are provided below.

2.2 SPR-III Background

The SPR-III reactor is composed of a number of high enriched U-10Mo (wt%) fuel plates. These plates are combined into two separate core halves. The fuel plates are brought together to achieve a sub delayed critical assembly; meaning that both core halves are marginally subcritical when brought together. The reactivity of the machine is adjusted with multiple reflector elements on the outside of the reactor. These reflector elements are the means of adjusting reactivity into the prompt regime. A cutaway view of the reactor is shown below.

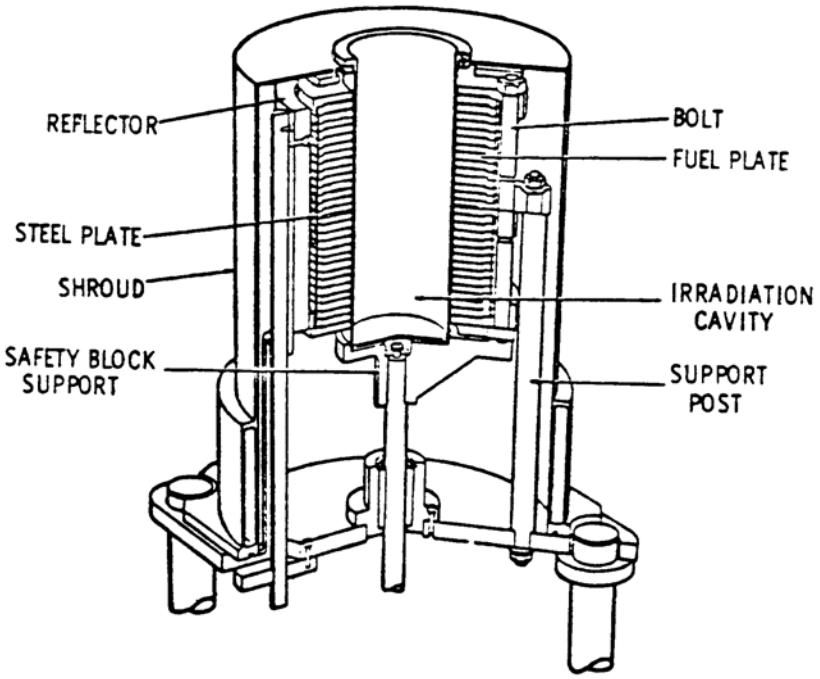

Figure 1: Graphical view of the SPR-III reactor.

In the cutaway, one can see the bolts used to hold the fuel plates together. The two core halves are shown assembled in the figure. In addition, the central irradiation cavity is seen and the external shroud. A photograph (Figure 2) of the reactor assembly is provided below with the safety block, the lower core half, decoupled (i.e. lowered). During free field operations, the experiment shroud is typically on. The shroud is boron loaded to minimize room return neutrons. The figure below has the shroud removed for viewing of the fuel plates and reflector elements. Note the separation distance of the two core halves.

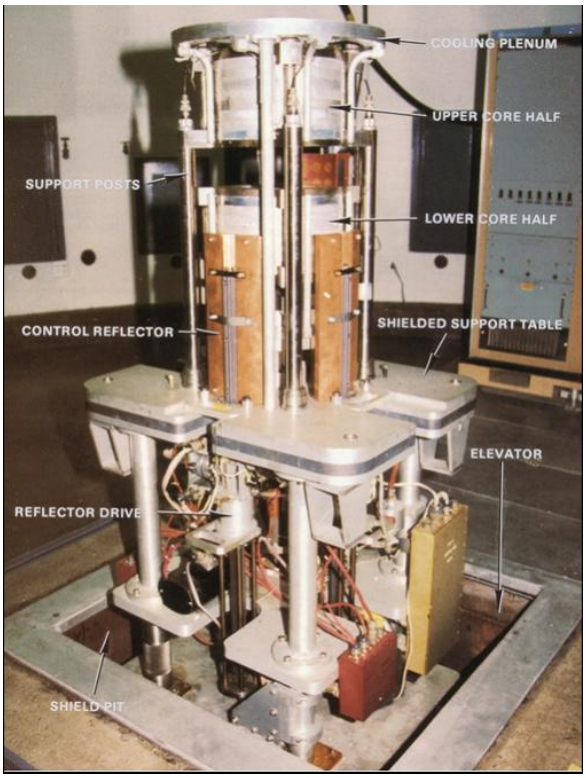

Figure 2: Picture of the SPR-III reactor with the experiment shroud removed.

The figure shows the reactor stand and associated wiring/support systems. In addition, one can see three of the four reflector elements on the outer circumference of the fuel. Although not shown in the figure, there is an external source located at the bottom of the stand in a shielded pig. When needed, the source is pneumatically driven to the outside of the core to initiate multiplication. During pulse operations the source is in its shielded location beneath the reactor.

The SPR-III reactor has successfully performed over 13,000 operations. These operations are a mix of both short steady state runs as well as pulse operations. The following figure illustrates the number of operations per year since its inception.

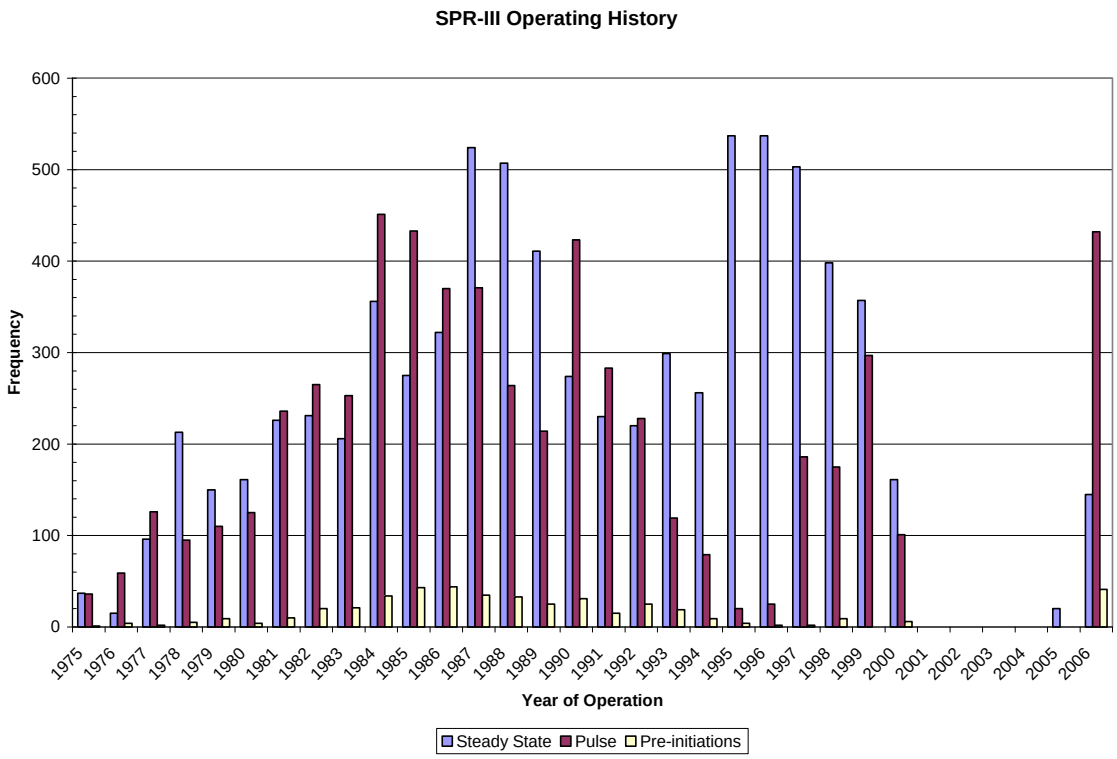

Figure 3: SPR-III operating history.

The figure also denotes the number of recorded pre-initiations per year. The overall number of pre-initiations was relatively low for this reactor, yet it was an observable phenomena. If the number of pre-initiations is divided by the total number of pulse operations over the years, the experimental pre-initiation probability is ~7.8%. Note that this probability represents the average over many experiment operations. Most of these operations involved an experiment within the central cavity. The free field pre-initiation probability may be different.

The overall pre-initiation probability is sufficiently high to be a nuisance to the reactor operations staff/experimenters as the experiments may need to be re-performed or must suffer from the lower reactor yield and broader pulse widths. This can lead to costly

experiment components/parts due to repetition of the experiment. Data mining efforts were performed to extract information for both free field and different experiments. See Appendix A for more details. This information was included in an appendix as it provides emphasis for the work as a whole; other important data for extension to SPR was gathered and is not reported.

2.3 Background Neutron Sources

There are two large contributing factors to the modest but non-trivial pre-initiation rate at SPR. The first is the inherent background neutron source. There are several sources from where the neutrons originate with the largest source coming from spontaneous fission neutrons within the reactor itself. Although the reactor fuel is highly enriched U-235, the physical mass of the system drives a non-trivial quantity of U-238 which has a relatively high spontaneous fission rate. It has been estimated that there are about 5,000 n/s (with multiplication) from spontaneous fission in the core with the reactor at -$15 (Ford 2005). The other contributing factor to the pre-initiation rate comes from the assembly time of the reactor system. In order to escape the pre-initiation phenomena, the reactor must be quickly assembled. For SPR-III, an aluminum reflector element must be driven full up to reach the final reactivity state. Due to the transit time, the random neutron levels in the core may build up prior to the reactor reaching its final reactivity state.

Assessing the background neutron source for SPR was of importance in order to determine the associated impact on the kinetic behavior. Knowledge of the average background source strength was necessary as the pre-initiation probability increases with source strength.

The spontaneous fission rates for U-235 and U-238 are shown in the table below.

Table 1: Spontaneous fission rates for uranium.

Reference:	Spontaneous fission rate (fissions/g/sec)	
	U-235	U-238
ANL-5800	$8.0*10^{-4}$	$1.6*10^{-2}$
Etherington, 1958	$3.1*10^{-4}$	$7.0*10^{-3}$

For SPR-III which has a reported fuel mass of 258 kg (232 kg U) this equates to ~181 fissions/sec un-multiplied (using the Etherington data). The SPR-III safety basis cites 470 n/sec un-multiplied which agrees with the Etherington data if $\bar{\upsilon}$ is factored in.

For SPR a neutron source was required during startup conditions to ensure that sustained fission chain results (and multiplication) can be monitored before a supercritical assembly is achieved. The SPR neutron source is on the order of $1*10^{6}$ n/s but is not used during a pulse operation.

2.4 Nuclear Data

Prior to delving into the theory, some discussion on nuclear data is warranted. Several have published fission neutron multiplicity data in tabular format. These include the works by Diven (1955), Terrell (1957), Holden (1988), and Frehaut (1988). This tabular data is repeated below as it is used heavily in this analysis.

Table 2: Fission multiplicity data.

ν	Diven (1955)	Holden (1988)	Frehaut* (1988)
0	0.027 ± 0.007	0.0317 ± 0.0015	0.0425
1	0.158 ± 0.004	0.1720 ± 0.0014	0.1685
2	0.339 ± 0.014	0.3363 ± 0.0031	0.3246
3	0.305 ± 0.015	0.3038 ± 0.0004	0.2990
4	0.133 ± 0.013	0.1268 ± 0.0036	0.1270
5	0.038 ± 0.009	0.0266 ± 0.0026	0.0330
6	-0.001 ± 0.003	0.0026 ± 0.0009	0.0047
7	0.001 ± 0.002	0.0002 ± 0.0001	0.0006
$\bar{\nu}$	2.47 ± 0.03	2.413 ± 0.007	2.420
* Normalized to one and adjusted to preserve $\bar{\nu}$ (Nolen 2000).			

For computation of constants used later in this work, the Frehaut data set is used. In addition to the fission multiplicity data some discussion of neutron cross-sections is also needed. The figure below plots the U-10Mo neutron cross-section which was produced using MCNP5 (LA-UR-03-1987 2003).

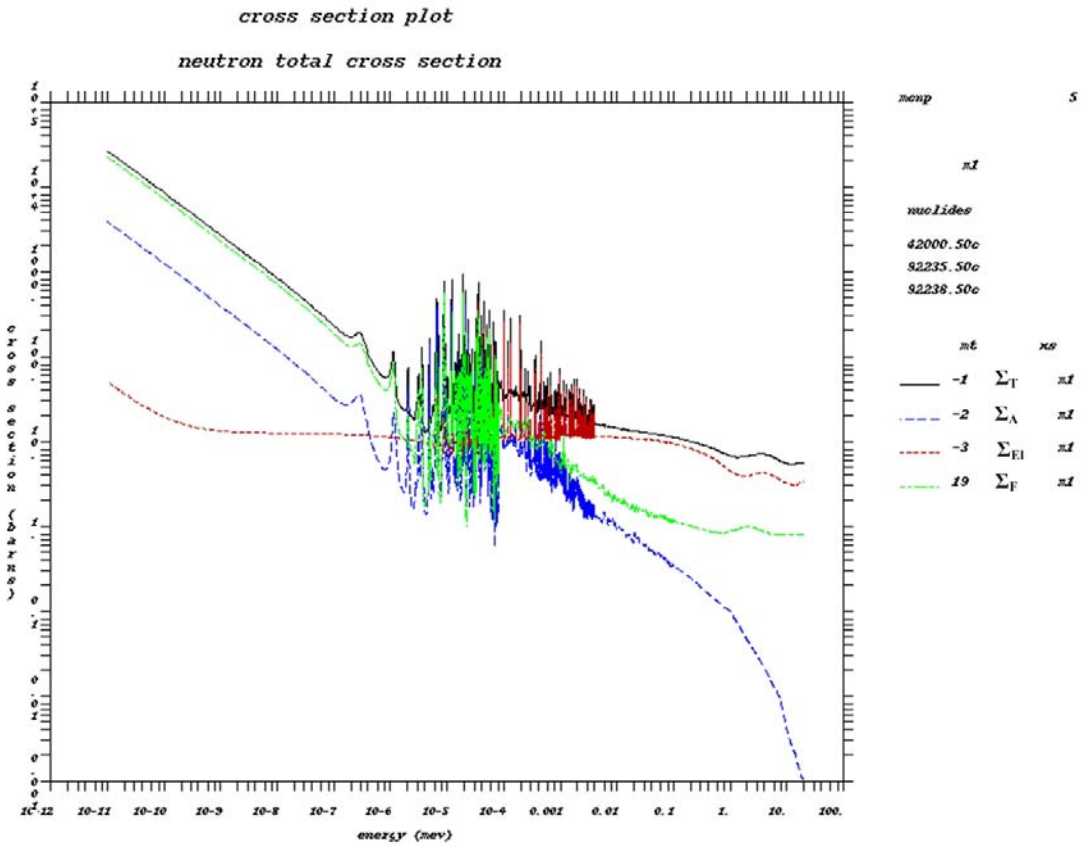

Figure 4: U-10 Mo Neutron cross-sections.

The total, absorption, elastic scattering, and fission cross-section are shown above. For a fast metal system, the resulting neutron spectrum is "hard". The average energy of fission neutrons is ~1.98 MeV and the peak of the emission curve corresponding to the most probable energy is ~0.73 MeV (Lamarsh 2001). One can see that at these energies, elastic scattering is the dominant reaction followed by fission. For this work the total cross-section was taken to be 6 barns. The scattering cross-section was taken to be 5 barns, the fission cross-section 0.9 barns, and the capture cross-section 0.1 barns. There is little change in the cross-section data around the fission spectrum indicating that a one group model may be sufficient for analysis.

CHAPTER 3: THEORY

This section of the work outlines the theory used to analyze stochastic neutronics including the non-extinction probability. Williams (1974) points out that the foundational concepts with population fluctuations were not developed by neutron physicists, but rather by biologists and naturalists, namely Galton and Watson in 1874. For reactor systems, there are two particular areas where stochastic neutronics receive particular attention. The first is found with noise when the reactor is at power. The second, and more prominent for FBRs, is geared towards the initial fluctuations seen in power during reactor startup. The time associated for buildup to a steady reactor power is not consistent if operating under weak source conditions. Thus even if the same sequence of steps are followed at the exact same time, the overall time to buildup to some power level differs. A balance is to be played as reactor operations prefer sufficiently low source strengths to ensure a pre-initiation does not occur, while nuclear safety requirements dictate exactly the opposite. The theory below was developed for stochastic neutronic buildup in prompt critical systems. It is geared around prompt neutrons only; although delayed neutrons can be readily incorporated into the balance equations. Given the short period of time SPR sits at prompt critical, neglecting delayed neutrons is an adequate assumption. The theory begins by developing relationships that describe the probability of exactly N neutrons present in an assembly. In order for the relationship to be evaluated, the analysis will be extended to any number of neutrons being present via generating functions.

3.1 Stochastic Behavior

The variability of the overall yield in a pulse and the time at which the pulse occurs in a reactor is known to vary quite randomly. This behavior is primarily attributable to the fission process. Namely, the number of neutrons per fission is a random variable. Although the mean number of neutrons per fission is typically used in standard reactor theory, fission chains see localized increases/decreases in the overall population from the number of neutrons emitted per fission. Secondly, the time in which reaction events occur in a medium is a random variable. In reactor theory the assumption is commonly made that reaction events occur proportionally to the average neutron lifetime in the medium. Finally, the type of reaction event that is chosen is also variable. Although the average probability of different events occurring is known though reaction cross-section data, localized increases/decreases in a fission/capture reaction can cause variations in the chain population (Williams 1974).

Neutrons can be said to behave stochastically if the population of those neutrons in the assembly is sufficiency low. A Markov process is one in that the chance of an event being recorded within a small time interval Δt is independent of the states at previous times (Williams 1974). This implies that the number of neutrons in the assembly at current times has relation to previous times only in the sense that it determines the current number of neutrons, but the behavior of the neutrons at future times is independent of the past. It is assumed that the changes in an assembly are sufficiently small such that in a time increment on the order of Δt, the changes in the system are on the order of Δt.

Neutronic behavior in a pulse type assembly under weak source conditions is initially completely random. It is sometimes difficult to distinguish the difference between deterministic and stochastic conditions. A decent metric for assessing divergence is to use the lowest steady state power level that can be achieved for the reactor. A steady state power can only be achieved through the use of a deterministic population. It is estimated that SPR-III could be operated at a power level of ~1 mW. Using the appropriate unit conversions, this equates to about 75 million neutrons/sec. Assuming one initial source neutron, it would require ~18 e-foldings (e^{18}) to reach 75 million. With reactor periods on the order of ~30 μs, the deterministic buildup could be reached in ~ 0.54 ms. Clearly this buildup could occur rapidly.

Some efforts to describe a stochastic process are warranted given their application in this work. Following the notation and discussion of Bartlett, such processes may be viewed as a random sequence in which some variable X_n at a given time t_n is independent of the previous entire set of X 's (Bartlett 1978). The random walk of the variable may be viewed as the cumulative sum of the variable X at different times. For relation to a Markov process it is assumed that the values of X_n at any set of times t_n ($n = 1,2,\ldots N$) depend on the values X_m at any set of previous times t_m ($m = 0,-1,\ldots,-j$) through the last value of X_0. Thus the distribution at times t_n $(t_1 < t_2 < \ldots t_n)$ is related through:

$$\begin{aligned} & p(x_1,t_1;x_2,t_2;\ldots,x_n,t_n) = p(x_1,t_1)\cdot p(x_2,t_2 \mid x_1,t_1)\cdot p(x_3,t_3 \mid x_1,t_1;x_2,t_2)\cdot\cdots \\ & = p(x_1,t_1)\cdot p(x_2,t_2 \mid x_1,t_1)\cdot p(x_3,t_3 \mid x_2,t_2)\cdot\cdots \\ & = p(x_1,t_1)\cdot\prod_{n=2}^{N} p(x_n,t_n \mid x_{n-1},t_{n-1}) \end{aligned} \qquad (2)$$

The notation of $p(x_2, t_2 \mid x_1, t_1)$ denotes the conditional probability of observing event x_2 given event x_1. Thus the Markov process is then defined by the conditional probability distribution $p(x_n, t_n \mid x_{n-1}, t_{n-1})$ for any n combined with the initial distribution $p(x_1, t_1)$.

3.2 Point Model Derivation

3.2.1 Forward Equation

In this section, a derivation of the 0-D equation for the probability of exactly N neutrons being present in an assembly at time t, or $P_N(t)$. Direct solution of this probability equation will give complete knowledge of the number of neutrons present in an assembly at any time t, from which the extinction $(P_0(t))$ or the non-extinction probability $(1 - P_0(t))$ can be investigated. Moreover, statistical moments such as the mean and variance of the neutron population can be readily obtained and evaluated.

The equations and derivations below have been initially reported elsewhere. This work includes a summary of important features for consistency. For the full derivation of these equations see the works of Courant (1947), Feynman (1946), Bell (1963), Bell (1965), and Williams (1974).

The following definitions and assumptions are made:

Let $P_N(t \mid t_0)$ be the probability that N neutrons exist in some system at time t given one neutron was injected at time t_0. It is assumed that Δt is large enough such that one neutron can be emitted during the time interval but small enough to make sure the events are mutually exclusive.

Following the notation of Williams (1974), let:

$\frac{1}{\lambda_F} = \frac{1}{\nu \cdot \Sigma_F}$ = mean lifetime for a fission neutron. Also, let the probability that j neutrons are released per fission be p_j for $1 \leq j \leq 7$. This represents a net increase in neutron population.

$\frac{1}{\lambda_C} = \frac{1}{\nu \cdot \Sigma_C}$ = mean lifetime for a capture neutron. This represents a net decrease in neutron population.

S = external random source strength/time interval, assumed to emit one neutron in the time interval; however, other sources may be used.

A balance equation can be setup for $P_N(t \mid t_0)$ by accounting for all independent and mutually exclusive processes that can occur within a short interval of time Δt, noting the Markovian character of the statistical processes of interest. By enumerating all possible events that may happen during the time interval Δt:

$$\underset{\text{a}}{P_N(t+\Delta t \mid t_0)} = \underset{\text{b}}{P_{N-1}(t \mid t_0) \cdot S \cdot \Delta t} + \underset{\text{c}}{P_{N+1}(t \mid t_0) \cdot (N+1) \cdot \lambda_C \cdot \Delta t} + \tag{3}$$

$$\underset{\text{d}}{\sum_j P_{N+1-j}(t \mid t_0) \cdot (N+1-j) \cdot p_j \cdot \lambda_F \cdot \Delta t} + \underset{\text{e}}{P_N(t \mid t_0) \cdot \left[1 - S \cdot \Delta t - N \cdot (\lambda_C + \lambda_F)\Delta t\right]} + o(\Delta t)$$

where:

a. Probability that there are N neutrons at time $t + \Delta t$ given one neutron was injected at time t_0.

b. Probability that there are $N-1$ neutrons at time t and the source emits one neutron within Δt.

c. Probability that there are $N+1$ neutrons at time t and one is captured within Δt.

d. Probability that there are $(N+1-j)$ neutrons in the system and that any of those neutrons causes a fission yielding up to j neutrons $(j = 0,1,\ldots J)$ within Δt.

e. Probability that there are N neutrons at time t and nothing happens within Δt.

Dropping the conditional probability notation, combining terms and rearranging:

$$\frac{P_N(t+\Delta t) - P_N(t)}{\Delta t} = S \cdot \left[P_{N-1}(t) - P_N(t)\right] + \lambda_C \cdot (N+1) \cdot P_{N+1}(t) - \tag{4}$$

$$N \cdot (\lambda_C + \lambda_F) \cdot P_N(t) + \lambda_F \cdot \sum_j P_{N+1-j}(t) \cdot (N+1-j) \cdot p_j + o(\Delta t)$$

Taking the limit as $\Delta t \to 0$ and recognizing the definition of a derivative on the left hand yields:

$$\frac{dP_N(t)}{dt} = S \cdot \left[P_{N-1}(t) - P_N(t)\right] + \lambda_C \cdot (N+1) \cdot P_{N+1}(t) - N \cdot (\lambda_C + \lambda_F) \cdot P_N(t) + \lambda_F \cdot \sum_j P_{N+1-j}(t) \cdot (N+1-j) \cdot p_j \tag{5}$$

Assuming there is one neutron initially in the system, a suitable initial condition may be expressed as $P_N(t_0) = \delta_{N,1}$ where δ is the Kronecker delta function. Equation 5 is the differential form of the Chapmann-Kolmogorov equation and represents an infinite hierarchy of differential equations for the desired neutron number probability. As such, it is not amenable to solution in this form. Although truncation of the hierarchy may be considered, interesting values of N are typically in excess of 10^6 so direct solution is impractical. Even for small values of N, it is seen that the solution at the value of N is dependent on other terms (from the $N+1-j$ terms in the summation). However, an alternative formulation based on a probability generating function (pgf) is more suitable for analysis. The differential-difference equation above may be dealt with through the use of a probability generating function.

The probability generating function associated with a discrete-state continuous time probability distribution function (pdf) is defined by:

$$G(x,t) = \sum_{N=0}^{\infty} x^N \cdot P_N(t) \tag{6}$$

with $|x| < 1$ such that $G(x,t) = P_0(t) + x \cdot P_1(t) + x^2 \cdot P_2(t) + \ldots$. Each term in the generating function describes the probability of either zero, one, two, etc. neutrons as a function of time. Using a generating function removes information of the exact numbers of neutrons present in the system and transforms them into a new variable G. Another generating, $g(x)$ is also needed for the fission multiplicity where $g(x) = \sum_{N=0}^{\infty} x^n \cdot p_n$.

The hierarchical equations for the pdf may be transformed to a single partial differential equation for the pgf as follows. First note some properties:

$$\frac{\partial G(x,t)}{\partial x} = \sum_{N=1}^{\infty} N \cdot x^{N-1} \cdot P_N(t) \tag{7}$$

$$\frac{\partial G(x,t)}{\partial t} = \sum_{N=0}^{\infty} x^N \cdot \frac{dP_N(t)}{dt} \tag{8}$$

$$x\frac{\partial G}{\partial x} = \sum_{N=1}^{\infty} N \cdot x^N \cdot P_N(t) = \sum_{N=0}^{\infty} N \cdot x^N \cdot P_N(t) \tag{9}$$

All terms in Eq. 5, are then multiplied by x^N and summed over all N to obtain:

$$\begin{aligned} \sum_{N=0}^{\infty} x^N \cdot \frac{dP_N(t)}{dt} \cdot = \sum_{N=0}^{\infty} x^N \cdot S \cdot \left[P_{N-1}(t) - P_N(t)\right] + \lambda_C \cdot \sum_{N=0}^{\infty} x^N \cdot (N+1) \cdot P_{N+1}(t) - \\ N \cdot (\lambda_C + \lambda_F) \cdot P_N(t) + \lambda_F \cdot \sum_{N=0}^{\infty} \sum_{j} x^N \cdot P_{N+1-j}(t) \cdot (N+1-j) \cdot p_j \end{aligned} \tag{10}$$

Using the generating function and the derivative properties defined above in Eqs. 7-9, the equation reduces to:

$$\frac{\partial G}{\partial t} = (x-1)\cdot S \cdot G + \left[\lambda_C \cdot (1-x) + \lambda_F \cdot (g(x)-x)\right]\frac{\partial G}{\partial x} \tag{11}$$

Subject to initial condition:

$$G(x,0) = x \tag{12}$$

Eq. 11 is a partial differential equation for the generating function which embodies the same information as the complete probability distribution but now has a more appealing form for analysis. While its solution under general conditions cannot be explicitly obtained, closed form solutions can be obtained for special cases from which the probability distribution can then be constructed by expanding the pgf in powers of x. Alternatively, equations for the moments can also be directly obtained; however, these are not of particular interest here.

Eq. 11 can be recast into an alternate form that makes it more useful for further analysis. In particular the second and third terms on the right hand side may be combined into a more concise format. Following the notation of Bell (1963), let

$f(x,t) = \lambda_C \cdot (1-x) + \lambda_F \cdot (g(x)-x) = -x + \sum_{j=0}^{J} x^j \cdot c_j(t)$ where the $c_j(t)$ terms represent the probability of fission times j neutrons being emitted per fission.

The generating function equation simplifies to:

$$\frac{\partial G}{\partial t} = S \cdot (x-1) \cdot G + f(x,t) \cdot \frac{\partial G}{\partial x} \tag{13}$$

Additional discussion on the physics terms which embody the $c_j(t)$ terms is warranted. Following Bell, it is first noted that x^j may be expanded into

$$x^j = [1-(1-x)]^j = 1 - j \cdot (1-x) + \frac{j \cdot (j-1)}{2!}(1-x)^2 - \ldots + \frac{(-1)^j \cdot j \cdot (j-1) \cdot \ldots}{j!} \cdot (1-x)^j .$$

This expansion is then developed further such that in $g(x,t)$ the term in the summation becomes, $\sum_{j=1}^{J} j \cdot (j-1) \cdots (j-i+1) \cdot c_j(t) = p_f(t) \cdot \chi_i = \frac{k(t)}{\bar{\nu}} \cdot \chi_i$ where the χ_i terms are constants from the fission multiplicity (see Table 3 to follow).

Using these relations, the formulation for $g(x,t)$ simplifies to

$g(x,t) = (1-x) \cdot [1-k(t)] + \frac{k(t)}{\bar{\nu}} \cdot \sum_{j=2}^{J} (-1)^j \cdot \frac{\chi_j}{j!} \cdot (1-x)^j$ where the terms $\frac{\chi_j}{j!}$ represent the fission neutron multiplication ($j = 2$ neutron pairs, $j = 3$ neutron triplets, etc). Bell notes that if $g(x,t)$ is set to zero, then for stationary time independent systems the steady state (SS) non-extinction probability or POI is in fact the root of the equation. Bell makes use of a quadratic truncation which appears to be valid over regimes where $k - 1 < 0.10$ (Bell 1963). The quadratic truncation takes the summation in the above formula to be limited to the second term $(j = 2)$, which assumes that $\bar{\nu} = 2$. It is common to truncate the fission generating function at the second term as it allows

development of analytical solutions under limiting conditions. This is equivalent to the historical "birth and death model" as outlined in Williams 1974. Truncation at the second order fission term is partially justified by the fact that the first and second moments (mean and variance) of the neutron distributions are correctly obtained (Lewins 1978). The validity of the quadratic approximation versus using the full fission distribution will be covered in detail in subsequent sections.

3.3 Fission Multiplicity Constants

For reference the fission multiplicity constants used in this work are taken from the modified Frehaut (1988) distribution in Nolen (2000). The non-linear fission multiplicity constants, χ_i, are provided below in tabular format. For these constants, Bell and Méchitoua present two different equations. The equations are identical, merely recast to explicitly include $\bar{\nu}$ where Bell's notation pulls it out of the summation term (Bell 1965, Méchitoua 2000).

For simplicity the following definition was used to calculate the fission multiplicity constants:

$$\chi_i = \frac{(-1)^i}{i!} \cdot \sum_{j=2}^{i} j \cdot (j-1) \ldots (j-i+1) \cdot p_j \tag{14}$$

where p_j is the probability of j neutrons emerging from fission.

Table 3: Fission multiplicity constants.

i	f_i	χ_i
2	0.3246	4.793
3	0.2990	7.512
4	0.1270	9.204
5	0.0330	8.856
6	0.0047	6.408
7	0.0006	3.024

3.4 Solutions for $P_N(t)$ Invoking the Quadratic Approximation

By limiting the non-linear terms to the quadratic truncation, analytical solutions for the probability of N neutrons at time t, or $P_N(t)$ can be found. Efforts were initially focused on a zero source and constant source case.

3.4.1 Zero Source

For a zero source and constant source case Bell was able to invert a Laplace transform of the generating function equation to provide an approximate solution for the probability of N neutrons that is valid for large times and large neutron populations. In particular, Bell assumed that the mean was represented as $\bar{n}(t) = e^{\int_{t_0}^{t} \alpha(t') \cdot dt'} >> 1$. Given that $\alpha = \left(\frac{k_p - 1}{l} \right)$ is typically a large number due to the small neutron lifetime, the integration forward in time is not too limiting to preclude the formula to be of use. The solution for the zero source case assuming one initial source neutron derived by Bell is:

$$P_N(t) = [1 - p(t_0)] \cdot \delta_{N,0} + \frac{p(t_0)^2}{\bar{n}(t)} \cdot e^{-\left(\frac{p(t_0) \cdot N}{\bar{n}(t)} \right)} \tag{15}$$

where $p(t_0) = POI = \frac{2 \cdot \bar{\nu} \cdot (k-1)}{k \cdot \chi_2}$. Bell's formula for $P_N(t)$ is useful for large values of N ; however it does a poor job for small numbers of neutrons at early times. It is worthwhile mentioning that explicit formulas for $P_N(t)$ can be extracted without having to use Laplace transforms. A construction for $P_N(t)$ is provided below using a series expansion. For the zero source case, the derivation begins with Bell's formula for the generating function (Bell 1963):

$$G(x,t) = 1 + \frac{e^{\int_{t_0}^{t} \alpha(t') \cdot dt'}}{\frac{1}{x-1} - \int_{t_0}^{t} \frac{\chi_2'}{2} \cdot e^{\int_{t'}^{t} \alpha(t'') \cdot dt''} \cdot dt'} \tag{16}$$

Representing the integral in the denominator as $b(t)$ and the numerator as $\bar{n}(t)$, a binomial expansion of the above yields (Prinja – unpublished notes):

$$G(x,t) = 1 + \frac{\bar{n}(t)}{\frac{1}{x-1} - b(t)} = 1 - \frac{\bar{n}(t)}{1+b(t)} + \frac{\bar{n}(t)}{[1+b(t)]^2} \cdot \sum_{N=1}^{\infty} \left(\frac{b(t)}{1+b(t)} \right)^{N-1} \cdot x^N \qquad (17)$$

From the definition of the generating function, the coefficients for the $P_N(t)$ terms may be readily found.

$$P_0(t) = 1 - \frac{\bar{n}(t)}{1+b(t)} \qquad (18)$$

$$P_N(t) = \frac{\bar{n}(t)}{b(t)^2} \cdot \left[\frac{b(t)}{1+b(t)} \right]^{N+1} \quad \text{for } N = 1,2,\ldots \qquad (19)$$

A formula for the extinction probability $P_0(t)$, as well as for any number of neutrons can be found at all times without any restriction on time, size of the neutron population, or the system multiplication factor.

3.4.2 Probability of N neutrons

For static reactivity, both $b(t)$ and $\bar{n}(t)$ are readily found:

$$\bar{n}(t) = e^{\int_{t_0}^{t} \alpha(t') \cdot dt'} = e^{\frac{1}{l} \cdot (k-1) \cdot (t-t_0)} \qquad (20)$$

$$b(t) = \int_{t_0}^{t} \frac{\chi_2'}{2} \cdot e^{\int_{t'}^{t} \alpha(t'') \cdot dt''} \cdot dt' = \frac{k \cdot \chi_2}{2 \cdot \bar{\nu} \cdot (k-1)} \cdot \left(\bar{n}(t) - 1 \right) = \frac{1}{POI} \cdot \left(\bar{n}(t) - 1 \right) \qquad (21)$$

Using Bell's time asymptotic solution for $P_N(t)$ and the exact solution shown above, a comparison is presented in the figure below. For this figure, the following constants were used: $k = 1.0072$, $l = 10^{-8}$ sec.

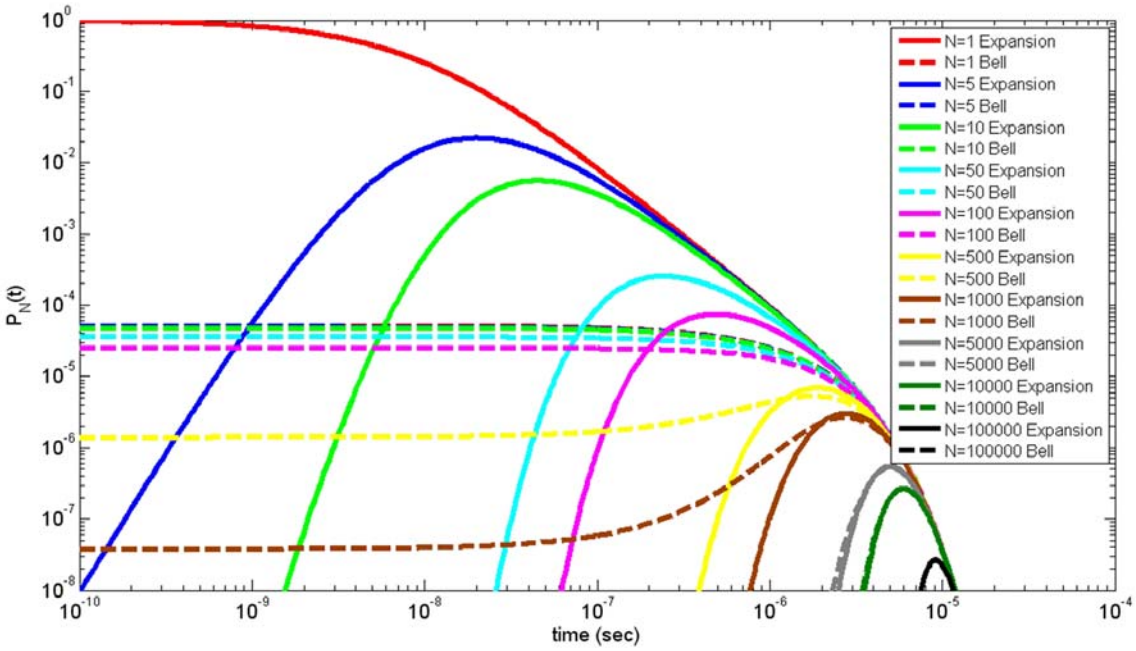

Figure 5: Comparison of solutions of the quadratic truncation for $P_N(t)$ for static reactivity.

The figure contains curves for different fixed values of N. The solid lines in the figure represent the exact solutions given by the series expansion. The dashed lines represent Bell's approximation. For small values of N and time, there is a large disagreement in the results. This disagreement is due to Bell's assumption that the value of N is large and sufficient time has elapsed $\left(\bar{n}(t) >> 1\right)$ from the initial injection event. Once the number of neutrons is on the order of a few thousand or greater, good agreement is found between the two results. In particular the time asymptotic behavior of both formulas agrees well.

The results in the figure show that at early times the probability of observing many neutrons was small as only one initial source neutron was present. Larger numbers of neutrons begin to appear later in time as neutron multiplication takes place. At times ~ 10^{-5} the overall solution for any number of neutrons becomes vanishingly small and all cases follow an asymptotic shape. The figure above can be related to the non-extinction probability that will be solved numerically in subsequent chapters. If one sums over all numbers of neutrons, one obtains the non-extinction probability. The extinction probability can be readily found by simply setting $N = 0$ or simply subtracting the non-extinction probability from unity. To highlight this behavior and the functional shape of the time non-extinction probability, the figure below plots both the time dependent extinction and non-extinction probability.

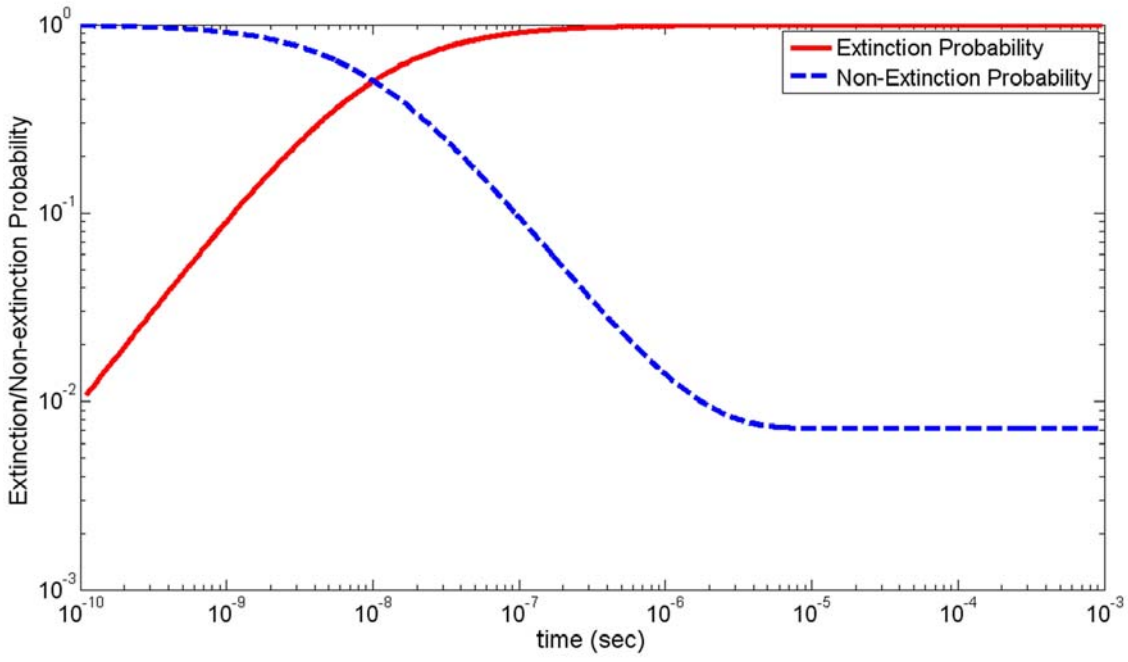

Figure 6: Extinction and Non-extinction probability for static reactivity.

One can see that initially the non-extinction probability is unity at the initial condition and then decreases as a function of time. The complementary extinction probability shows that at late times the probability the chain has become extinct is quite high, yet there is finite probability that the chain has become divergent which is seen by the asymptotic SS non-extinction probability, or POI.

3.4.3 Constant Source

The results presented above were for a single initial injected neutron. In Bell's work discussing the zero source case, he extended the theory to include the impact of a constant source (Bell 1963). The constant source cases assume initially there were no neutrons in the system and then just shortly after time zero, a constant source of neutrons was injected. The formula derived by Bell was:

$$P_N(t) = \left(\frac{\eta}{\bar{n}(t)}\right)^{\eta} \cdot \frac{1}{\Gamma(\eta)} \cdot N^{\eta-1} \cdot e^{\left(-\frac{\eta \cdot N}{\bar{n}}\right)} \tag{22}$$

where $\eta = \dfrac{2 \cdot S}{\chi_2'} = \dfrac{2 \cdot S \cdot l \cdot \Sigma_A}{\Sigma_F \cdot \chi_2}$

The gamma function was substituted into Bell's formalism to allow for source strengths that are less than the resulting neutron lifetime (η can be less than one). Note that the value of η (or essentially the product of $S \cdot l$) governs the broadness of the distribution. The formula for the constant source case was also confirmed by Harris and compared to the subprompt critical experiments documented in Hanson (Harris 1961). Harris notes

that the probability distribution solution satisfies a gamma distribution where η can be taken to be the relative standard deviation.

Following the format for the zero source case, an expression may be derived for the source case using a series expansion. Revisiting Bell's source generating function (1963):

$$G(x,t) = G(x_0,t_0)\cdot\left[1-(x-1)\cdot\int_{t_0}^{t}\frac{\chi_2'}{2}\cdot e^{\int_{t'}^{t}\alpha(t'')\cdot dt''}\cdot dt'\right]^{-\frac{2S}{\chi_2'}} \tag{23}$$

It is assumed (as was in Bell's work) that the function $G(x_0,t_0)$ is initially zero which means that initially there are zero neutrons in the system. Representing the integral as $b(t)$, and substituting in Bell's variable $\eta = \frac{2\cdot S}{\chi_2'}$, the equation for the generating function takes the form:

$$G(x,t) = \frac{1}{\left[1-(x-1)\cdot b(t)\right]^{\eta}} = \frac{1}{\left[1+b(t)\right]^{\eta}}\cdot\sum_{N=0}^{\infty}\frac{\Gamma(\eta+k)}{N!\cdot\Gamma(\eta)}\cdot\left(\frac{b(t)}{1+b(t)}\right)^{N}\cdot x^{N} \tag{24}$$

Using the definition of the generating function the values of $P_N(t)$ may be found from:

$$P_N(t) = \frac{1}{\left[1+b(t)\right]^{\eta}}\cdot\frac{\Gamma(\eta+N)}{N!\cdot\Gamma(\eta)}\cdot\left(\frac{b(t)}{1+b(t)}\right)^{N} \tag{25}$$

Solution of the above formula allows one to determine the probability of N neutrons at any time t for a fixed constant source. It is worthwhile to note that the extinction probability for the source case goes to zero for large times. Physically this means that for a prompt critical system with a constant source, one of the source particles will eventually lead to a divergent chain and thus the extinction probability must be zero.

The time dependent behavior for the extinction probability can be seen by setting N to zero in Eq. 25. Upon doing so the extinction probability then becomes:

$$P_0(t) = \frac{1}{[1 + b(t)]^{\eta}} \tag{26}$$

The variable $b(t)$ is related to $\bar{n}(t)$ which continues to grow rapidly as a function of time. At late times $b(t)$ is a tremendously large number. Even for small values of η, the term in the denominator continues to grow with time until eventually the extinction probability eventually becomes zero.

3.4.4 Probability of N neutrons

Expansion solutions are compared against Bell's solution for various times, numbers of neutrons and source strengths. As the plots are dependent upon multiple variables, only a few source strength plots are presented. The first is that of a small source, whereas the second represents a strong source.

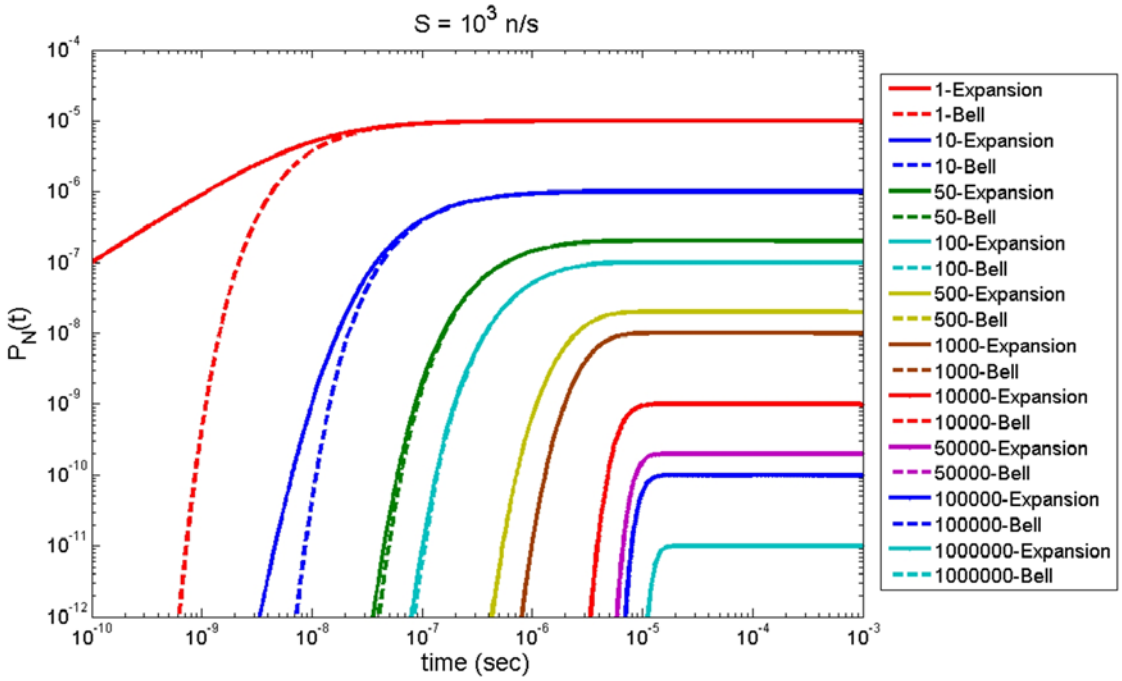

Figure 7: Comparison of solutions of the quadratic truncation for $P_N(t)$ for static supercritical reactivity with a weak source.

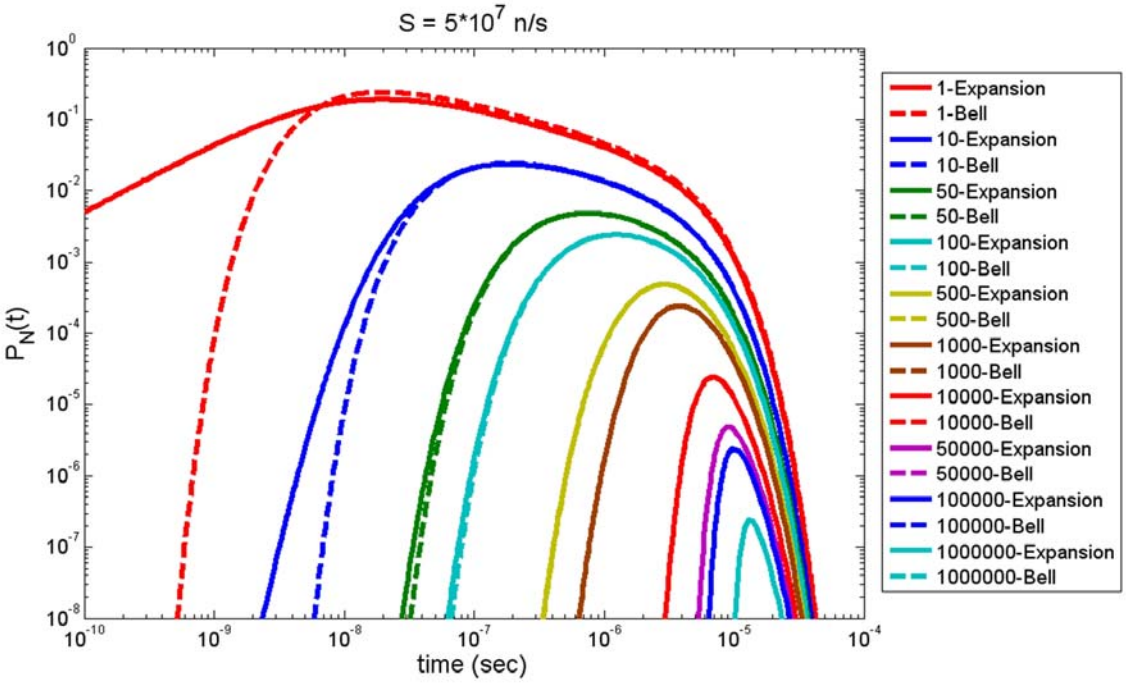

Figure 8: Comparison of solutions of the quadratic truncation for $P_N(t)$ for static supercritical reactivity with a strong source.

As was shown for the zero source case, deviations are seen for early times and small numbers of neutrons. The difference between the solutions was seen regardless of the source strength used. For small source strengths the probabilities build up to near constant values for time frames of interest. As the source strength was increased the probability of observing any numbers of neutrons at late times goes to zero. This is again due to the fact that for a prompt critical system with a source the system must lead to a divergent chain. As the source strength was increased, the time at which these curves go to zero becomes shorter and shorter indicating that a divergent chain has developed.

To reinforce the concept that prompt critical systems with a source must lead to a divergent chain, the probability of finding zero neutrons as a function of time (the extinction probability) and the complementary event (the non-extinction probability are provided below) for a strong source.

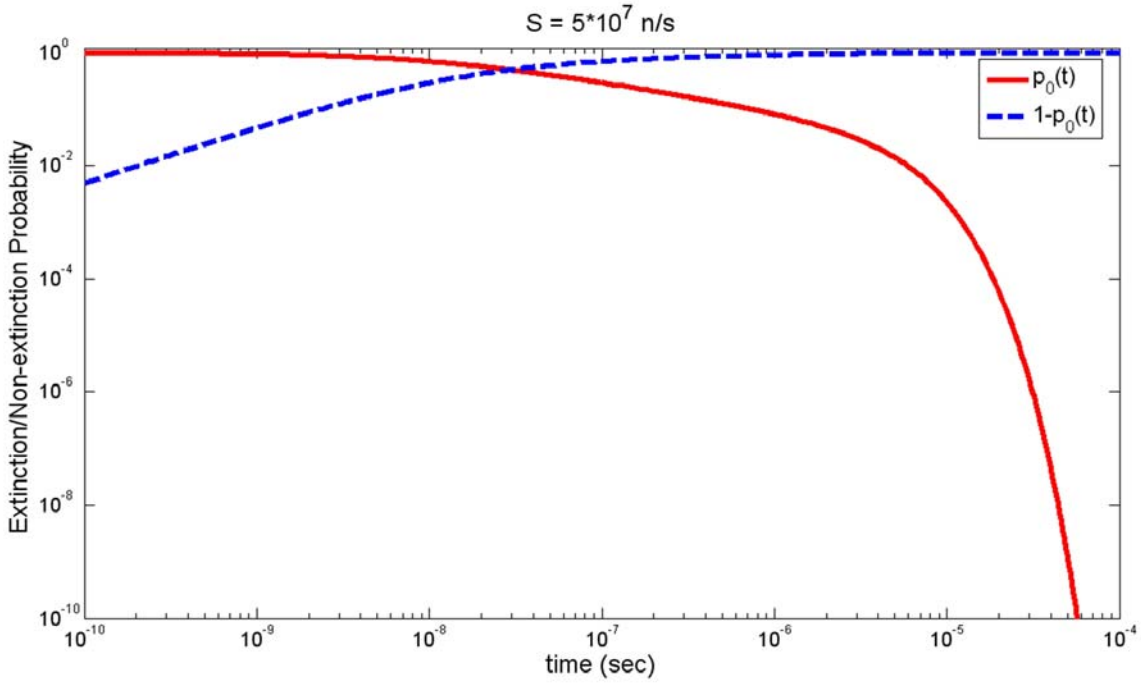

Figure 9: Extinction and non-extinction probability for a prompt critical system with a source.

With a source present in a prompt critical medium, the extinction probability must go to zero. This was seen in the figure above which shows that the extinction probability rapidly approaches zero while the complementary non-extinction probability rapidly approaches unity. As time approaches infinity, the non-extinction probability does go to unity and a divergent chain has developed.

3.5 Dynamic Reactivity Insertions

The theory presented so far was generic with respect to the overall system reactivity. The initial discussion was that of a static system to understand constant reactivity systems and then proceeds to include dynamic reactivity insertions. As all pulse reactor systems must insert reflectors or fissile material, the system reactivity is typically ramped as a function of time. This additional time dependence makes the non-extinction probability problems interesting and complex.

Much of the initial analytical work and numerical results were focused on static reactivity to confirm theory. Upon good agreement with theory, the results were then extended to either a step or ramp insertion case where the system would be idle at some lower reactivity state $(k_{\min})$ and then progress to some higher reactivity state $(k_{\max})$ over a given time interval (t_{refl}). For a step insertion, the system multiplication factor was assumed to instantaneously switch at the reflector insertion time.

Other types of insertions beyond ramps are also feasible but were excluded from analysis. A simple step or ramp insertion was sufficient to capture the principle behind reactivity addition as a function of time.

3.6 Backward v. Forward

Prior to proceeding further, discussion is warranted regarding the forward and backward equations. The forward derivation was presented previously and both forms are useful for analysis. In the discussion of Markov chains the concepts of forward and backward equations are routinely used. In reactor systems forward equations are typically the most common and intuitive. Namely, as one neutron is injected into the reactor, the progeny are followed as a function of time. The number of neutrons at future times is initially dependent upon the initial condition; namely one or more neutrons at the injection time but at later times future states are independent of the initial condition. In nominal reactor calculations, forward based problems are used to describe the time dependent change in neutron density as a function of time based on some initial condition.

For the forward case one is interested in the probability of any change occurring during time t and $t+\Delta t$ in which the following relation holds $P(t_2+\Delta t \mid t_1) = P(t_2+\Delta t \mid t_2)\cdot P(t_2 \mid t_1) + o(\Delta t)$. The time t_1 is initial state and subsequent changes are examined at time t_2 for which $t_2 > t_1$. For the backward case one considers a small change in the initial t_1 such that $P(t_2 \mid t_1 - \Delta t) = P(t_2 \mid t_1)\cdot P(t_1 \mid t_1 - \Delta t) + o(\Delta t)$. The time t_2 is the final state and subsequent changes are examined at time t_1 for which $t_1 < t_2$. Starting from the final state, changes are examined at previous times $(t_1 - \Delta t)$. From these two probability change relations, arguments for the forward and backward equations can be derived and their equivalence can be shown (Harris 1963).

Noting that all coefficients in the forward and backward probability equations are finite, it has been shown by many authors that both forms are mathematically equivalent (Feller 1968, Lewins 1978, Salmi 1980, Harris 1983, Harris 1989). The fundamental difference between the two forms is how the time parameter is treated. In the forward derivation, the initial time t_0 is held fixed, and all information about the system is known, while future times t, such that $t > t_0$, are treated as variable. The backward equation considers the terminal time t_f as fixed, and all information about the system is known, while the previous times s, such that $s < t_f$, are treated as variable. If the properties of the system are time independent, the solution then depends only on the total time magnitude (either from the initial condition or the time to the terminal condition) $\tau = t - s$ such that $-\frac{\partial G}{\partial s} = \frac{\partial G}{\partial t}$ (Lewins 1981). The major difference between the two formalisms is that the forward derived equation is linear whereas the backward equation is non-linear. Such non-linearity in the backward form will be addressed below. The time domain is then treated as the time magnitude from the initial condition or the time to the terminal condition, and only the time magnitude is important.

Time dependent backward or adjoint calculations are formulated similarly as the forward equation. Namely, the initial condition is reversed such that the system is now defined by a terminal condition. Adjoint calculations are typically best understood as importance functions. In particular, for a neutron injected into some medium at a given time, the problem solved is the importance at some later time. The backward equations seek to answer the question that if a neutron is injected into a medium at some point in the past at

time s, what is the probability it will not become extinct over the time interval of $t_f - s$?. A non-zero non-extinction probability highlights that neutrons will still be present at this later. In the backwards case, one injects neutrons at the initial time while assuming that the chain has not become extinct at the terminal condition.

Despite the different types of formalisms, both are used in the support of this work. The solutions for $P_N(t)$ shown above and the Monte Carlo results presented in later sections are of the forward type. The initial source neutron is tracked forward in time until its progeny die or diverge. The non-extinction probability equation used throughout the remainder of this work is the backward type. Problems arise with the forward formalism as closed form solutions cannot be obtained. Only the backwards probability balance yields a closed form solution which can readily be solved.

3.6.1 Backward Equation

The backward equation provides an alternative but equivalent formulation of the time dependent neutron number probability in a zero dimensional setting. It differs from the forward equation in that the probability balance is constructed by considering independent and mutually exclusive events that contribute to a fixed final state and time following an infinitesimal change in the injection time of an initiating neutron. Since the initial time becomes the independent variable while the final time is fixed, the equation is accordingly referred to as a backward in time equation. As we will see, however, the backward equation is a nonlinear equation with respect to the appropriate probability as

well as the generating function, but as will also be shown, the backward formulation provides a natural setting when generalizing the stochastic model to accommodate phase space coordinates.

The difference between the forward and backward cases arises from the fission neutrons produced. In the forward equation the probability balance was built around any one of the $N+1-\nu$ present at time t causing a fission event and the resulting ν neutrons produced (minus the parent) would then contribute to N neutrons being present at time $t+\Delta t$. The backward balance is similar, except the difference is that $(\nu-1)$ neutrons produced by the initial neutron having a fission reaction at time $(s+\Delta s)$ leading, through their own progeny, to exactly N neutrons being present at the terminal time.

In order to derive the backward equation, let $P_N\left(t_f \mid s\right)$ be the probability of N neutrons being present at the terminal time t_f, which is fixed, given that one neutron was injected at some variable initial time s. Consider now the same probability at a short time Δs after injection of the initial neutron. A probability balance of all independent and mutually exclusive events then yields:

$$P_N(t_f \mid s) = \underset{\text{a}}{\left(1-\lambda_T \cdot \Delta s\right)} \cdot \underset{\text{b}}{P_N(t_f \mid s+\Delta s)} + \underset{\text{c}}{\lambda_C \cdot \Delta s \cdot \delta_{N,0}} + \underset{\text{d}}{\lambda_F \cdot \Delta s \cdot \sum_{m_1+m_2+\ldots m_n=N} \cdots \sum p_i \cdot P_{m_1}\left(t_f \mid s+\Delta s\right) \cdot P_{m_2}\left(t_f \mid s+\Delta s\right) \cdots P_{m_k}\left(t_f \mid s+\Delta s\right)} + o(\Delta s) \tag{27}$$

a. Probability that N neutrons are present at time t_f given one neutron injected at initial time s.

b. Probability of no interactions occurring in time Δs after injection multiplied by the probability that the initial neutron at time $s+\Delta s$ will lead to N neutrons at time t_f.

c. Probability that the initial neutron will be parasitically captured over the interval Δs and this event will only contribute to the final state only if $N=0$ at t_f.

d. Probability that the initial neutron has a fission reaction over interval Δs times the probability of one, two, or multiple neutron emissions with probability p_i, each of the latter creating progeny such that there are a total of N neutrons at t_f. As each fission neutron develops its progeny independently, the probabilities of the individual chains are multiplied to yield the given final state.

Rearranging and taking the limit as $\Delta s \to 0$, the nonlinear backward equation is obtained:

$$-\frac{1}{v}\cdot\frac{\partial P_N\left(t_f \mid s\right)}{\partial s}+\lambda_T\cdot P_N\left(t_f \mid s\right)=\lambda_S\cdot P_N\left(t_f \mid s\right)+\lambda_C\cdot\delta_{N,0}\cdot P_N\left(t_f \mid s\right)$$
$$+\lambda_F\cdot\sum_i p_i\cdot\prod_{j=1}^{i}P_{N_j}\left(t_f \mid s\right) \tag{28}$$

where for each of the fission terms, $N_1+\cdots+N_i=N$. Eq. 28 is also subject to a terminal condition of:

$$P_N\left(t_f \mid t_f\right)=\delta_{N,1} \tag{29}$$

Due to the non-linearity, solution of the backward equation is considerably more challenging than the forward case. However, by converting this to an equation for the generating function, certain advantages will accrue. Thus, multiplying all terms by x^N and summing over all N yields:

$$-\frac{1}{v}\cdot\sum_{N=0}^{\infty}x^N\cdot\frac{\partial P_N\left(t_f \mid s\right)}{\partial s}+\sum_{N=0}^{\infty}x^N\cdot\lambda_T\cdot P_N\left(t_f \mid s\right)=\sum_{N=0}^{\infty}x^N\cdot\lambda_C\cdot\delta_{N,0}+$$
$$\lambda_F\cdot\sum_{N=0}^{\infty}\sum_i p_i\cdot\prod_{j=1}^{i}x^N\cdot P_{N_j}\left(t_f \mid s\right) \tag{30}$$

Introducing the generating function as before, namely:

$$G\left(x,t_f \mid s\right)=\sum_{N=0}^{\infty}x^N\cdot P_N\left(t_f \mid s\right) \tag{31}$$

Manipulating the summation terms, Eq. 30 eventually yields the following:

$$-\frac{1}{v}\cdot\frac{\partial G(x,t_f\mid s)}{\partial s}+\lambda_T\cdot G(x,t_f\mid s)=\lambda_c+\lambda_F\cdot\sum_{i=1}\frac{\chi_i}{i!}\cdot G(x,t_f\mid s)^i \tag{32}$$

subject to a terminal condition of:

$$G(x,t_f\mid t_f)=x \tag{33}$$

Setting x to zero in the generating function yields:

$$G(x,t_f\mid s)\Big|_{x=0}=\sum_{N=0}^{\infty}x^N\cdot P_N(t_f\mid s)\Big|_{x=0}\equiv P_0(t_f\mid s) \tag{34}$$

where $P_0(t_f\mid s)$ is just the extinction probability. Similarly setting $x=0$ in Eq. 32 we see that the generating function equation is equivalently an equation for the extinction probability:

$$-\frac{1}{v}\cdot\frac{\partial P_0(t_f\mid s)}{\partial s}+\lambda_T\cdot P_0(t_f\mid s)=\lambda_c+\lambda_F\cdot\sum_{i=1}p_i\cdot P_0(t_f\mid s)^i \tag{35}$$

It is noted that it is not possible to write down a closed form equation for the extinction probability in the forward formulation but although this becomes possible in the backward approach, it comes at the price of nonlinearity. Of greater interest in this work is the non-extinction probability which is given by the complementary event $P_{NE}\left(t_f \mid s\right) = 1 - P_0\left(t_f \mid s\right)$. Expressing the non-extinction probability as $p\left(t_f \mid s\right)$, Eq.(35) becomes:

$$\frac{1}{v} \cdot \frac{\partial p\left(t_f \mid s\right)}{\partial s} + \lambda_T \cdot \left(1 - p\left(t_f \mid s\right)\right) = \lambda_c + \lambda_F \cdot \sum_i p_i \cdot \left(1 - p\left(t_f \mid s\right)\right)^i \tag{36}$$

The fission term can be simplified by applying a binomial expansion:

$$\left(1 - p\left(t_f \mid s\right)\right)^i = \sum_{k=0}^{i} (-1)^i \cdot \binom{i}{k} \cdot p\left(t_f \mid s\right)^i \tag{37}$$

to eventually obtain the non-linear backward time dependent non-extinction probability equation:

$$-\frac{1}{v} \cdot \frac{\partial p\left(t_f \mid s\right)}{\partial s} + \lambda_T \cdot p\left(t_f \mid s\right) = \bar{\nu} \cdot \lambda_F \cdot p\left(t_f \mid s\right) + \lambda_F \cdot \sum_{i=2}^{\nu_{\max}} (-1)^i \cdot \frac{\chi_i}{i!} p\left(t_f \mid s\right)^i \tag{38}$$

where the χ_i constants are the same as defined earlier and take into account the fission multiplicity data.

CHAPTER 4: NUMERICAL MODELING – 0-D

The modeling efforts of this section were geared towards numerical solution of the deterministic non-extinction probability equation. Solutions to this equation lead to an understanding of the time dependent behavior in prompt critical systems. Numerical results are presented for a wide variety of cases. These include static, step, and ramp insertions of reactivities as well as inclusion of an external source. Parameters applicable to SPR operation are also used and varied to understand the sensitivity of these terms on the non-extinction probability (see Appendix A for more details). The 0-D case for the monoenergetic non-extinction probability is presented below. The backward time dependent non-extinction probability 0-D equation is:

$$-\frac{1}{v}\cdot\frac{dp}{dt}+\Sigma_A\cdot p=\left(\Sigma_C+\bar{\nu}\cdot\Sigma_F\right)\cdot p-\Sigma_F\cdot\sum_{i=2}^{7}\left(-1\right)^i\cdot\frac{\chi_i}{i!}\cdot p^i \tag{39}$$

with

$$p(t_f)=1.0 \tag{40}$$

This equation can be recast into an alternate form that makes it useful for interpretation of the infinite eigenvalue by recognizing that $l \equiv \frac{1}{\nu \cdot \Sigma_A}$, using a shifted time index $t^* = t_f - t = t$, and inserting:

$$l \cdot \frac{dp}{dt} = [k-1] \cdot p - \frac{\Sigma_F}{\Sigma_A} \cdot \sum_{i=2}^{7} (-1)^i \cdot \frac{\chi_i}{i!} \cdot p^i \tag{41}$$

with

$$p(0) = 1.0 \tag{42}$$

and also noting that $k = \frac{\bar{\nu} \cdot \Sigma_F}{\Sigma_A}$.

4.1 Examination of Non-Linear Terms

The non-linear terms in the non-extinction probability are what makes the equation unique relative to the neutron transport equation. Prior to solving the non-extinction probability equation, an investigation into the behavior of these non-linear terms is warranted. The general form of the linear and non-linear fission terms takes the following form:

$$L_F - N_F[L] = \bar{\nu} \cdot \Sigma_F \cdot p(t) - \Sigma_F \cdot \sum_{i=2}^{7} (-1)^i \cdot \frac{\chi_i}{i!} \cdot p(t)^i \tag{43}$$

It is advantageous to spend some time understanding the nature of $N_F[L]$. As noted by Bell (1963), the entire summation of the non-linear terms is always positive. With the negative sign in front of the summation, the non-linear terms always have a time absorptive effect.

The non-linear terms represent the mean number of neutron groupings emitted per fission (pairs, triplets, etc.). The quadratic truncation frequently used cuts off the fission multiplicity at 2. To help the reader better understand how these truncations impact the overall fission term, several simple graphs are included for illustration.

Using a fission cross-section of 0.04164 cm^{-1}, the non-linear terms versus p are plotted in the figure below for each of the non-linear terms by themselves. Thus the p^2 term is only for the quadratic term, the p^3 term is only for the cubic term, and so on.

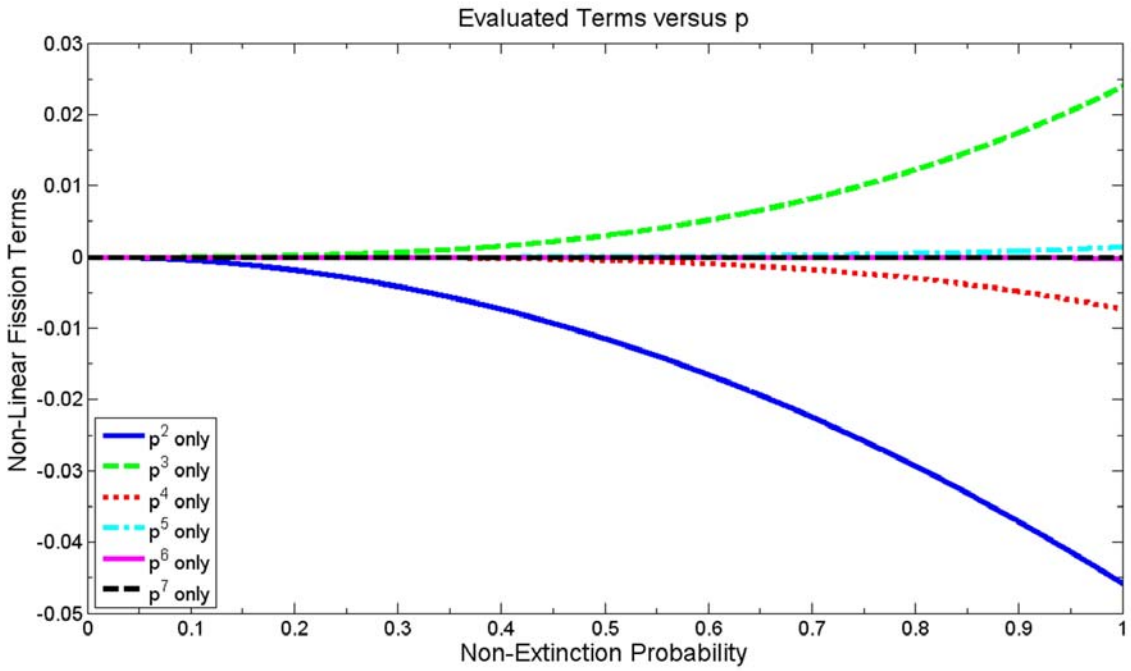

Figure 10: Magnitude of the non-linear terms versus non-extinction probability.

The figure illustrates the magnitude of each of the non-linear terms. The negative sign outside the summation is included such that each of the even powered terms is negative. Only the odd powered terms show some positive behavior, with the cubic term showing the largest positivity. For powers of fifth order or higher, the overall magnitude of terms is sufficiently small due to the high power in *p* and also the inverse factorial term. The entire non-extinction probability domain is necessary to plot as the terminal condition fixes the probability to one. It will be shown later that the systems of interest in this work have small POI values. One must then integrate in time until the POI value is reached; thus the non-extinction probability domain shown above is traversed.

To highlight the difference of the non-linear terms in the summation, the figure below is provided. The linear term is shown and then subsequently adds on the non-linear terms one by one. This process proceeds through the full multiplicity. Consequently, the overall importance of the non-linear terms can be seen in aggregate as well as the importance of the truncation of non-linear terms retained.

The notation in the figure below is according to the following. The solid red curve "L_F" represents the linear fission term. The dashed blue curve "L_F-[p^3]" represents linear minus the sum of the quadratic and the cubic term and so on.

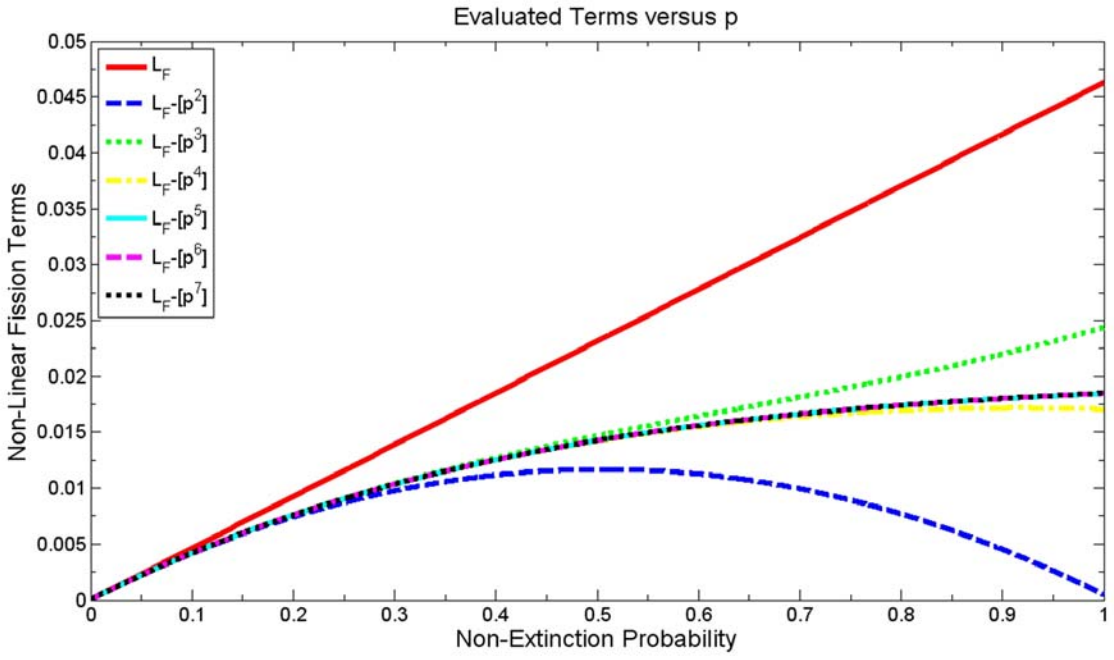

Figure 11: Overall importance of the non-linear terms on the fission term.

It is interesting to note that the quadratic curve exhibits significant curvature and almost drives the fission terms to zero near the probability of one. The higher order fission terms exhibit oscillatory behavior due to the $(-1)^i$ term in the summation. The quadratic and cubic terms underestimate and overestimate the fission importance, respectively. As noted earlier, for terms five or higher there is a negligible change in the combined fission term. Regardless of the summation truncation used, the non-linear terms do indeed have an absorptive effect on the fission term.

Several conclusions can be drawn from the figures presented above. The non-linear terms act as a time absorber in the system. For any fission truncation used, the effective system reactivity with these terms is lower than in the standard eigenvalue calculation. It is noted that the quadratic truncation differs significantly from the full multiplicity. Thus it can be expected that the time dependent results for the quadratic case will slightly underestimate the non-extinction probability compared to the full multiplicity while the system is relaxing to the POI.

4.2 0-D Iteration Routine

Solutions were sought for the time dependent non-extinction probability. Two methods were sought for solution, one in which the roots of the above equation were solved explicitly and the other method used a Newton iteration routine. With the Newton routine, the solution within a timestep is iterated upon until convergence is achieved. It was found that this method was significantly faster than the polynomial solver. This was

not surprising as much time is spent calculating all the roots. It should be noted that $x = 0$ is a root and there is always one root which is positive and is bounded between zero and one. The Newton routine proved to be sufficiently fast that resolution of the time domain was readily seen. Across the time domain the number of Newton iterations per timestep was on the order of 3-5. The breakdown of the Newton routine used is provided below. The routine uses a fully implicit time discretization.

Let n denote the solution at the current timestep and *n+1* the solution at the next timestep. When $n = 0$, this corresponds to $t = t_0$. Recasting the non-extinction probability equation:

$$\frac{p_{n+1} - p_n}{\Delta t} = g\left(p_{n+1}\right) \tag{44}$$

where

$$g\left(p_{n+1}\right) = \frac{1}{l} \cdot \left[\left(k_\infty - 1\right) \cdot p_{n+1} - \frac{\Sigma_F}{\Sigma_A} \cdot \sum_{i=2}^{7} \left(-1\right)^i \cdot \frac{\chi_i}{i!} \cdot {p_{n+1}}^i \right] \tag{45}$$

Rearranging

$$p_{n+1} - p_n = \frac{\Delta t}{l} \cdot g\left(p_{n+1}\right) \tag{46}$$

Let:

$$h\left(p_{n+1}\right) = p_{n+1} - p_n - \frac{\Delta t}{l} \cdot g\left(p_{n+1}\right) \tag{47}$$

Performing a Taylor's series expansion on *h*, and neglecting the derivative terms of second order and higher:

$$h(p) + \Delta p \cdot h'(p) = 0 \tag{48}$$

$$\Delta p = -\frac{h(p)}{h'(p)} = -\frac{p_{n+1} - p_n - \frac{\Delta t}{l} \cdot g(p_{n+1})}{1 - \frac{\Delta t}{l} \cdot g'(p_{n+1})} \tag{49}$$

Within a timestep, the variable k is used to denote the Newton iteration index.

$$p^{(k+1)} - p^{(k)} = -\frac{p_{n+1} - p_n - \frac{\Delta t}{l} \cdot g(p_{n+1})}{1 - \frac{\Delta t}{l} \cdot g'(p_{n+1})} \tag{50}$$

The Newton iteration is performed until the successive difference between iteration steps is within the desired error criteria.

4.3 Zero Source - Static Reactivity

Using the Newton iteration routine outlined above, the time dependent non-extinction equation is initially solved for the full fission multiplicity data. The case for static reactivity is presented below. The systems are taken to be at a fixed multiplication factor for all times. The time dependent solution is plotted for several multiplication factors to highlight the subsequent difference on the time dependent behavior.

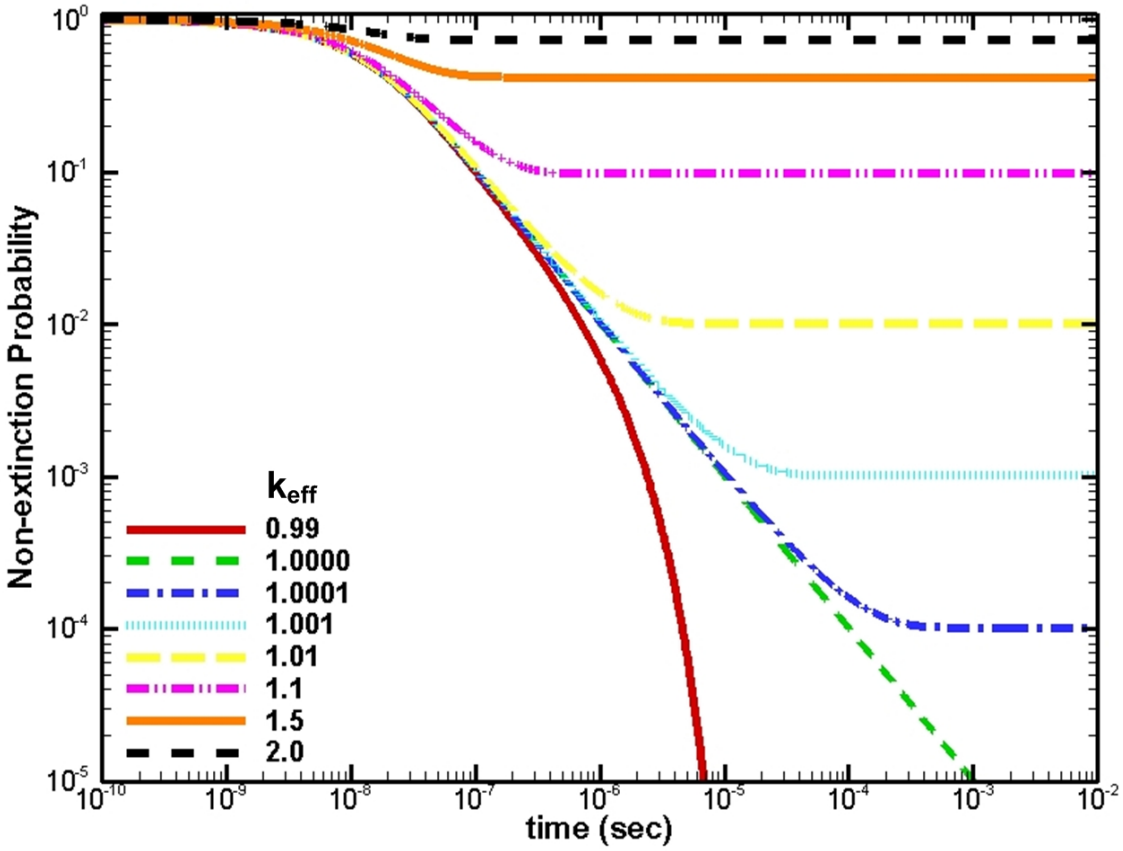

Figure 12: Time dependent non-extinction probability for fixed reactivity.

The time dependent solutions initially exhibit similar behavior for early times. For high system reactivities, the steady state POI is reached rapidly. As the multiplication factor is decreased, the time to reach the steady state solution increases and the resulting magnitude of the solution decreases. Note that the time scales at which the steady state values are reached are significantly different (results presented on a log-log scale). Thus there is a significant time lag for weakly prompt critical systems before the steady state solution is reached. For a system exactly critical, the non-extinction probability tends to zero for infinite times. This result is non-obvious as the ratio of production to losses is unity and one would expect the solution to tend to a constant. The subcritical cases also tend to zero, yet at a much faster rate as expected.

One can see that eventually the asymptotic SS POI value is reached for all prompt critical systems. Thus a neutron injected over this time interval will either become divergent or extinct. The SS POI represents the fraction of such divergent chains. For low prompt critical systems, the resulting POI value is low. As the system reactivity is increased the POI approaches values close to one. For times close to the initial condition the non-extinction probability is near unity. Given the time magnitude from the initial condition is small, sufficient time has not elapsed for a divergent chain to develop. One can see in the figure that there is significant multiplication for the high multiplication factor cases such that the non-extinction probability asymptotes rapidly. Even for the subcritical case shown in the figure, a significant period of time must elapse before the chain can be said to become fully extinct. Thus the greater the chance for the source neutron to multiply, the greater the chance it will exist at later times from the injection time.

4.3.1 Timestep Analysis

As with any numerical integration routine, the timestep selected can play a large role on the overall results. This is particularly true as the differencing scheme used for the Newton routine is $o(\Delta t)$. Given the non-linearity of the problem, the timestep of the solution was thoroughly studied. In particular, in order to obtain the exact description for the time dependent behavior, one must choose a sufficiently small timestep. For Figure 12, a timestep of 0.1 ns was used for an effective neutron lifetime of 10 ns. As the

simulation timestep is increased, a deviation in the time dependent behavior is seen. The figure below illustrates these behaviors.

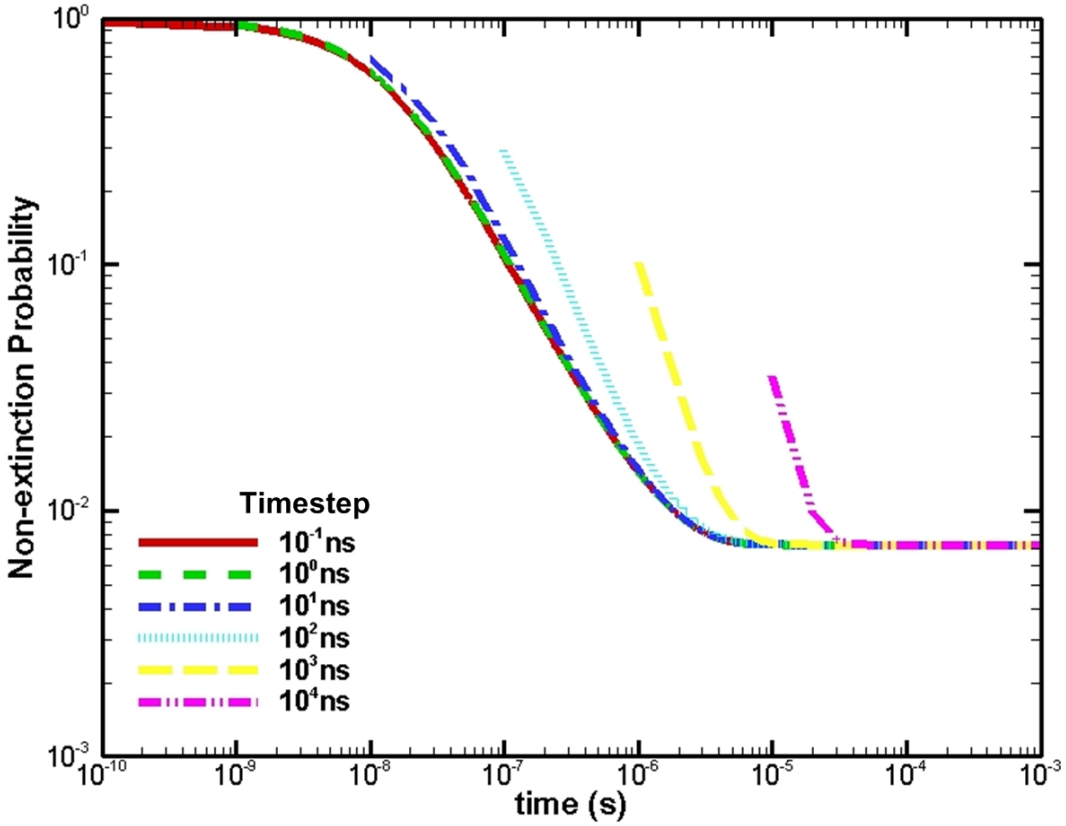

Figure 13: Importance of timestep on time dependent solution.

For timesteps less than the assumed neutron lifetime (10ns), the timestep is sufficiently small that there is negligible change in the time dependent solution. Thus if one is interested in the time dependent behavior, timesteps smaller than the neutron lifetime should be used. It is interesting to note that even though large timesteps lead to large deviations in the initial time dependent solutions, these cases always converge to the exact same steady state non-extinction probability. The utility of this point is such that if only the steady state value is sought, large timesteps may be used. The initial time

dependent behavior will not be correct; however, the steady state value will be reached. In order to obtain a benchmark on the time dependent behavior, solution of the differential equation is necessary. Comparison of the analytic to the numerical solution is discussed in the next section.

4.3.2 Analytical v Numerical Solution

To ensure the numerical results obtained from the Newton routine were correct, a comparison can be made against an exact analytical solution. To develop the analytical solution, the quadratic truncation must be invoked. The quadratic analytical solution for constant reactivity is presented below. The backward equation with the quadratic non-linear truncation is:

$$-\frac{1}{v}\cdot\frac{dp}{dt}+\Sigma_T\cdot p=\left(\Sigma_S+\bar{\nu}\cdot\Sigma_F\right)\cdot p-\Sigma_F\cdot\frac{\chi_2}{2}\cdot p^2 \tag{51}$$

with $-\infty < t \le t_f$ and $p\left(t_f\right)=1.0$

With some re-organization:

$$-\frac{dp}{dt}=v\cdot\Sigma_A\cdot\left(k-1\right)\cdot p-v\cdot\Sigma_F\cdot\frac{\chi_2}{2}\cdot p^2 \tag{52}$$

Eq. 52 is then divided by p^2 and is shown to satisfy a Ricotti equation:

$$-\frac{1}{p^2}\cdot\frac{dp}{dt}=v\cdot\Sigma_A\cdot\left(k-1\right)\cdot\frac{1}{p}-v\cdot\Sigma_F\cdot\frac{\chi_2}{2} \tag{53}$$

Let $r(t) = 1/\,p(t)$ such that $\frac{dr}{dt} = -\frac{1}{p^2} \cdot \frac{dp}{dt}$ and substituting

$$\frac{dr}{dt} = \nu \cdot \Sigma_A \cdot (k-1) \cdot r - \nu \cdot \Sigma_F \cdot \frac{\chi_2}{2} \tag{54}$$

with

$$r(t_f) = 1/\,p(t_f) = 1.0 \tag{55}$$

The solution of which is:

$$r(t) = e^{-\nu \cdot \Sigma_A \cdot (k-1) \cdot (t_f - t)} - \frac{\Sigma_F \cdot \chi_2}{2 \cdot \Sigma_A \cdot (k-1)} \cdot \left[e^{-\nu \cdot \Sigma_A \cdot (k-1) \cdot (t_f - t)} - 1 \right] \tag{56}$$

The solution for $p(t)$ is then:

$$p(t) = \frac{1}{e^{-\nu \cdot \Sigma_A \cdot (k-1) \cdot (t_f - t)} - \frac{\Sigma_F \cdot \chi_2}{2 \cdot \Sigma_A \cdot (k-1)} \cdot \left[e^{-\nu \cdot \Sigma_A \cdot (k-1) \cdot (t_f - t)} - 1 \right]} \tag{57}$$

The time dependent non-extinction probability can be plotted graphically for all times. It can be shown that the solution tends to the steady state POI value as predicted by Bell.

As $t \to -\infty$

$$p(-\infty) = \frac{1}{r(-\infty)} = \frac{2 \cdot \bar{\nu} \cdot (k-1)}{k \cdot \chi_2} = POI \tag{58}$$

Using a constant system multiplication factor of 1.0072, the analytical solution is plotted against numerical results. The figure below includes the analytic time dependent solution (using the shifted time index) and both the quadratic and full multiplicity numerical solutions for illustration. A timestep of 1 ns was used.

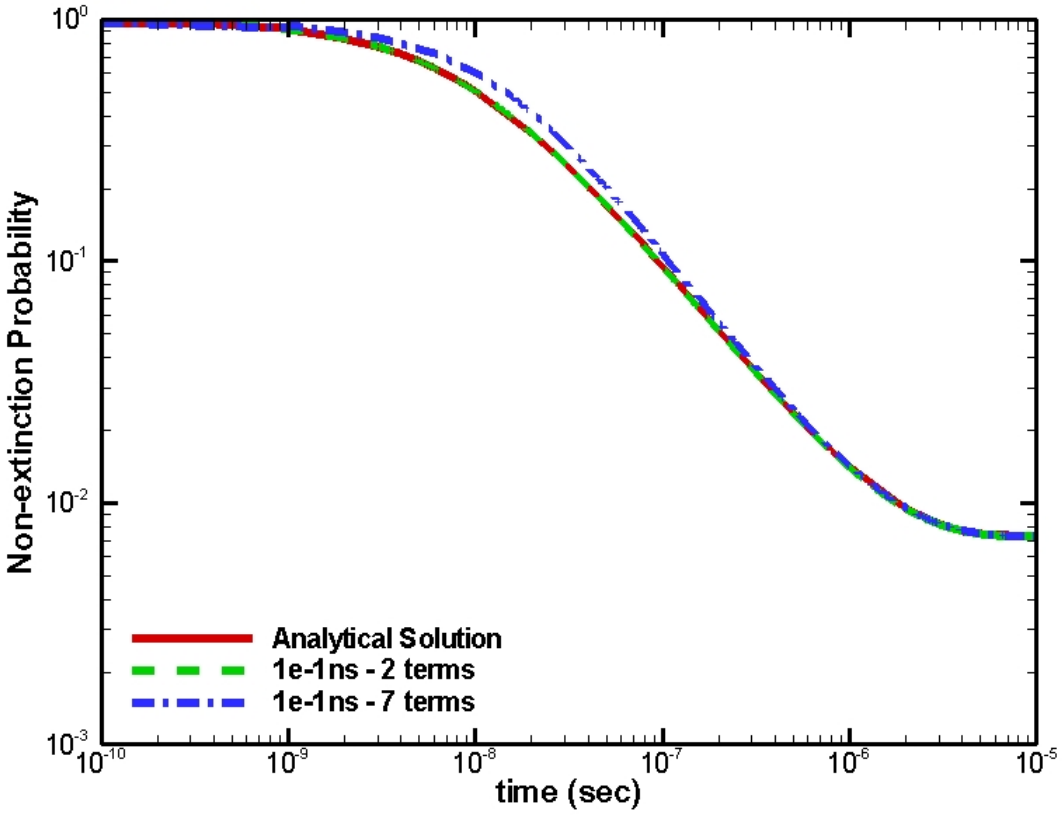

Figure 14: Comparison of analytical and numerical results.

For both multiplicities presented, the numerical solution matches well with the analytical solution. The full seven term multiplicity shows a slight difference in the solution around injection times a few lifetimes from the initial time. After this both of the multiplicities approach the steady state solution with excellent agreement over the entire time domain.

It was noted by Bell that the quadratic truncation is a good approximation to the entire fission multiplicity data for low prompt reactivities. To quantify the magnitude of the approximation and resulting limit of the quadratic truncation, the roots of the 0-D equation were solved for all truncations for the SS POI.

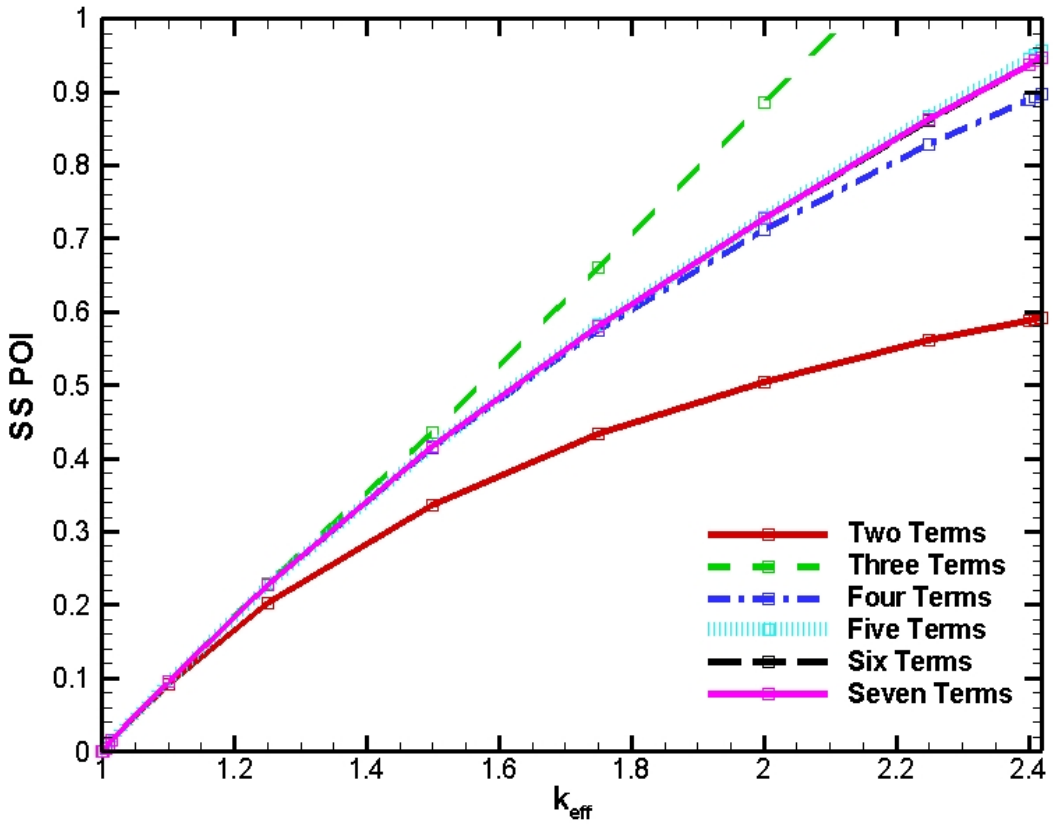

Figure 15: Steady state POI solution versus system reactivity.

For the broad range of system eigenvalues, there is a substantial difference seen in the SS POI. For the effective range of interest for this work, $k_{eff} \cong 1$, there is negligible difference between the quadratic and seventh order SS solution (confirming the results seen in Figure 14). Only for multiplications above 1.2 is there a noticeable difference. It should also be noted that even as the infinite eigenvalue approaches $\bar{\nu}$, the SS POI does

not go to one. Thus if such a system could exist, the results show that there is no guarantee that a given single source neutron will lead to a divergent chain.

For comparison, the SS POI for selected cases using the full multiplicity are shown in the table below. In addition, the SS POI for the probability of developing a divergent chain (using the quadratic truncation) is also presented for comparison (Bell 1963).

Table 4: Comparison of numerical POI to infinite medium values.

k	SS POI	Bell's $p(t_0)$
1.0001	0.000101	0.000101
1.001	0.001009	0.001009
1.01	0.010050	0.009997
1.1	0.096522	0.091793
1.25	0.227099	0.201944
1.5	0.416543	0.336574
1.75	0.580968	0.432738
2.0	0.727839	0.504861

For low prompt reactivities, the numerical solution is identical to Bell's analytical formula. Once the system multiplication factor exceeds ~1.1, deviations in the steady state POI can be found. If one is only interested in the SS POI, Bell's formula is sufficient for all reactivity ranges of interest to fast burst operation.

For multiplication factors close to one, the resulting time to SS becomes increasingly long. This can be problematic for the systems of interest in this work as one must integrate out to exceedingly long times to reach the SS value. For the weak prompt critical case of $k = 1.0001$ shown in the figure above, the resulting time to SS was 0.0233 seconds. For a timestep of 1.0 ns, this equates to a total 23,300,000 timesteps needed to reach SS.

4.4 Zero Source - Dynamic Reactivity

Although the results presented above for static systems yield insight into the time dependent non-extinction probabilities, FBRs rely on dynamic reactivity insertions for pulse operations. Focus is extended to a dynamic reactivity insertion. For systems like SPR, the reactivity insertion can be modeled as a ramp insertion. For comparison to the numerical results, an exact analytical solution was found for a step insertion case.

4.4.1 Analytical v Numerical Solution

For the dynamic multiplication case, the system is taken to be at some minimal eigenvalue for times near the terminal condition. At a time of t_{refl}, (reflector insertion time) the effective multiplication factor is instantaneously increased to some maximum value for all previous times. Using this reactivity scheme, the following analytical solution is obtained.

for $t < t_{refl}$, $k(t) = k_{\max}$

$$p(t) = \frac{1}{e^{-\left[A\cdot(t_r - t) + B\cdot(t_f - t_r)\right]} + \nu\cdot\Sigma_F\cdot\frac{\chi_2}{2}\cdot\left[-\frac{1}{A}\cdot\left[e^{-A\cdot(t_r - t)} - 1\right] - \frac{1}{B}\cdot e^{-\left[A\cdot(t_r - t) + B\cdot t_r\right]}\cdot\left[e^{-B\cdot t_f} - e^{-B\cdot t_r}\right]\right]} \tag{59}$$

where $A = \nu\cdot\Sigma_A\cdot(k_{\max} - 1)$ and $B = \nu\cdot\Sigma_A\cdot(k_{\min} - 1)$

for $t_{refl} < t < t_f$, $k(t) = k_{\min}$

$$p(t) = \frac{1}{e^{-B\cdot(t_f - t)} \cdot \left[1 - \frac{\Sigma_F \cdot \chi_2}{2 \cdot \Sigma_A \cdot (k_{\min} - 1)}\right] + \frac{\Sigma_F \cdot \chi_2}{2 \cdot \Sigma_A \cdot (k_{\min} - 1)}} \tag{60}$$

Using the Newton iteration routine, the time dependent solution is plotted in the figure below. For the dynamic reactivity case, the following values were used: $l = 10^{-8}$ sec, $k_{\min} = 1.0001$, $k_{\max} = 1.0072$, $t_f = -10^{-10}$ sec, $t_{refl} = -10^{-5}$ sec. In addition, two cases are also presented for the fixed multiplication factors (k_{min} and k_{max}).

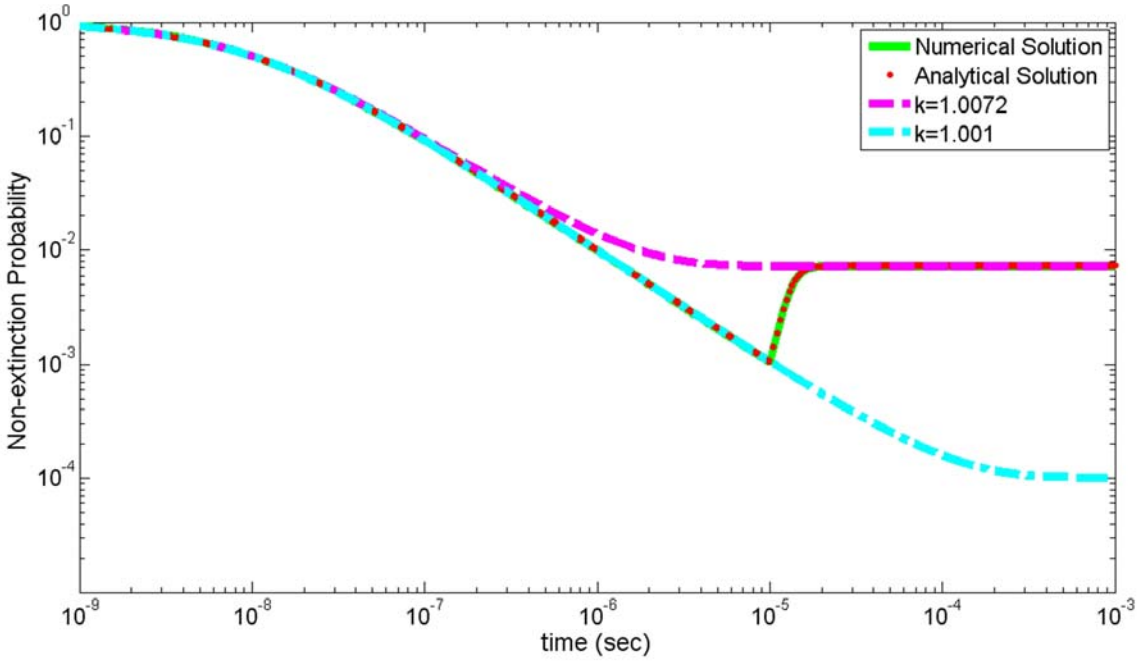

Figure 16: Time dependent non-extinction probability for a step insertion.

The analytical solution is plotted with red dots. The numerical solution is plotted with a solid green line. The solutions are identical over the entire time domain. For times far from the initial time, the solution reaches the steady state value corresponding to the maximum reactivity state. For the region of the time domain where the multiplication factor is changing, the time dependent solution has a sharp bend with the minimum corresponding to the minimal multiplication factor. Thus for a neutron inserted just prior to the point at which the reactivity was increased, the non-extinction probability is at its lowest value and then increases to the terminal condition. Once the reactivity state is changed, there is a finite period of time where the solution is between the curves for the maximum and minimum non-extinction probabilities. These times may be considered to be in a transitionary state until the system reaches the final multiplication factor and the resulting solution relaxes to the SS POI at that corresponding multiplication factor. Thus at times prior to the point at which the reactivity is switched the solution decays according to the lower multiplication factor solution and then jumps to the final state. From the results presented in the figure, it was concluded that excellent agreement was seen between the numerical and analytical results.

4.4.2 Dynamic Reactivity Results

The time dependent solutions for varying reactivity states forces the non-extinction probability to see deep "dips" in magnitude while the system is subcritical. Once the system crosses critical, the solution is forced to bend around. The final system multiplication factor drives the time behavior relative to the terminal condition. Using a ramp insertion and the same numerical timestep, the time at which all of the reactivity was inserted was varied for illustration. Due to the initial subcritical nature of the problem, the time the system spends in a subcritical state plays a large role on the time dependent behavior. The importance of the insertion time is shown in the figure below where the initial multiplication factor $k = 0.99987$ was used, the final multiplication factor was fixed to $k = 1.01$, and the time over which the reactivity was inserted was varied.

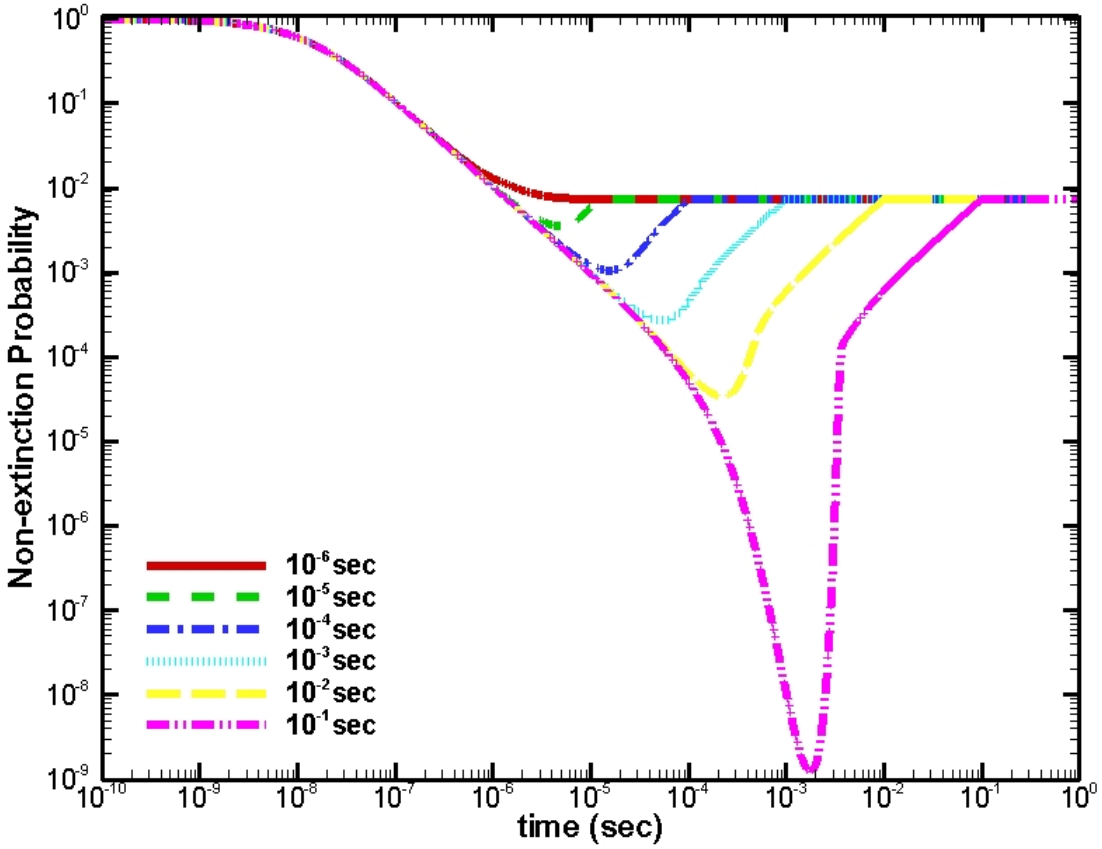

Figure 17: Non-extinction probability for a ramp insertion v different insertion times.

As the reactivity insertion time is decreased, there are significant dips seen in the time dependent non-extinction probabilities. This is due to the amount of time the system sits at a subcritical state. For any of the cases, once critical is crossed each of the curves turns around. After sufficient times from the injection time, each of the cases yields the same POI. For cases where the reactivity was inserted quickly (10^{-6} s), there is little change seen in the time dependent results. As the insertion time is slowed down, the non-extinction probability endures a steep decline for times away from the steady state or initial value.

4.5 Source Extension

It is worthwhile to note that if the time dependent behavior of a single neutron can be calculated, incorporation of many such particles is rather straightforward. It was noted by Bell that if a source of neutrons is incorporated into the model, the resulting generating function is merely a product of all of the individual generating functions due to the Markovian nature of the low neutron number systems (Bell 1965). It was shown by both Bartlett and Humbert that if the generating function for a single neutron can be found then the resulting generating with the source can be found from (Barlett 1978, Humbert 2003):

$$G_{SOURCE}\left(x,t_f \mid 0,t\right)=\exp\left\{\int_t^{t_f} d\tau\cdot\int_r d\vec{r}\cdot S\left(\vec{r},\tau\right)\cdot\left(G\left(x,t_f \mid 1,t\right)-1\right)\right\} \tag{61}$$

Relating back to the quantity of interest, the non-extinction probability with a source is $1-\left(G_{SOURCE}\left(x,t_f \mid 0,t\right)\right)_{x=0}$. In the case of a spontaneous fission source, one must account for the probability, q_i, of i neutrons emitted from the fission event.

Inclusion of a source in the problem can be performed using the solution of the single neutron non-extinction probability and the following relation:

$$p_{SOURCE}\left(t\right)=1-\exp\left\{\int_t^{t_f} d\tau\cdot\int_r d\vec{r}\cdot\sum_{i=1}^{I} q_i\cdot S_i\left(\vec{r},\tau\right)\cdot\left[1-p\left(t_f \mid 1,\vec{r},t\right)\right]^i-1\right\} \tag{62}$$

In the case of a constant source where $I = 1$, the source non-extinction probability equation becomes:

$$p_{SOURCE}(t) = 1 - \exp\left\{ -\int_{t}^{t_f} d\tau \cdot \int_{r} d\vec{r} \cdot S(\vec{r}, \tau) \cdot p(t_f \mid 1, \vec{r}, t) \right\} \tag{63}$$

Once the user has found the single neutron extinction probability the source non-extinction probability is simply found through quadrature. If the source is independent of time (and space), the source is pulled out of the integral and the user must merely integrate the resulting non-extinction probability over the interval of interest. To do this numerically, one must use small timesteps to properly account for the time integral.

Some interesting properties of the above equation can be deduced. Principally, regardless of the source strength the resulting source non-extinction probability will approach one. The counter argument may also be made if the time domain is integrated over a long enough time interval, the resulting quadrature on the non-extinction probability becomes sufficiently large regardless of the source strength.

4.6 Source Strength Examination

Discussion of neutron sources was provided earlier relative to reactor operations. Unfortunately there is some uncertainty in the overall source strength during pulse operations. It is generally assumed that the initial neutron level corresponds to that of spontaneous fission for the quantity of uranium present. This neutron level, on the average, will always be present. For SPR with the safety block lower relative to the upper half, the system is believed to be shutdown by ~ -$15. At this reactivity, there is a subcritical multiplication factor of 11.3. Given that the normal shutdown configuration of the reactor is with the core halves apart, the average neutron source in the shutdown configuration is 11.3 * 470 n/sec. During operations the lower core half is driven upwards over a period of ~ 30 seconds. Once the core half is raised, the pulse element is inserted in ~ 250 ms. The potential additional source strength increase during these times should also be taken into account. It is difficult to determine what the source strength may be during the various periods of re-configuration. One way to estimate the source is that a reasonable bounds may be set on the multiplication factor for which the minimum would correspond to that of the shutdown multiplication of 11.3 ($\rho = -\$15$) and a maximum value would correspond to that of the assembled reactivity state. With the safety block fully seated, the reactor is nominally anywhere from 2-11 ¢ sub-delayed critical (2¢ subcritical initial reactivity for a 10 ¢ pulse, 11¢ subcritical initial reactivity for a 1 ¢ pulse, etc.). Taking the worst case reactivity of just 2¢ subcritical corresponds to a subcritical multiplication factor of 7,693. Thus the maximum source strength could

be taken to be 7,693 * 470 n/sec = $3.6*10^6$ n/sec. Clearly there is a large range of potential background sources ($5.3*10^3$ – $3.6*10^6$ n/s).

Given there are timing restrictions on the source buildup, a better way to assess the increase in background source strengths would be to solve the point kinetics equations with an external source. Solution to such a problem will provide the additional source increase if the population is assumed to be deterministic. Using a point kinetics code at Sandia, this calculation was performed. The system was taken to be initially subcritical at -$15. The initial source strength corresponded to that of spontaneous fission with the subcritical multiplication factor added in. The safety block is then inserted over a period of 30 seconds to determine the net increase in source. Once the safety block is in, the pulse element insertion then begins.

The results from the calculation are as follows. The initial source was taken to be 5,311 n/s (11.3 * 470 n/s). Once the safety block was inserted in 30 seconds the resulting source strength increased to ~115,000 n/s (Parma 2008). Note that this value is bounded by that shown above. This should be no surprise as the time frame of interest is long enough that the system has had enough time to relax to its final reactivity state (this is only partially correct as the subcritical multiplication factor is constantly changing as reactivity is being added and delayed precursors are being added, thus the solution should always be lower than the subcritical multiplication corresponding the final assembly). Assessing the additional increase in the source during the pulse element insertion is difficult. In a point kinetics code, one prompt critical is crossed, the system neutron

population increases to infinity rapidly. Since the pulse element is inserted quickly, it may be assumed that the additional increase in source can be neglected. Thus the range of applicable source strengths for SPR is ($5.3*10^3$ – $1.1*10^5$ n/s).

For the range of potential source strengths, the ramp insertion case for a 10¢ pulse was selected as it leads to the worst case operational behavior. It has been shown previously that lower pulses exhibit a sharp dip in the non-extinction probability due to the system being subcritical for a long period of time. As the source non-extinction probability is the time integral of the non-extinction probability, the resulting dip in the non-extinction probability leads to a negligible change in the source non-extinction probability. Thus the time at which the source non-extinction probability goes to one is much longer for a weak pulse case than for a maximum pulse case. The 10¢ pulse case is therefore bounding for the analysis of interest here.

Using a 10¢ pulse, the single neutron non-extinction probability was calculated. For different source strengths the source non-extinction probability was calculated as a function of time for $t_{refl} = 10^{-2}$ sec.

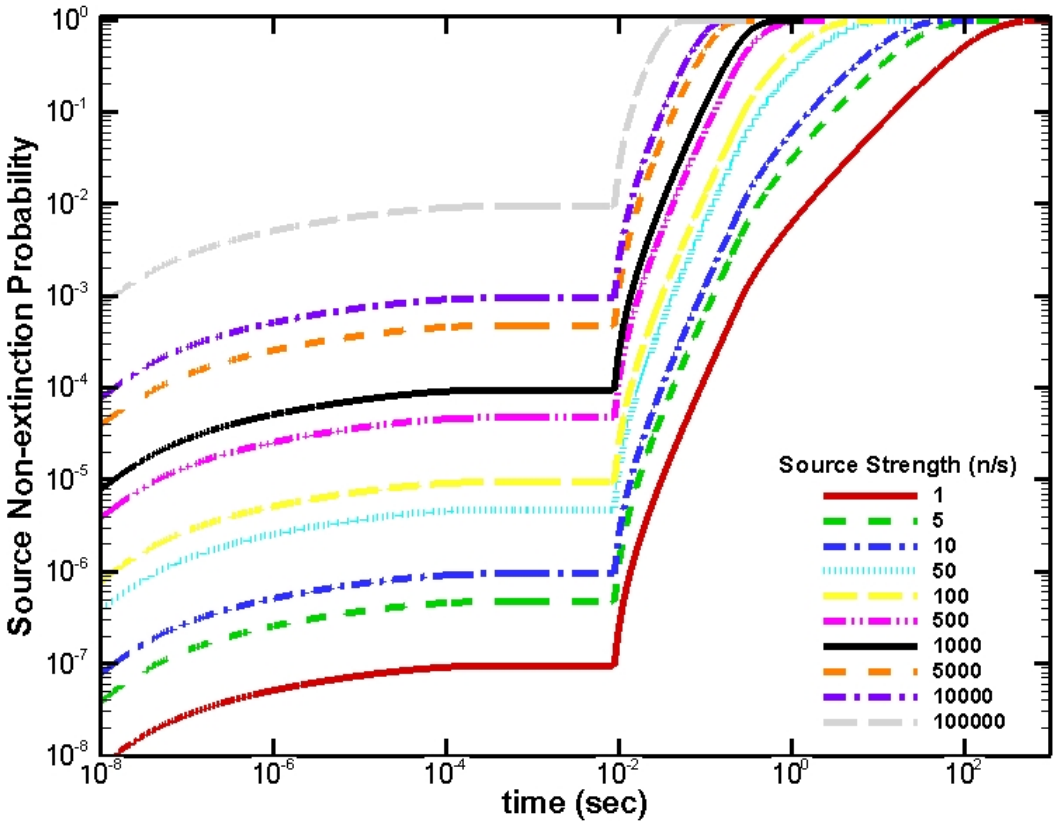

Figure 18: 10¢ pulse in 0-D for bounding source strengths.

For the different source strengths shown the time to reach a source non-extinction probability of unity varies considerably. The case of 5,000 n/s reached a source non-extinction probability of 0.9999 in 0.3835 seconds. The source case of 100,000 n/s reached a source non-extinction probability of 0.9999 in 0.08395 seconds. Increasing the source strength by a factor of 20 reduced the time to assure non-extinction by a factor of 4.5.

4.7 Pre-initiation Examination

One of the interests in this work was to determine if the pre-initiation rate on SPR could be estimated from the theory. A means to assess the magnitude of pre-initiation is to revisit one of the formulas presented in the Constant Source section. The probability of finding exactly N neutrons as a function of time with a source was shown to be found from:

$$P_N(t) = \frac{1}{[1+b(t)]^{\eta}} \cdot \frac{\Gamma(\eta+N)}{N!\Gamma(\eta)} \cdot \left(\frac{b(t)}{1+b(t)}\right)^N \tag{64}$$

where $\eta = \frac{2 \cdot S \cdot l \cdot \Sigma_A}{\Sigma_F \cdot \chi_2}$ and $b(t) = \frac{k \cdot \chi_2}{2 \cdot \bar{\nu} \cdot (k-1)} \cdot \left(\bar{n}(t) - 1\right)$

The means by which a pre-initiation is judged on SPR is if the power level reaches ~ 50 W before the burst element is fully seated. This value was chosen such that there was an appropriate trigger on reactor power and not on electrical noise (Ford 2008). The formula above can be modified to instead of yielding the probability of exactly N neutrons at time t to be the probability that the number of neutrons has not exceeded N at time t. Following the notation of Bell, the probability that the number of neutrons does not exceed N at time t, $Q_N(t)$, can be found from $Q_N(t) = \sum_{N'=0}^{N} P_{N'}(t)$. Thus by summing over neutron levels of interest at time t provides the probability that a pre-initiation has not occurred (with respect to the experimental set point). The resulting pre-initiation probability would simply be the complementary event.

Given that one is only interested in determining the probability if a pre-initiation will occur or not, the solution depends on evaluating the time integral (in the $b(t)$ term) at the reflector insertion time of 250 ms and then performing the summation up to 50 W. Some discussion on this power level is warranted. Performing this operation numerically is not feasible. The gamma function in the numerator increases at a rapid rate for large N. However in the denominator the factorial term and the gamma function are larger in magnitude for the same N. As N gets larger and larger the ratio of these two terms goes to zero. The following identity is used for further illustration: $N! = \Gamma(N-1)$. A simplification can be made to the first term in the summation by noting that for source strengths of interest to this work the value of η is sufficiently small. Thus $\frac{\Gamma(\eta+N)}{N!\cdot\Gamma(\eta)} \approx \frac{\Gamma(N)}{N!\cdot\Gamma(\eta)} = \frac{(N-1)!}{N!\cdot\Gamma(\eta)} = \frac{1}{N\cdot\Gamma(\eta)}$. As N becomes large and for small values of η, the denominator becomes vanishingly small. For source strengths of interest to this work, η is much less than one and the approximation appears to be quite valid for the low source strengths of interest (for $S=10^4$ n/s, $\eta=0.0001$). Although challenging, the term $\frac{1}{N\cdot\Gamma(\eta)}$ can be evaluated, even up to 50 W.

For late times the term $b(t)$ inside and outside the summation proves be difficult to evaluate. For late times where $\bar{n}(t)$ approaches infinity, the only parameter that varies with respect to N is the first term in the summation. The term $b(t)$ outside the summation acts as a scaling factor and for late times (where $\bar{n}(t)$ blows up) may be

approximated as: $\left(\frac{1}{POI}\right)^{-\eta} \cdot e^{-\alpha \cdot \eta \cdot t}$. This shows that the summation must tend to zero for late times indicating that a divergent chain will have built up.

Even with all of these approximations, the expression for $Q_N(t)$ is difficult to evaluate. Evaluating the summation is important as it allows one to relate the source non-extinction probability to a pre-initiation rate. The non-extinction probability has no knowledge of the numbers of neutrons in the system, only that some exist. It should however be no surprise that at late times the system would only consist of large neutron populations. If the expression for $Q_N(t)$ could be evaluated this could be readily seen. Another way to view this is to examine the source non-extinction probability presented in Figure 18. For late times of interest and for source strengths $\geq 10^4$ n/s, the source non-extinction probability is nearly unity which indicates that a divergent chain has almost assuredly been obtained.

Even though the source non-extinction probability and the burst probability, or pre-initiation probability, measure different physical quantities at different times, it can be readily shown that with sources present only large populations of neutrons exist at late times and the two approximate one another. Thus the importance of small numbers of neutrons is small and equating the two appears valid for the time frames of interest.

4.8 Maximum Over-pulse Examination

One of the initial primary drivers behind this work was to determine if it was possible to calculate the maximum over-pulse that can be achieved on a SPR type of machine. Per the SPR Documented Safety Analysis (DSA), the maximum over-pulse assumed for SPR is \$0.40 above prompt (Ford 2005). A pulse in this range equates to ~132 MJ of energy being deposited locally in the fuel. For such energy depositions, some 86% of the core becomes molten with < 1% being vaporized. In addition, experiments located in the central cavity may also be subject to the same fate. Investigating the maximum over-pulse can be performed with the theory developed in this work as well as the results presented previously. To begin the analysis, multiple dynamic reactivity non-extinction probability runs were performed for different pulse sizes with a fixed Δk. Pulses in the upper end of the normal range were chosen as well as those that are significantly outside authorized operations. The single neutron non-extinction probabilities were calculated and then a constant external source was also included. The figure below shows the time integrated source non-extinction probabilities for a source strength of 5,000 n/s for various pulse sizes.

The maximum over-pulse can be determined by fixing the reflector insertion time, source strength, as well as the total amount of reactivity (Δk) inserted. These parameters for SPR are assumed fixed at 250 ms, 4,700 n/s, and \$1.12 respectively. Given that the maximum amount of reactivity is fixed (via the reflector worth), an over-pulse occurs if the initial system multiplication factor is set too high. During a maximum pulse of 10¢,

the initial system reactivity is -2¢. If the initial multiplication factor is set too high, the system is actually configured into a supercritical state. The source non-extinction probability plotted versus time is shown in the figure below.

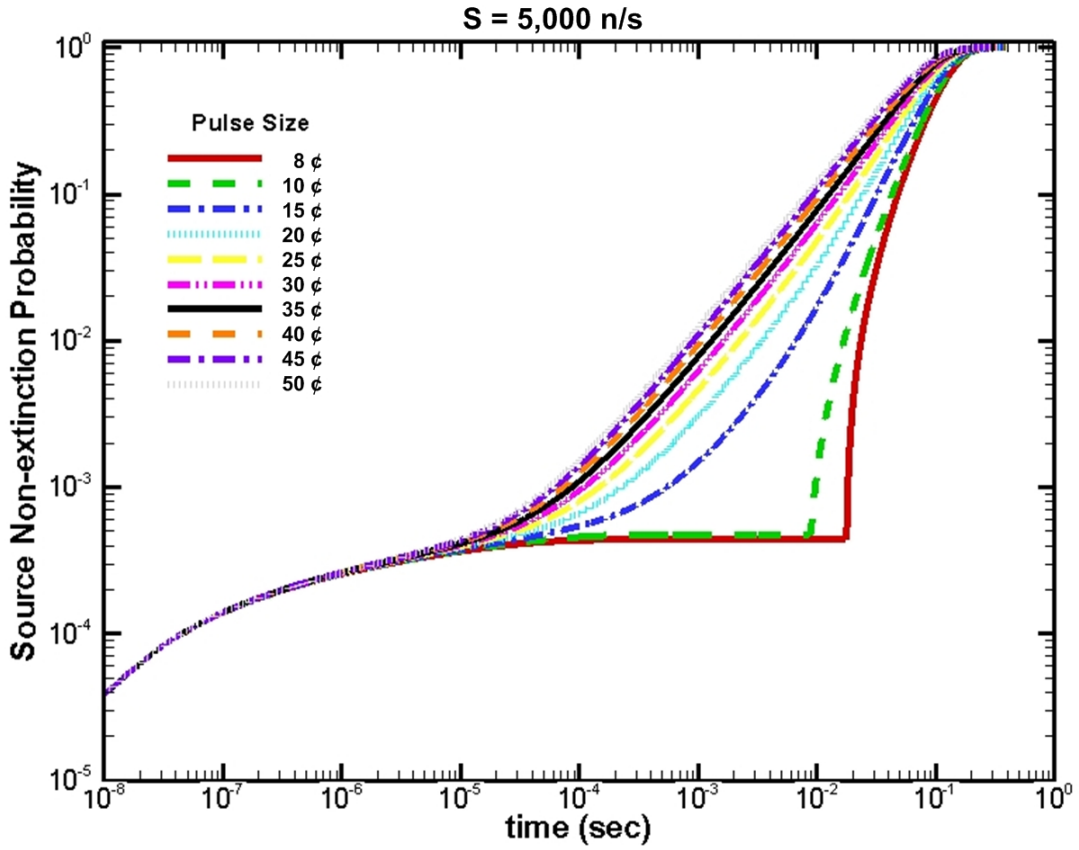

Figure 19: Source non-extinction probabilities for various pulses.

A number of different pulse values are shown in the figure above. The 8¢ and 10¢ exhibit similar behavior as seen in earlier figures where the source non-extinction probability becomes flat for a portion of the time domain. As the pulse size increases the time for the source non-extinction probability to go to one becomes shorter. There is a transition beyond 10¢ due to the fact the reflector is assumed to be worth $1.12. Thus all

cases beyond 12¢ require the system to be initially supercritical thus yielding the different functional shapes.

The time domain in the above figure was unlimited. If however the time integral on the source non-extinction probability is limited to the reflector insertion time, one can calculate the probability that the source has not become extinct at this time. The table below provides the source non-extinction at the reflector insertion time of 0.250 seconds.

Table 5: Source non-extinction probability at the reflector insertion time of 0.250 seconds.

Pulse Size (¢)	Source Non-extinction Probability
8	0.9854
10	0.9878
15	0.9919
20	0.9946
25	0.9964
30	0.9976
35	0.9984
40	0.9989
45	0.9993
50	0.9995

Significantly increasing the pulse size does not have a significant impact on the source non-extinction probability. Thus with the low source strength presented in Figure 19, there is essentially a negligible difference in the maximum over-pulse that can be performed. Thus it is difficult to support the maximum over-pulse argument given the small difference in the source non-extinction probability at 0.250 seconds.

An alternate means of comparing the results is to use a value of 99.99% for the source non-extinction probability as the divergence metric. For the cases presented above, the time at which the source non-extinction probability becomes 0.9999 was recorded. The plot above is then translated into a plot examining the source strength versus time instead of the source non-extinction probability versus time for a fixed source. This allows one to determine the source strength needed (for different pulse configurations) to either ensure/prevent a pre-initiation occurring. If this time to reach 0.9999 is shorter than 250 ms, then a pre-initiation will always occur; otherwise the machine may sit at prompt critical for a finite period of time and perform the over-pulse.

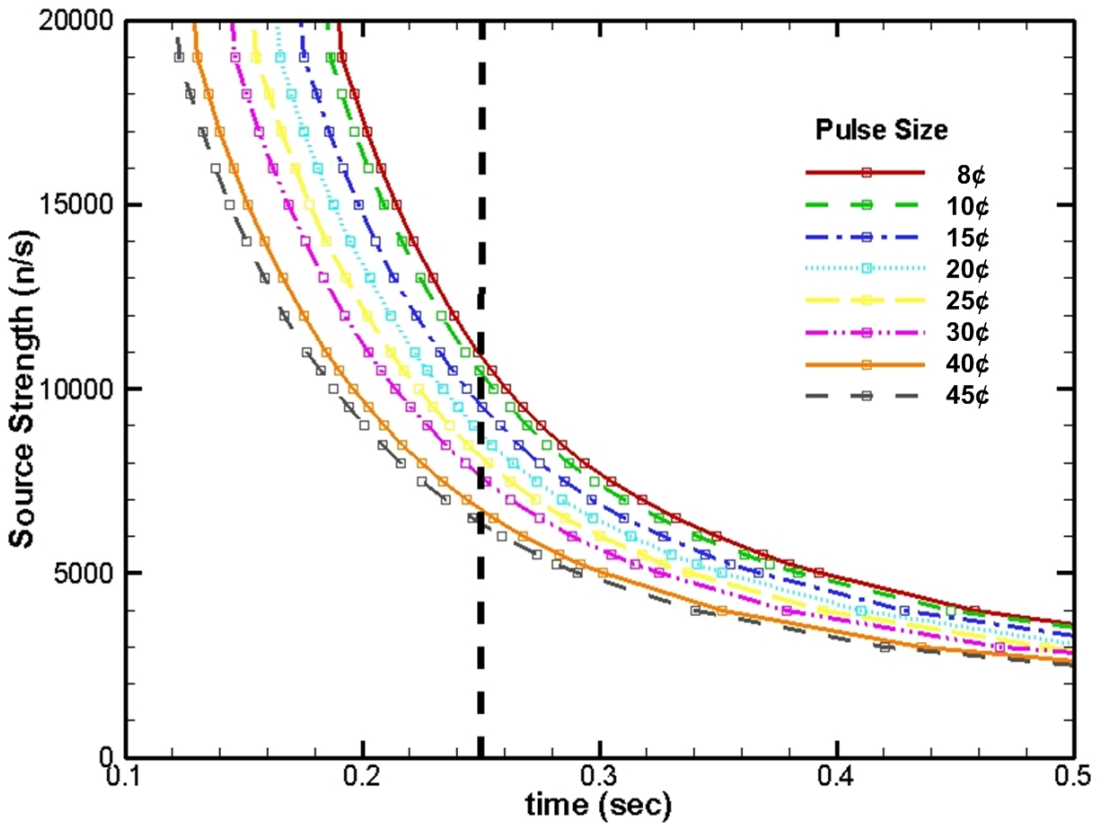

Figure 20: Maximum over-pulse applicable to SPR operations.

The figure shows the time dependent source non-extinction probability for multiple pulse conditions. Instead of fixing the source (as was done in Figure 19) the source was varied while fixing the source non-extinction probability. Picking a value for assuring that a chain has not become extinct, one is able to determine the maximum over-pulse possible. For example, the figure above illustrates that to ensure a 10¢ pulse will occur prior to 0.250 seconds, a source of ~ 10,000 n/s must be present. When establishing the maximum over-pulse the goal is to ensure that a pre-initiation actually does occur prior to fully inserting the reflector. Once divergence is assessed, the time at which this occurs is recorded. This is then related back to the linear reactivity insertion to determine what final reactivity state is feasible. An over-pulse of $1.226 (22.6¢) is sufficient to cause core melting. To preclude core melting from occurring, a source of ~ 8,000 n/s would be needed. Even if melting were not to occur, it is likely that there would mechanical damage due to the shock and thermal stresses.

Using the source strength range identified previously, the maximum pulse may be calculated. The figure shows that in order to assure that a pulse greater than 45¢ is not performed, a source of ~ 6,100 n/s is necessary. To ensure a pre-initiation occurs for lower pulse sizes the resulting background source must be increased. The range of source strengths applicable to SPR were $5.3*10^3 – 1.1*10^5$ n/s. For the low end of the source strengths, Figure 20 illustrates that overpulses greater than 45¢ are possible. The maximum source strength is off the axis scale indicating that a pre-initiation may occur for pulses smaller than 8¢.

CHAPTER 5: MONTE CARLO MODELING

5.1 Background

Monte Carlo techniques are routinely used to solve nuclear engineering problems by simulation of neutrons according to the Boltzmann transport equation. Using the same technique, an analog Monte Carlo code was written to address stochastic neutron chain buildup and the non-extinction probability. Analog refers to the faithful simulation of histories by neglecting the commonly used particle weight as a variance reduction technique. Although at first glance Monte Carlo techniques appear to be quite favorable for solving the stochastic problem of interest, in fact for weakly supercritical systems the technique is quite inefficient. The favoritism to the Monte Carlo technique is likely due to the fact that for any neutron in a medium, it will behave randomly (relative to the average behavior) with respect to how it interacts with that medium. In addition, if this neutron induces a fission event, the number of neutrons emitted from the event has a certain probability distribution to it. Thus, using pseudo-random numbers, one is able to randomly simulate different reaction events as well as sample a probability distribution for the number of neutrons from fission. It is the value of ν, not $\bar{\nu}$ that makes the non-extinction problem both interesting and non-trivial to solve. Initially the Monte Carlo code included in this work was developed as a means to assess if the non-extinction probability could indeed be solved by the Monte Carlo method. Prior to code development, it was realized that the overall efficiency of the code would be quite low, but nevertheless, information could be extracted from the code that other techniques

could not provide in a straightforward manner (namely the non-extinction probability equation).

During the historical development of the knowledge base behind stochastic transport and non-extinction problems, computational power was sufficiently low (or non-existent) such that Monte Carlo was not a viable option. Over the years it has grown in popularity due to increased computational power. It is clear that with Méchituoua's paper on using a Monte Carlo code to determine a metric for assessing divergence, Nolen's Monte Carlo work on chain lengths in subcritical systems, and the Livermore work on Mercury that there is some renewed interest in the area (Méchituoua 2000, Nolen 2000, Greenman 2007). Nolen's work was focused on subcritical systems such that there was a zero probability of observing a chain of infinite length. Despite his work also being computationally inefficient for long chain lengths, computational requirements were manageable. For the Livermore work, it is clear that allowing the code to be run on multiple processors is needed for most problems of interest (Greenman 2007).

The Monte Carlo code developed in this work begins by injecting a neutron into a prompt critical medium. Using the total cross-section for the system, a free-flight distance is calculated for the neutron. This distance is determined from $d = \frac{-\ln(1-\xi)}{\Sigma_T}$ where ξ is a random number bounded between zero and one. Given the Monte Carlo code is 0-D, the distance to collision is not of much use; however, using the neutron velocity this distance can be converted into a time to collision which is of use. With this collision time the neutron is then moved forward in time relative to the initial time. At this new time, a new

random number is sampled to determine the type of interaction that occurred at the new time. The types of interaction events used are: nothing (effectively scattering in a monoenergetic medium), capture (absorption minus fission), and finally fission (fission event with emission of 0-7 neutrons). If the nothing event is selected, the neutron still exists at the new collision time. If the neutron is captured, then it is removed at the collision time. If a fission event occurs, the parent neutron is removed at the collision time. A new random number is then called which then determines the number of neutrons emitted from the parent. These neutrons are instantaneously inserted into the medium at the collision time. As neutrons are produced at future times, these neutrons are written to an external "bank" file. In 0-D, the only information retained is the time at which this neutron would appear. Stepping the code into multiple dimensions or even energies would also require storage of additional information as well (i.e. $\vec{r}, \vec{\Omega}, E$).

Once the event for the parent has been sampled, the code then looks for more neutrons present at the current time. This will arise if the current neutron being transported also had multiple siblings from the parent fission. If neutrons are found, these are then transported independently of one another. If no neutrons are found, the code then tracks forward in time until it finds the next neutron. If no other neutrons exist, then the chain has died away. Given that the Monte Carlo code must track all future "banked" events, the code slows down as the progeny begin to build up. Thus for source histories made up of a few events, the total transport time is quick. As the source history begins to "diverge", the code slows down considerably and the computation requirements become taxing. Depending on how "large" the user lets the population build up to also has

significant ramifications on run time. On single processor machines, population sizes must typically be limited to < 100 million.

5.2 Assessing Divergence

One of the challenges associated with Monte Carlo modeling of the stochastic buildup is that the user must set an upper limit on the maximum chain size it will track. The user is forced to select a large enough value for the overall population size to ensure the chain has indeed "diverged" yet small enough to be within the limits of current computers. The words "diverged" are used loosely as it is difficult to determine if divergence has indeed occurred. Unless the user could track populations similar to that of lowest reactor power for a fast reactor ensuring divergence is difficult.

Others have discussed the problem with assessing divergence. The Livermore work suggests that the maximum chain size be variable and dependent on the overall system reactivity. They then recommend that the user select larger and larger values until there is effectively no change in the resulting probability of initiation (Greenman 2007). The problem with this approach is that it requires running the same problem multiple times to establish divergence. Méchitoua published a work for a point model where the probability of initiation was examined for different divergent chain length settings. A parametric study was performed where the upper divergence limit was increased until there was no change in the POI. An equation was developed for the divergent chain

population setting such that the chain length setting should be greater than $\frac{10}{k_{eff}-1}$ (Méchitoua 2000).

During the initial development of this work it was unclear what the setting for the divergent chain length should be. Given this, a value of one million was chosen to ensure that there was as little of biasing as possible for the determination of the POI. For all the reactivity ranges of interest, this cutoff is much greater than the recommended by Méchitoua above. For a divergence metric of one million, it would suggest that this should be sufficient for system multiplications as low as 1.00001.

5.3 0-D Results

In addition to the deterministic approach to understanding the non-extinction problem, the Monte Carlo method can also be used to simulate neutron chain buildup/decay. It can provide a means for assessing the accuracy of solutions obtained from approximate solution of the pgf equation. To illustrate the stochastic buildup of neutrons a sample plot of source histories is shown below for a static supercritical system. The plot contains 5,000 curves, one for each injected source neutron.

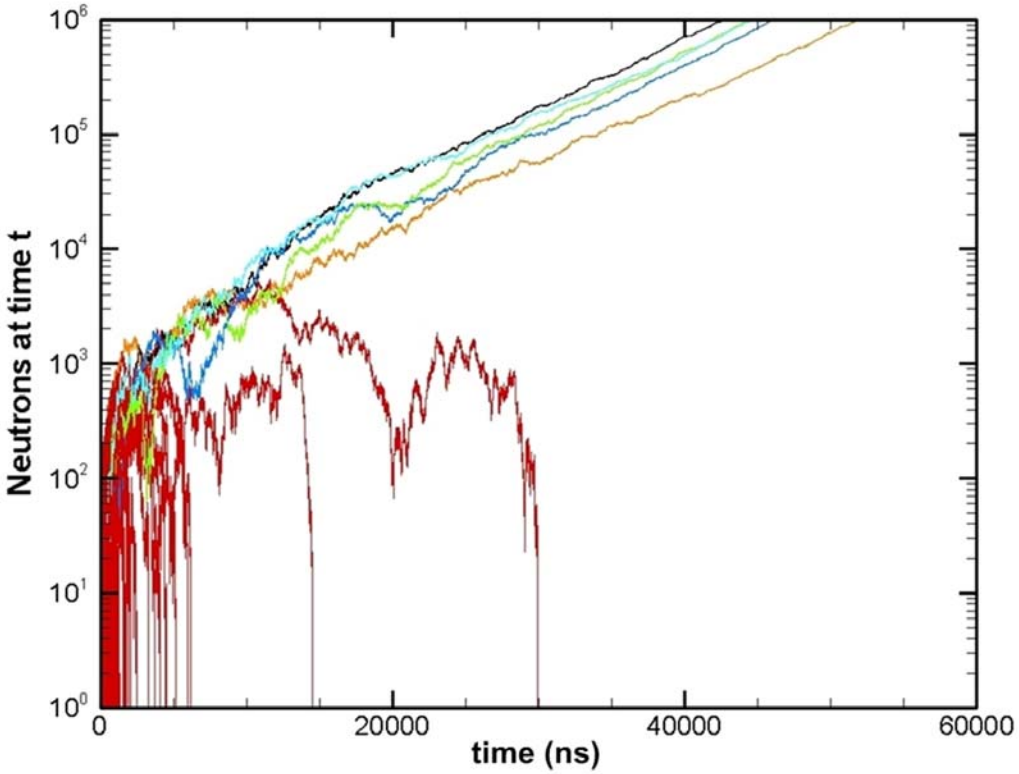

Figure 21: Monte Carlo results for the neutron population as a function of time.

For the histories presented, one can see that there are only 5 that "diverge". Again it is noted that the population was killed once it reached a size of one million. A few interesting details can be seen from the figure. For those chains that died away, most of them became extinct at very early times. Only 2 of the 5,000 were able to hang around for long times before they also eventually died away (~ 14,000 and 30,000 ns). As indicated in the figure, the population trace from these two histories oscillated back and forth. Chains that exhibit this behavior are a nuisance to the calculation. Given these chains do not quickly die away much computational time is spent with little resulting valuable information. If the SS POI is the only metric of interest, these chains are without value. Similar behavior is seen for those chains to do survive. During the early

buildup these chains also exhibit some oscillatory behavior and it is not until populations $> 10^5$ are reached that the resulting time behavior becomes smoother. Even for the population sizes presented above, the resulting time behavior for the five chains is not the same (the slope). Given this, the chains may be on their way to truly being divergent, but complete divergence cannot be assessed from the plot alone.

As shown in the above figure, there is some uncertainty as to how large is large enough for assessing divergence. Méchitoua's metric for assessing divergence occurs when the population reaches ~1,250 neutrons. As is evidenced in the figure, this value is still within the "noise" of the population but appears to be high enough to capture most of the detail.

Although time consuming, transport of a chain to one million particles is feasible on the average personal computer at the time of this writing. Simulation of histories that buildup to a decent population size, hang around for a long time, and eventually die off are a nuisance to the simulation as a large amount of computer time was spent to determine that that source history did not diverge. This is an inherently problematic issue with the Monte Carlo technique for solving this problem. In the Mercury paper, they provide an additional time cutoff for source histories that are taking too long. For the fast burst systems of interest here, the reactor proceeds rapidly into the prompt critical regime, but stays there intentionally until the pulse ensues. As such, it was not deemed adequate to include a time cutoff for long lived populations. In fact per Figure 21 the time cutoff would have to be large enough to miss the one chain that eventually dies

away (at ~ 30,000 ns). Although not illustrated above, for systems that are just slightly prompt critical, the neutron behavior is exceedingly frustrating for the Monte Carlo code. As the net ratio of production to losses approaches unity, certain source histories can in fact oscillate for very long times. A test case was run for a system at k=1.00001 and the run was finally terminated after taking more than 3 weeks of computation time on a single source neutron.

For the five cases that did show divergence, it was clear that the time at which these populations reached "divergence" was different. In fact, although not readily shown in that figure, there is a large disparity in the times at which these chains do diverge. Not only is the magnitude of the number of source histories that diverge is of importance, but also the time at which these populations reach divergence.

5.4 Divergent Chain Probability and Time to Divergence Data

For each source neutron injected into the medium, it and its progeny are followed until they either die away or they reached the divergence metric of 10^6. If the total number of divergent source neutrons are divided by the number of source neutrons injected into the medium, one obtains the divergent chain probability. This probability of obtaining a divergent chain is equivalent to the infinite medium POI. The results from the Monte Carlo simulations and infinite medium formula are plotted in the figure below.

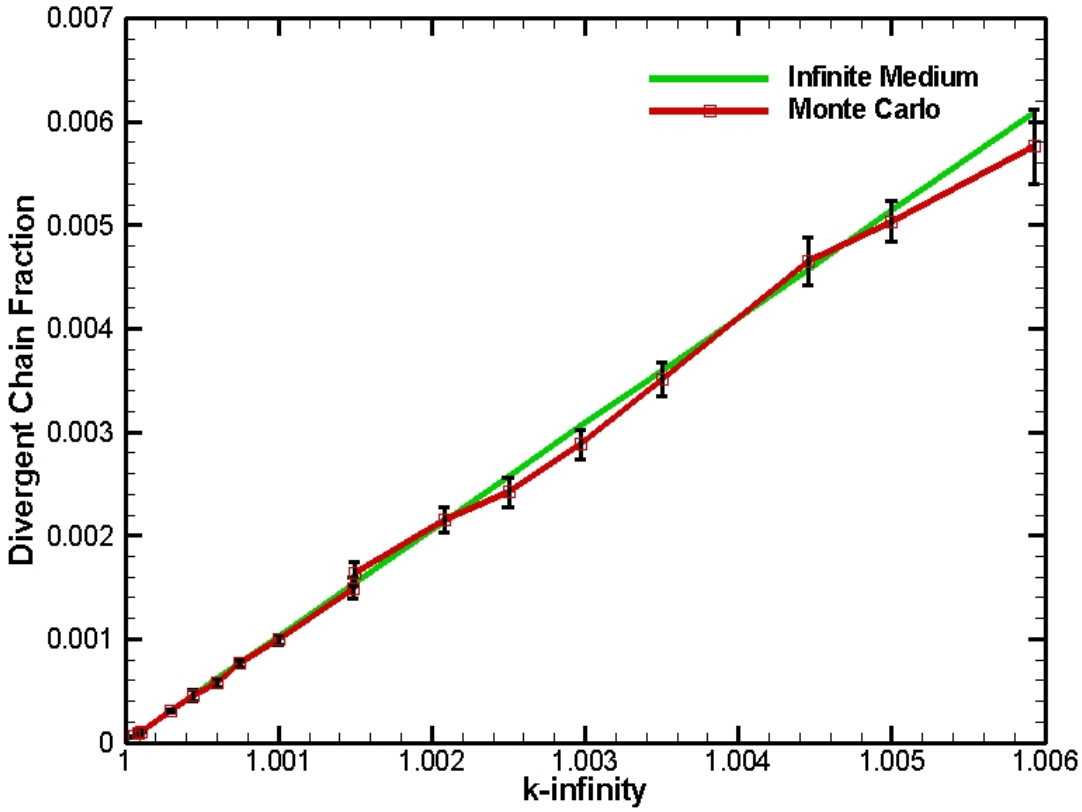

Figure 22: Divergent chain probability comparing Monte Carlo results and Bell

From the two curves shown in the figure, there is excellent agreement between the SS infinite medium solution and the Monte Carlo results. Note that the infinite medium solution relies on the quadratic truncation; the Monte Carlo work used the full fission multiplicity distribution.

As mentioned above, there is a large difference in the time it takes an individual source neutron to reach its divergence metric. Due to the variation in the time at which divergence is attained, a simple tally was performed for each of these times. These divergence times were then tallied for several different reactivity states. One would expect that the time to divergence decreases as reactivity increases. In addition, on a per

source neutron basis, the number that diverge should also increase as reactivity increases. Thus performing the calculation on strongly supercritical systems should be easiest and performing the calculation on weakly supercritical systems should be computationally challenging. These expectations can readily be observed when one examines the "time to divergence" for various reactivity states. The time to divergence is the total time it took from when the initial parent source neutron was injected to when the population hit one million. If one plots out the time at which this occurs versus an arbitrary number assigned to each source neutron that diverged, the plot below is obtained. The different color series correspond to different infinite eigenvalue states shown in the legend.

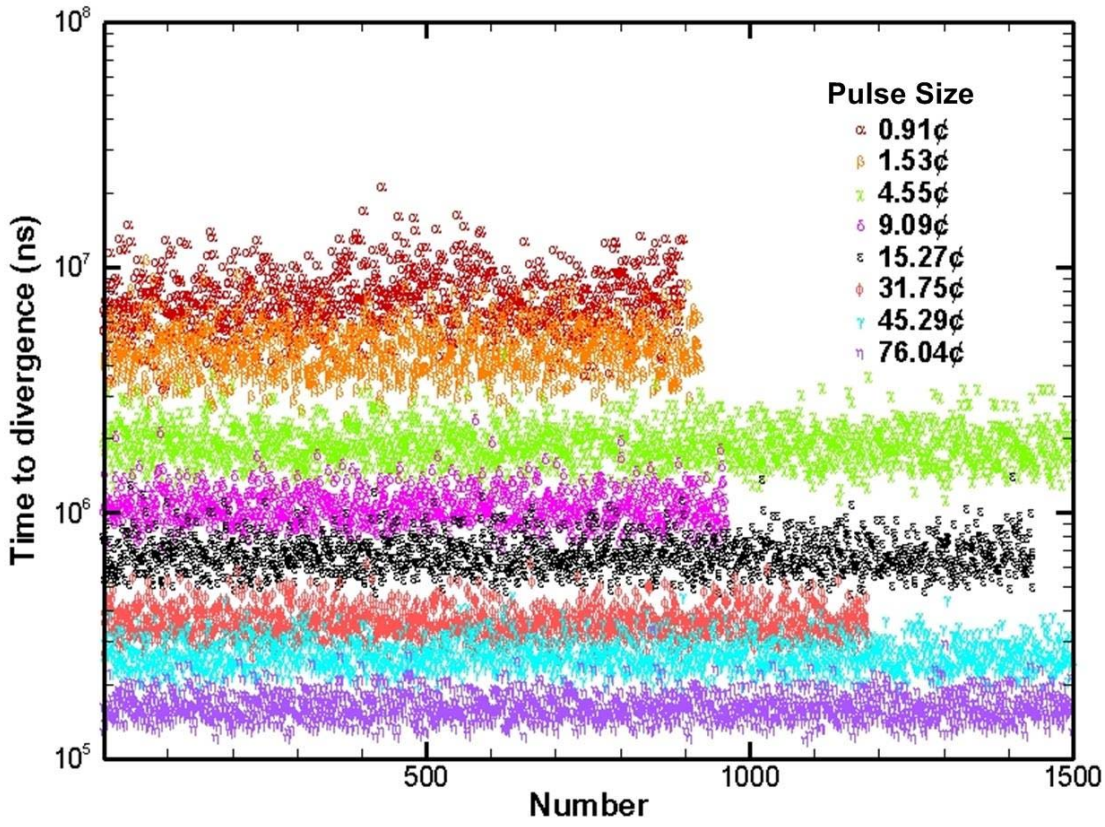

Figure 23: Time to divergence v. arbitrary particle number.

The figure above shows the time to divergence for different source particles at different static reactivity states. The figure shows a system that is weakly prompt critical (~ 1¢) to highly prompt critical systems. In Figure 23, it is readily noticed that although the times to reach divergence do vary, the distribution of times range from tightly bound to widely disperse. For high reactivity states the times to divergence are not as widely dispersed about the mean. For slightly prompt critical systems, one can see a large disparity between the mean time to divergence and the overall spread about the mean. The number of observed events is not directly proportional to the number of source neutrons injected. In other words, the average probability of initiation is different for the different reactivity states presented. This can be observed by the table below which shows the number of source histories run in order to obtain the number of divergent events. As anticipated, as the system reactivity decreases, the number of source histories run to obtain any divergent chain information greatly increases.

Table 6: Calculated divergent chain data.

reactivity above prompt (¢)	Number of divergent chains	Number of source histories	Divergent chain fraction with error*	Total run time (days)
0.916	896	15,895,000	0.000056 ± 0.000002	628.2
1.54	923	8,905,000	0.000104 ± 0.000003	146.2
4.58	1,554	5,120,000	0.000304 ± 0.000008	347.2
9.15	965	1,665,000	0.000580 ± 0.000019	172.5
11.53	1,409	1,850,000	0.000762 ± 0.000020	28.2
15.37	1,439	1,450,000	0.000992 ± 0.000026	26.7
22.85	858	575,000	0.001492 ± 0.000051	36.7
23.04	816	500,000	0.001632 ± 0.000057	10.9
31.96	1,184	550,000	0.002153 ± 0.000062	32.2
38.37	1,210	500,000	0.002420 ± 0.000069	8.6
45.59	1,743	605,000	0.002881 ± 0.000069	45.3
53.66	1,756	500,000	0.003512 ± 0.000084	8.9
68.22	1,558	335,000	0.004651 ± 0.000118	20.6
76.54	2,519	500,000	0.005038 ± 0.000100	8.6
90.73	1,008	175,000	0.005760 ± 0.000181	8.7

*Errors were calculated from: $\sigma = \sqrt{\left(\frac{1}{N-1}\right)\cdot\left(\frac{s\cdot(N-s)}{N^2}\right)}$ where N is the number of source histories and s is the number of divergent chains (Brown 2006).

Note the number of source histories that were required to be run to obtain similar numbers of divergent chains. Even modest increases in reactivity corresponded to large changes in the divergent chain fraction. The run time column shown in the table was included to provide the reader with a relative understanding of how long the simulations took. The variation in run time as the multiplication factor increases is partially due to the randomness of the problem; a secondary cause is due to machines of unequal processing power were used to generate the results. The intent behind the column is to merely highlight the very long run times required to run weakly prompt critical systems.

5.4.1 Comparison to Deterministic Results

To compare the Monte Carlo results to the deterministic results, snapshots were taken in time of the neutron distributions. For the different fixed times selected, the total numbers of neutrons found at that time are tabulated. These numbers are then divided by the total number of initial source neutrons to obtain the probability of finding any number of neutrons at that time. This is synonymous to the non-extinction probability. To illustrate that the results between the Monte Carlo method and the deterministic formulation yield similar results, a case is presented for the non-extinction probability as calculated by both methods.

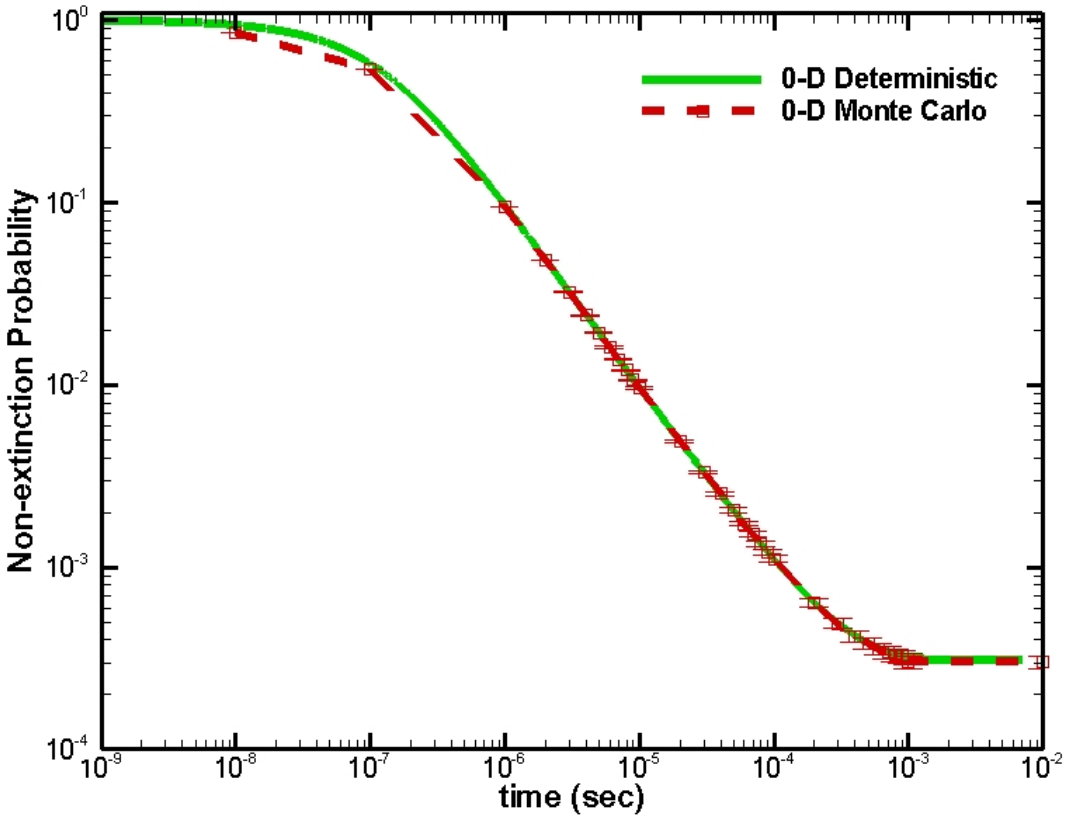

Figure 24: Integral Monte Carlo results versus S_N results for k_∞ = 1.0005.

The figure plots the non-extinction probability using both methods and illustrates excellent agreement between the two methods. The last time bin in the Monte Carlo results was taken to be at 10^{-3} seconds. An additional data point was arbitrarily added at 10^{-2} seconds which corresponds to the divergent chain probability discussed above. This plot shows that the non-extinction probability generated by either technique yields similar results.

There was some initial interest in trying to run the Monte Carlo code with a ramp insertion of reactivity to mimic the behavior of SPR. It is not difficult to see why this is computationally a bad idea on a serial machine. For the non-extinction probabilities seen above, they are all above 10^{-4}. For the ramp insertion cases presented back in Figure 17, non-extinction probabilities of 10^{-9} are seen. For even slower insertion times applicable to SPR (250 ms v. 100ms), the resulting probability would be even lower. Thus in order to resolve the time dependence one would have to run much more than a billion particles to avoid excessive error. As such, all efforts to model dynamic reactivity cases were dropped.

5.4.2 Determination of Divergent Chains

Some discussion was previously provided on the divergence metric used to limit the maximum chain buildup. What was not included was some discussion of the divergence metric on the time dependent results. Figure 21 provided some examples of chains that might be seen in a prompt critical medium. In that figure, the point at which divergence may be assessed could have been as low as 10^4 instead of the 10^6 used with no difference of the number that diverged and those that became extinct. It is clear that if the divergence metric is lowered, the times at which divergent chains are assumed to develop is shorter. If decreasing the divergence metric to some lower value is valid, the same distribution of times to reach divergence would not hold due to the random fluctuations still seen. Reexamining Figure 21, suppose that the divergent chain metric was lowered to 10^3. It would appear that there would be a total of seven divergent chains; the five applicable to the higher 10^6 divergence metric as well as two others. By adding two more divergent chains than normally would have developed, the divergent chain percentage would be overestimated. Given that the overall percentage is sufficiently small this may be an acceptable error; what may not be acceptable is the time at which divergence occurs. The two chains that are included in the divergent chain percentage illustrate some interesting behavior. Both of these chains exceed the divergence metric, then decrease below, then increase above it again, and then would eventually become extinct. With this oscillatory behavior the time to divergence behavior will be different for sufficiently low divergence metrics; despite that the error in the divergent chain percentage may be acceptable.

It is not challenging to illustrate this behavior numerically. Using a single fixed reactivity state, the Monte Carlo results were re-run for different divergence metrics. Once the runs were complete, the probability distributions developed were summed over all N at different times, exactly the same as that shown in Figure 24. Upon doing so, if there is any difference in the time dependent non-extinction probability by lowering the divergence metric, the behavior described above should be apparent. The figure below illustrates multiple different runs performed to support the argument.

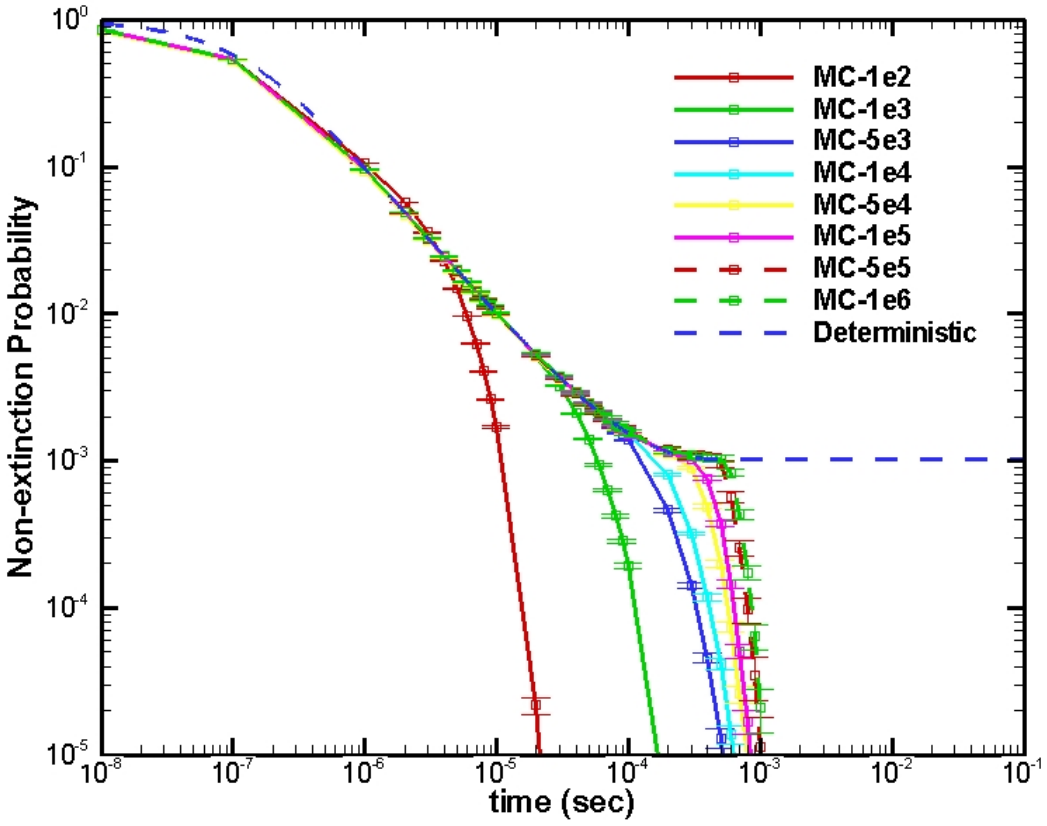

Figure 25: Integral Monte Carlo results for $k_\infty = 1.001$ for different divergence metrics.

Multiple divergence metrics were chosen and the resulting integral number distributions plotted. The results show that for large divergence metrics there is little to no change in the results as compared to the non-extinction probabilities. For much smaller metrics, there is a significant difference between the time dependent results. Lowering the divergence metric results in an overestimation of the number of divergent chains for late times. Given the purpose behind this work is to compare to a reactor system, the time dependent behavior is of utmost importance. To truly assess divergence while preserving the time dependent behavior, one should set the divergence metric to be large enough to reach the asymptotic SS POI. It is also worthwhile to illustrate the difference in the SS divergent chain probability. The table below records the data needed for comparison.

Table 7: Divergent chain probability for different divergence metrics.

Metric	Source Histories	Divergent Chains	Divergent Chain Fraction	Run Time (sec)	Source Histories / Run Time
$1*10^6$	16,300,000	16,527	0.0010139 ± 0.000007	21,874,212.8	0.75
$5*10^5$	17,750,000	17,961	0.0010118 ± 0.000007	15,984,167.8	1.11
$1*10^5$	16,250,000	16,405	0.0010052 ± 0.000009	4,255,826.7	4.27
$5*10^4$	18,350,000	18,798	0.0010244 ± 0.000007	4,349,700.9	4.22
$1*10^4$	29,750,000	29,998	0.0010083 ± 0.000006	1,247,502.8	23.85
$5*10^3$	32,000,000	32,668	0.0010209 ± 0.000006	945,277.9	33.85
$1*10^3$	30,000,000	47,457	0.001582 ± 0.000007	149,195.2	201.08
$1*10^2$	22,450,000	581,839	0.025917 ± 0.000034	18,704.0	1,200.28

Using similar numbers of source histories, the total number of divergent chains increases with a decreasing divergence metric. The divergent chain percentage is overestimated for smaller and smaller divergence metrics. For the multiplication factor used to generate the results; $k_\infty = 1.001$, Méchitoua's metric for assessing divergence would be 10^4. At this value the divergent chain fraction is similar to that of the highest metric chosen (however,

the time dependent behavior is sufficiently different that one should be careful). The total run time divided by the number of source histories is also presented in the table. This column provides a metric for the average time spent per source history. The lowest divergence metric was the fastest to transport its particles while the highest metric took the longest. This data was included not to prove this trivial point; rather, to provide the reader with an understanding for the length of time needed to transport the source histories. In other words, even though large divergence metrics approximate the deterministic solution quite well, the run time for these metrics becomes computationally burdensome.

CHAPTER 6: 1-D NUMERICAL MODELING

The deterministic non-extinction probability equation was derived and presented previously for an infinite system. Others have extended the equation to its general form for which the non-extinction probability is then dependent on the injection space, angle, energy, and time. These additional variables then describe the probability that a neutron chain has not become extinct given that the source neutron was injected at some position $\vec{r}$, traveling with some angle $\vec{\Omega}$, at a given energy E, and a time relative to the terminal condition of $(t_f - t)$. As was illustrated in previous chapters, point models are sufficient to provide the time dependent behavior; yet they lack any spatial profile that may develop.

Prior to presenting the general equation, let $p(\vec{r}, \vec{\Omega}, E, t)$ be the probability that the neutron population including all progeny do not become extinct at the final time t_f given a single neutron injection at position $\vec{r}$, with direction $\vec{\Omega}$, with energy E at time t.

The general adjoint non-extinction probability equation is then:

$$
\begin{aligned}
&-\frac{1}{v}\cdot\frac{\partial p}{\partial t}-\Omega\bullet\nabla p\left(\vec{r},\vec{\Omega},E,t\right)+\Sigma_T\left(\vec{r},E\right)\cdot p\left(\vec{r},\vec{\Omega},E,t\right)= \\
&\int^{E}\int^{\Omega} dE'\cdot d\Omega'\cdot p\left(\vec{r},\vec{\Omega}',E',t\right)\cdot\Sigma_S\left(\vec{r},\vec{\Omega}\rightarrow\vec{\Omega}',E\rightarrow E',t\right)+ \\
&\bar{\nu}\cdot\Sigma_F\left(\vec{r},E\right)\cdot\int^{E}\int^{\Omega} dE'\cdot d\Omega'\cdot p\left(\vec{r},\vec{\Omega}',E',t\right)\cdot\frac{\chi(E')}{4\pi}- \\
&\Sigma_F\left(\vec{r},E\right)\cdot\sum_{j=2}^{J}\frac{(-1)^j\chi_j\left(\vec{r}\right)}{j!}\cdot\left[\int^{E}\left(\int^{\Omega} dE'\cdot d\Omega'\cdot p\left(\vec{r},\vec{\Omega}',E',t\right)\right)\cdot\frac{\chi(E')}{4\pi}\right]^j
\end{aligned}
\tag{65}
$$

with a boundary condition of:

$$
p\left(\vec{r}_B,\vec{\Omega},E,t\right)=0 \text{ for all } \Omega\bullet n\geq 0 \tag{66}
$$

and terminal condition:

$$
p\left(\vec{r},\vec{\Omega},E,t_f\right)=1 \tag{67}
$$

The boundary condition relates the non-extinction probability for all neutrons injected on the boundary with outward directions to zero as they cannot lead to divergent chains since they initially leak out of the system. With regards to the terminal condition, the non-extinction probability for any neutron injected anywhere in the system at the terminal time must be unity as the initial injected neutron is still present.

The notation in the general equation is similar to that presented in the 0-D section (except for the spatial and angular terms) or the general transport equation except for the χ terms. The $\chi(E')$ term in the linear and non-linear fission terms represent the energy

dependent emission probability from fission. The $\chi_j\left(\vec{r}\right)$ term in the non-linear fission term comes from the fission multiplicity data presented in Table 3.

Solutions to the general equation have been found by others for limited systems; in particular, steady state systems. The time dependence of the equation has not been well documented in the past, in particular any emphasis on dynamic reactivities or numerical performance. To understand the importance of the time dependent solution as well as dynamic reactivities, the general adjoint equation was simplified. The spatial domain was limited to that of a 1-dimensional (1-D) slab. Monoenergetic neutrons are also assumed to remove any energy dependence in the model. Such assumptions are not bad approximations to a FBR type of system, in particular to SPR as the geometry is annular and the system relies on fast neutrons only for which there is negligible energy transfer in the system.

For the 1-D slab geometry of thickness L with monoenergetic neutrons, the non-extinction probability equation becomes:

$$-\frac{1}{v}\cdot\frac{\partial p(x,\mu,t)}{\partial t}-\mu\cdot\frac{\partial p(x,\mu,t)}{\partial x}+\Sigma_T\cdot p(x,\mu,t)=\frac{1}{2}\cdot\left(\Sigma_S+\bar{\nu}\cdot\Sigma_F\right)\cdot\int_{-1}^{1}p(x,\mu',t)\cdot d\mu'- \Sigma_F\cdot\sum_{i=2}^{7}(-1)^i\cdot\frac{\chi_i}{2^i\cdot i!}\cdot\left(\int_{-1}^{1}p(x,\mu',t)\cdot d\mu'\right)^i \tag{68}$$

With corresponding boundary conditions of:

$$p(0,\mu,t) = 0 \text{ for all } \mu < 0 \tag{69}$$

$$p(L,\mu,t) = 0 \text{ for all } \mu > 0 \tag{70}$$

and terminal condition:

$$p(x,\mu,t_f) = 1.0 \tag{71}$$

All neutrons injected at the boundaries with outgoing directions relative to the edge must be zero as such neutrons leak from the model. The terminal condition remains as before.

Solution to the standard adjoint equation, or the standard transport equation, is well documented in the open literature. Iteration techniques in such references are for solving a linear problem. The focus of this work was to focus primarily on the non-linearity of the equation. The iteration routines outlined below begin with the terminal condition where the non-extinction probability is unity everywhere. As one advances in time, forward sweeps (across the slab with forward angles) and backward sweeps (across the slab with negative angles) iterations are performed to allow the non-extinction probability to relax to the appropriate value at time. Such forward and backward sweeps are performed over all angles and cells in the slab at each timestep.

To solve the 1-D slab equation, multiple iteration routines were investigated. These include a standard fixed point iteration routine, a lagged fission fixed point routine, and a linearized lagged fission fixed point routine. Inclusion of synthetic acceleration was also

incorporated into the linearized routine as well. Each of the routines used in this work is addressed independently below. Once the routines are introduced, results generated using the routines are provided for comparison.

6.1 Fixed Point Iteration Routine

A fixed point iteration routine was the first iteration scheme used to solve the time dependent non-extinction probability equation. The iteration routine takes advantage of a time lagged source which is then the "source" for the next iteration. The iteration scheme is popular in many codes for solving the linear transport equation and was deemed a good starting point. Pending any numerical issues, it was also considered a viable candidate as existing transport codes which use this type of routine could be easily modified to solve stochastic problems, in addition to the deterministic ones they currently solve. Thus production codes could be simply modified and could now solve an entire new class of problems with minimal code modifications. The details of the iteration routine are outlined below.

It is noted that if the cross-section data is time independent then the non-extinction probability is time translation invariant and only depends on the time difference $\left(t_f - t\right)$. This translates the equation into a pseudo forward equation which is often more convenient for visualization. For slab geometry where symmetry is maintained, setting:

$$\mu = -\mu \tag{72}$$

Eq. 68 then reduces to:

$$\begin{aligned} &\frac{1}{v}\cdot\frac{\partial p}{\partial t} + \mu\cdot\frac{\partial p}{\partial x} + \Sigma_T\cdot p(x,\mu,t) = \left(\frac{\Sigma_S + \nu\cdot\Sigma_F}{2}\right)\cdot\int_{-1}^{1} p(x,\mu',t)\cdot d\mu' - \\ &\Sigma_F\cdot\sum_{i=2}^{7}(-1)^i\cdot\frac{\chi_i}{2^i\cdot i!}\cdot\left(\int_{-1}^{1} p(x,\mu',t)\cdot d\mu'\right)^i \end{aligned} \tag{73}$$

With reversed boundary conditions:

$$p(0,\mu,t) = 0\,,\ \mu > 0 \tag{74}$$

$$p(L,\mu,t) = 0\,,\ \mu < 0 \tag{75}$$

The terminal condition is then shifted to an "initial condition"

$$p(x,\mu,0) = 1 \tag{76}$$

From the angular dependent non-extinction probability, a properly normalized scalar probability is defined as:

$$p_0(x,t) = \cdot\int_{-1}^{1} p(x,\mu',t)\cdot d\mu' \tag{77}$$

Inserting this into the equation:

$$\frac{1}{v}\cdot\frac{\partial p}{\partial t}+\mu\cdot\frac{\partial p}{\partial x}+\Sigma_T\cdot p(x,\mu,t)=\left(\frac{\Sigma_S+\nu\cdot\Sigma_F}{2}\right)\cdot p_0(x,t)-\Sigma_F\cdot\sum_{i=2}^{7}(-1)^i\cdot\frac{\chi_i}{2^i\cdot i!}\cdot p_0^i(x,t) \tag{78}$$

For simplification of notation, also define the fission operator as the sum of the linear and non-linear fission components:

$$N(p_0)=\frac{\bar{\nu}\cdot\Sigma_F}{2}\cdot p_0(x,t)-\Sigma_F\cdot\sum_{i=2}^{7}(-1)^i\cdot\frac{\chi_i}{2^i\cdot i!}\cdot p_0^i(x,t) \tag{79}$$

The equation then simplifies to:

$$\frac{1}{v}\cdot\frac{\partial p}{\partial t}+\mu\cdot\frac{\partial p}{\partial x}+\Sigma_T\cdot p(x,\mu,t)=\frac{\Sigma_S}{2}\cdot p_0(x,t)-N(p_0) \tag{80}$$

The discretization utilizes a fully implicit time discretization where s denotes the time index:

$$p^{(s)}(x,\mu)=p(x,\mu,t_s)\text{ for }s=0,1,2,\ldots$$

$$\Delta t=t_{s+1}-t_s$$

Then approximating the time derivative as:

$$\frac{\partial p}{\partial t}\approx\frac{p^{(s+1)}-p^{(s)}}{v\cdot\Delta t} \tag{81}$$

Inserting this into Eq. 80 and combining terms:

$$\left(\Sigma_T+\frac{1}{v\cdot\Delta t}\right)\cdot p^{(s+1)}+\mu\cdot\frac{\partial p^{(s+1)}}{\partial x}=\frac{\Sigma_S}{2}\cdot p_0{}^{(s+1)}-N\left(p_0{}^{(s+1)}\right)+\frac{p^{(s)}}{v\cdot\Delta t} \tag{82}$$

Eq. 82 is solved at each $s+1$ timestep with knowledge of the non-extinction probability from the s timestep where $\frac{p^{(s)}}{v \cdot \Delta t}$ is fixed over the $s+1$ timestep. For the first timestep, the initial condition is invoked. The fixed time lagged term (on the right hand side) is denoted by $Q(x,\mu)$. Iterations are used to resolve the spatial non-extinction probability within the slab over the $s+1$ timestep. The non-linear fission terms depend on the scalar probabilities and are therefore included in the scattering source and lagged in the sweeps. Over the timestep of interest the time indexes are dropped and using a new index k for the each iteration.

$$\left(\Sigma_T + \frac{1}{v \cdot \Delta t}\right) \cdot p^{(k+1)} + \mu \cdot \frac{\partial p^{(k+1)}}{\partial x} = \frac{\Sigma_S}{2} \cdot p_0{}^{(k)} - N\left(p_0{}^{(k)}\right) + Q(x,\mu) \text{ for } k = 0,1,2,\ldots \tag{83}$$

Spatial differencing is accomplished through standard diamond differencing where centered valued functions and the cell centers are approximated by the average of the corresponding neighboring nodes (cell edges). The cell average probability is defined as:

$$p_j^{(k)}(\mu) = \frac{1}{\Delta x_j} \cdot \int_{x_{j-1/2}}^{x_{j+1/2}} p^{(k)}(\mu, x) \cdot dx \tag{84}$$

Integrating Eq. 83 over the j[th] cell:

$$\mu \cdot \left(p_{j+1/2}^{(k+1)}(\mu) - p_{j-1/2}^{(k+1)}(\mu)\right) + \left(\Sigma_T + \frac{1}{\Delta t}\right) \cdot \Delta x_j \cdot p_j^{(k+1)}(\mu) = \frac{\Sigma_S}{2} \cdot \Delta x_j \cdot p_{0,j}^{(k)} - \int_{x_{j-1/2}}^{x_{j+1/2}} N\left(p_{0,j}^{(k)}\right) \cdot dx + Q_j(\mu) \tag{85}$$

where

$$Q_j(\mu) = \frac{1}{v \cdot \Delta t} \cdot \int_{x_{j-1/2}}^{x_{j+1/2}} p^{(s)}(\mu, x) \cdot dx = \frac{\Delta x}{v \cdot \Delta t} \cdot p_j^{(s)}(\mu) \tag{86}$$

The above equation has both cell and edge defined probability terms. A closure relation is therefore necessary. The close relation assumes that the average across a cell is defined as half of the summation of the cell boundary values.

$$p_j^{(k+1)}(\mu) = \frac{p_{j+1/2}^{(k+1)}(\mu) + p_{j-1/2}^{(k+1)}(\mu)}{2} \tag{87}$$

Another assumption is invoked on the non-linear terms:

$$\int_j N\left(p_{0,j}^{(k)}\right) \cdot dx = \Delta x_j \cdot N\left(p_{0,j}^{(k)}\right) \tag{88])}$$

To address the angular domain, the standard discrete ordinates, S_N approximation is used. The discrete ordinates technique holds the angular domain at fixed discrete angles. These discrete angles are taken to be Gauss-Legendre quadrature points, $\{\mu_m, m = 1,2,\ldots M\}$, such that the angular domain in slab geometry from -1 to 1 is replaced by a weighted quadrature sum such that:

$$p_{0,j}(t) \approx \sum_{m=1}^{M} w_m \cdot p_{j,m}(t) \tag{89}$$

Inserting this into the differenced Eq. 85 yields:

$$\mu_m \cdot \left(p_{m,j+1/2}^{(k+1)} - p_{m,j-1/2}^{(k+1)}\right) + \left(\Sigma_T + \frac{1}{\Delta t}\right) \cdot \Delta x_j \cdot p_{m,j}^{(k+1)} = \frac{\Sigma_S}{2} \cdot \Delta x_j \cdot p_{0,j}^{(k)} - \Delta x_j \cdot N\left(p_{0,j}^{(k)}\right) + Q_{m,j} \tag{90}$$

For neutrons traveling in the positive direction $\mu_m > 0$: $p_{m,j-1/2}^{(k)}$ is known from the left boundary condition and using the diamond closure relationship:

$$p_{m,j+1/2}^{(k+1)} = 2 \cdot p_{m,j}^{(k+1)} - p_{m,j-1/2}^{(k+1)} \tag{91}$$

Plugging this into the first term in Eq. 90, yields:

$$\mu_m \cdot \left(p_{m,j+1/2}^{(k+1)} - p_{m,j-1/2}^{(k+1)}\right) = 2 \cdot \mu_m \cdot \left(p_{m,j}^{(k+1)} - p_{m,j-1/2}^{(k+1)}\right) \tag{92}$$

For all positive angles, the forward sweep is then:

$$\left[\mu_m + \left(\Sigma_T + \frac{1}{v \cdot \Delta t}\right) \cdot \frac{\Delta x_j}{2}\right] \cdot p_{m,j}^{(k+1)} = \frac{\Sigma_S}{4} \cdot \Delta x_j \cdot p_{0,j}^{(k)} - \frac{\Delta x_j}{2} \cdot N\left(p_{0,j}^{(k)}\right) + \mu_m \cdot p_{m,j-1/2}^{(k+1)} + \frac{Q_{m,j}}{2} \tag{93}$$

and with the closure relationship:

$$p_{m,j+1/2}^{(k+1)} = 2 \cdot p_{m,j}^{(k+1)} - p_{m,j-1/2}^{(k+1)} \tag{94}$$

where $p_{m,j-1/2}^{(k)}$ is known from the left boundary condition.

For all negative angles, the backward sweep is similar with:

$$\left[\mu_m + \left(\Sigma_T + \frac{1}{\Delta t}\right)\cdot\frac{\Delta x_j}{2}\right]\cdot p_{m,j}^{(k+1)} = \frac{\Sigma_S}{4}\cdot\Delta x_j\cdot p_{0,j}^{(k)} - \frac{\Delta x_j}{2}\cdot N\left(p_{0,j}^{(k)}\right) + \mu_m\cdot p_{m,j+1/2}^{(k+1)} + \frac{Q_{m,j}}{2} \tag{95}$$

and with the closure relationship

$$p_{m,j-1/2}^{(k+1)} = 2\cdot p_{m,j}^{(k+1)} - p_{m,j+1/2}^{(k+1)} \tag{96}$$

where $p_{m,j+1/2}^{(k)}$ is known from the right boundary condition.

Once the forward and backward sweeps are performed, an error is calculated. The sweeps are performed until convergence is obtained. Convergence is assessed through the L2 norm error, or $\|L2\|$, which is calculated from:

$$\|L2\| = \sqrt{\frac{1}{N}\cdot\sum_{i=1}^{N}\Delta x\cdot\left[p_0^{k+1}(i) - p_0^{k}(i)\right]^2} \tag{97}$$

The L2 norm provides an error estimate from the square root of the squared absolute errors between successive iterations. Thus $p_0^k(i)$ are the angular integrated, spatially dependent non-extinction probabilities from to the k^{th} iteration and $p_0^{k+1}(i)$ represent the values post iteration.

Once both the iterations have converged to the specified error criteria, the process is repeated at the next timestep. It will be shown later that the spectral radius, the relative error decrease from one iteration to the next, is quite variable throughout the iteration process. In order to ensure that there are no false convergence issues, the specified error criteria for convergence is modified by the calculated spectral radius. The spectral radius is estimated from the L2 norm of three successive k iterations [Warsa 2002]:

$$\rho \approx \frac{\left\| p_0^{k+1} - p_0^k \right\|_2}{\left\| p_0^k - p_0^{k-1} \right\|_2} \tag{98}$$

The error criteria is adjusted to the calculated spectral radius through:

$$\varepsilon^* = (1-\rho)\cdot\varepsilon \tag{99}$$

This scaling is typically recommended to avoid false convergence. A thorough investigation on the error criteria was performed to ensure that a sufficiently small value was chosen to preclude false convergence. This can particularly become an issue as the non-extinction becomes small, thus the relative difference between successive iterations may be small. It was found that selecting an error criterion of 10^{-10} was sufficient.

6.2 Lagged Fission Fixed Point Routine

The lagged fission source iteration scheme is a modified version of the fixed point iteration scheme outlined above. The major difference is that the fission terms, both linear and non-linear, are pulled out of the iteration loop and are then updated in a new outer iteration. Within a given timestep, the fission terms are then resolved in the new outer iteration and then held constant over the inner iteration loop where the scattering term is resolved. The inner iterations are now different such that it includes both the linear and non-linear fission terms and the time lagged source; all of which are held constant over the inner iteration. The inner iteration now has effectively two fixed source terms, one from the fission terms calculated in the outer iteration and one from the time lagged source from the previous timestep. The motivation to pull the fission terms out of the inner iteration was driven by the numerical performance of the fixed point routine. Discussions of the performance are addressed in a subsequent chapter. The benefit of lagging the fission terms is that the inner iterations will be shown to converge quite rapidly.

Rather than repeat the entire discretization, only those equations which are modified are listed below. The new outer iteration is denoted by a l index. At the beginning of each timestep, the time lagged source is updated through Eq. 86 (see above). Then in the new outer iteration a lumped fission source term is evaluated which is a combination of both the linear and non-linear fission terms.

$$N[L]_{0,j}^{(l)} = \bar{\nu} \cdot \Sigma_F \cdot \frac{\Delta x_j}{4} \cdot p_{0,j}^{(k)} - \frac{\Delta x_j}{2} \cdot N\left(p_{0,j}^{(k)}\right) \tag{100}$$

These terms are evaluated from the converged scalar probabilities of the previous timestep (as denoted by the k index) and are then fixed over the new set of inner iterations. Once the inners have reached the convergence criteria, the outer iterations are also checked for convergence. Convergence for the outers is determined through the L2 norm of the scalar probability used to evaluate the fission terms, $p_{0,j}^{(l)}$ and the newly converged scalar probability from the inners, $p_{0,j}^{(k+1)}$.

The inner iterations are greatly simplified and for positive angles then become:

$$\left[\mu_m + \left(\Sigma_T + \frac{1}{\Delta t}\right) \cdot \frac{\Delta x_j}{2}\right] \cdot p_{m,j}^{(k+1)} = \frac{\Delta x_j \cdot \Sigma_S}{4} \cdot p_{0,j}^{(k)} + \mu_m \cdot p_{m,j-1/2}^{(k+1)} + N[L]_{0,j}^{(l)} + \frac{Q_{m,j}}{2} \tag{101}$$

Now instead of only holding the time lagged source as fixed, both it and all of the fission terms are held fixed over the inner iteration. After the inner iteration has reached the convergence criteria, another outer iteration, $(l+1)$, is utilized where all of the fission terms are updated from the converged scalar probability of the inners and then again held

fixed over all the inners. Note that the time lagged source is not updated until the next timestep where the process is repeated. Once convergence has been obtained for both the inner and outer iterations, the simulation then advances to the $s+1$ timestep.

6.3 Linearized Lagged Fission Fixed Point Routine

The final iteration routine investigated was that of a linearized lagged fixed point routine. The routine is similar to the lagged routine described above except that the fission terms (both linear and non-linear) in the equation are linearized and then evaluated about a constant value. This routine takes advantage of the same inner and outer iteration architecture. As with the lagged fission routine described above, both of the linear and non-linear terms are evaluated in the outer iteration and then held constant over the inner iteration. The only difference is that the fission terms in the outers are linearized prior to being held fixed over the inners. These terms were linearized in order to allow for acceleration and for subsequent Fourier analysis in which the theoretical spectral radius may be calculated. Calculation of the theoretical value was necessary to understand the behavior and performance of the linearized routine. Numerical results for the iteration routine, in particular how it performs against the theoretical analysis will both be presented in a subsequent chapter. The details of the iteration routine are outlined below; however, only those details which are different are provided.

Revisiting the discretized equation (formerly Eq. 90):

$$\mu_m \cdot \left(p_{m,j+1/2}^{(k+1)} - p_{m,j-1/2}^{(k+1)}\right) + \left(\Sigma_T + \frac{1}{v \cdot \Delta t}\right) \cdot \Delta x_j \cdot p_{m,j}^{(k+1)} = \frac{\Sigma_S}{2} \cdot \Delta x_j \cdot p_{0,j}^{(k)} - \Delta x_j \cdot N\left(p_{0,j}^{(l)}\right) + Q_{m,j} \tag{102}$$

The linearization begins by assuming the linear and non-linear terms can be linearized through:

$$N\left(p_{0\,j}\right) = N\left[p_{0\,j}^{(k)} + \left(p_{0\,j}^{(k+1)} - p_{0\,j}^{(k)}\right)\right] \approx N\left(p_{0\,j}^{(k)}\right) + \left[p_{0\,j}^{(k+1)} - p_{0\,j}^{(k)}\right] \cdot N'(x) \tag{103}$$

where $N'(x) = \left.\frac{\partial N}{\partial p_0}\right|_{p_{0\,j}^{(k)}}$. The k iteration index is used to highlight that these terms are evaluated with the converged solution from the inner iterations. Inserting this into the discretized non-extinction probability:

$$\mu_m \cdot \left(p_{m,j+1/2}^{(k+1)} - p_{m,j-1/2}^{(k+1)}\right) + \left(\Sigma_T + \frac{1}{v \cdot \Delta t}\right) \cdot \Delta x_j \cdot p_{m,j}^{(k+1)} = \frac{\Sigma_S}{2} \cdot \Delta x_j \cdot p_{0,j}^{(k)} + \Delta x_j \cdot \left[N\left(p_{0\,j}^{(k)}\right) + p_{0\,j}^{(k+1)} \cdot N'(x) - p_{0\,j}^{(k)} \cdot N'(x) + Q_{m,j}\right] \tag{104}$$

or

$$\left(\mu_m + \left(\Sigma_T + \frac{1}{v \cdot \Delta t}\right) \cdot \frac{\Delta x_j}{2}\right) \cdot p_{m,j}^{(k+1)} = \frac{\Sigma_S}{4} \cdot \Delta x_j \cdot p_{0,j}^{(k)} + \mu_m \cdot p_{m,j-1/2}^{(k+1)} + \frac{\Delta x_j}{2} \cdot \left[N\left(p_{0\,j}^{(k)}\right) + p_{0\,j}^{(k+1)} \cdot N'(x) - p_{0\,j}^{(k)} \cdot N'(x) + Q_{m,j}\right] \tag{105}$$

The terms $\frac{\Delta x_j}{2} \cdot \left[Q_{m,j} + N\left(p_{0_j}^{(k)}\right) - p_{0_j}^{(k)} \cdot N'(x) \right]$ are updated for each timestep and then held fixed over all the outers/inners at that timestep. The terms $\frac{\Delta x_j}{2} \cdot \left[p_{0_j}^{(k+1)} \cdot N'(x) \right]$ are updated in each outer with the converged scalar inner k+1 iterate.

The discretized inner iterations are identical to that of the lagged routine shown above and are not repeated.

6.3.1 Diffusion Synthetic Acceleration of Inners

The fixed point iteration routine is known to breakdown for systems that have optically thick cells where the meshing is typically greater than a mean free path and in which the scattering ratio, c_S, (ratio of the scattering to the total cross-section) is near one. The monoenergetic code described here is by definition of one energy and it was shown that for a fast fission energy range the scattering ratio is ~ 0.83 (Figure 4). Thus convergence issues known with this type of routine should not be an issue for the problems of interest. The standard diffusion synthetic acceleration (DSA) scheme was used to speedup the inner iteration performance. Acceleration of the inner scattering iterations can be achieved by applying DSA to the inner iteration, and the subsequent performance of the inners should be similar to that seen when solving the standard transport equation. After the forward and backward sweeps are performed for all angles, a DSA update is

performed. The details behind using DSA are well documented and are not present here; rather, performance results are provided to give an indication of the speedup.

For the cross-sections presented in Figure 4, the scattering ratio, $c_S = \Sigma_S / \Sigma_T$ is 0.833. Although this is low enough to not be much of a concern, DSA on the inners was included for completeness. The table below highlights the number of inner iterations required for convergence by numerically adjusting the scattering ratio. The table is included to highlight that the DSA update on the inners performs according to expectation.

Table 8: Performance of the inner iterations with and without acceleration.

Scattering ratio c_S	Simulation timestep 1 ns		Simulation timestep 10^9 ns	
	Unaccelerated	Accelerated	Unaccelerated	Accelerated
0.1	4	4	6	5
0.2	5	4	8	5
0.3	5	4	10	6
0.4	6	4	11	6
0.5	6	5	14	7
0.6	7	5	17	8
0.7	8	5	22	9
0.8	10	6	31	10
0.833	11	6	34	10
0.9	14	6	71	10
0.95	23	7	171	10
0.99	83	9	1103	10
0.995	152	9	2251	10
0.999	647	10	10549	10
0.9995	1208	10	19754	10
0.9999	5072	10	83826	10

As the scattering ratio approaches unity, the number of inner iterations greatly increases for the unaccelerated case. Applying the DSA scheme allows the number of iterations to be reduced to a manageable number. Although the reduction in inner iterations is small for the scattering ratio applicable to fast burst reactors, inclusion of DSA on the inners proves to be an acceptable means of reducing the overall iteration count.

6.4 1-D Verification Testing

An important feature of any code is a benchmark for comparison of results. Good agreement was already shown between the analytical and numerical analysis presented in 0-D. Unfortunately there is no general time dependent analytical solution in 1-D to compare the numerical results against. Given this, there are other features of the code that can be checked against expected results to determine whether at least certain portions of the numerical solution are behaving according to expectations.

6.4.1 Critical Slab Thickness

In order to verify that the code was performing as expected without the non linear terms, different critical slab thicknesses were computed and then compared to known analytic solutions (Bell 1970). Using the methodology outlined in Duderstadt, a k-eigenvalue calculation was performed (Duderstadt 1976). Effectively, the linear fission term is divided by a scaling factor k and all non-linear terms are ignored. The value of k_{eff} (as well as the scalar probability) is iterated upon until sufficient convergence has been obtained. For the k-eigenvalue update, the following approximation is made.

$$k^{(k+1)} \cong \frac{\int^{x} dx \cdot p_0^{(k+1)}(x)}{\frac{1}{k^{(k)}} \cdot \int^{x} dx \cdot p_0^{(k)}(x)} \tag{106}$$

where $p_0^{(k)}(x)$ is the spatially dependent scalar probability for the x^{th} cell. The standard vacuum boundary conditions were invoked on the slab.

Upon convergence of both the k-eigenvalue and the scalar probability, the following result was obtained for the eigenvalue versus slab thickness.

Figure 26: Numerical eigenvalues for critical slab thicknesses.

c	Slab Thickness (cm)	k_{eff}
1.02	34.80218	1.0000067
1.05	20.86878	0.9999942
1.10	14.00048	1.0000163
1.20	9.31757	0.9999212
1.40	13.67975	0.9999649
1.60	10.86691	0.9999542

The numerical results agree well with the expected slab thicknesses. To ensure the results were not being biased by the number of slab cells or the angular quadrature order, 300 spatial cells were used along with 64 quadrature ordinates (S_{64}).

Inclusion of the k-eigenvalue search was also necessary in order to relate a slab thickness to its multiplication factor. Otherwise one would not know what the calculated non-extinction probability corresponded to. Throughout the 1-D results, a k-eigenvalue search is initially performed. This additional calculation is fast and adds a slight increase in overall computation time.

6.4.2 Infinite Medium Eigenvalue Comparisons

A means to check the steady state POI is to invoke reflective boundary conditions on the slab boundary. Upon doing so, the finite slab will become an infinite media. As such the solution anywhere within the slab should equate exactly to the 0-D infinite media result at long times. The boundary condition on the slab edges is modified by setting the outgoing current to be the incoming current at the same angle. The time dependent result was computed and is shown below. For the plot below the complete fission multiplicity was used and the infinite eigenvalue was $k_\infty = 2.1781$.

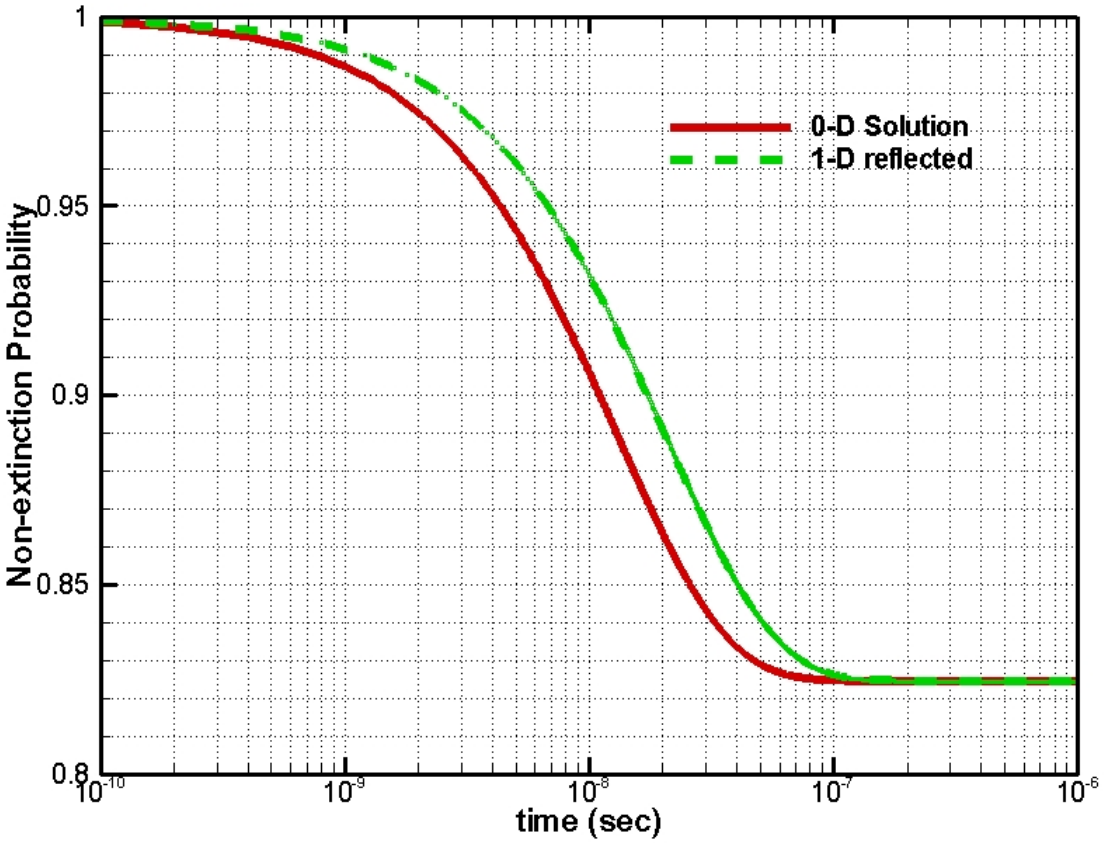

Figure 27: Time dependent 0-D solution v. 1-D reflected solution.

Both the 0-D and reflected 1-D solutions begin at the same initial probability of 1.0. The 0-D results were generated using the Newton iteration routine and the 1-D results were generated using the lagged fission source routine. Given that the 0-D solution is by definition dimensionless, the solution begins to decay away quicker than the 1-D solution. This is primarily due to the fact that neutrons which leak out of the 1-D slab solution are reflected back into the slab at the next interval. Thus neutrons are transported throughout the slab and conservation is maintained by preventing any neutrons from exiting the core. Due to this the 1-D solution takes longer to reach the SS POI than the 0-D solution. However in the limit as time goes to infinity, both solutions

converge to the same SS POI value indicating that the 1-D routine yields the appropriate SS POI.

6.4.3 Importance of the Quadrature Order

The quadrature order approximation for the angular domain has great importance on the overall solution. To highlight this, the following figure presents the results of the time dependent solution by varying the quadrature order. The intent of this plot is to highlight the relatively high S_N order needed. For the time dependent slab results, the slab midpoint is plotted as a function of the S_N order selected. The slab thickness was 9.5523 cm which corresponded to a system multiplication factor of 1.01.

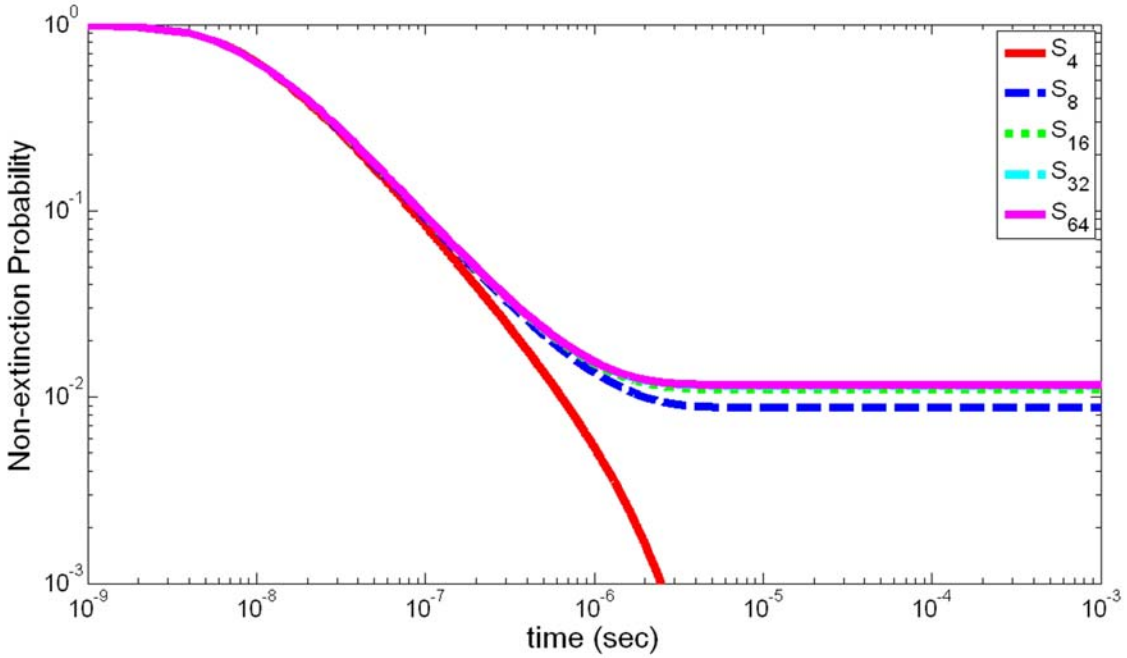

Figure 28: Importance of quadrature order on the time dependent slab midpoint values.

It is readily seen that the quadrature order has a large impact on the resulting time dependent behavior. Perhaps this is best seen by the S_4 case. The non-extinction probability goes to zero for this curve as the resulting eigenvalue calculated for the system was less than 1.0. It can be seen that a quadrature order greater than ~ 32 is sufficient to capture the full time dependent behavior. The impact of the quadrature order can also be seen on the calculated eigenvalues.

Table 9: Importance of quadrature order on the calculated eigenvalue.

S_N Order	Calculated k_{eff}
512	1.01003297
256	1.01003144
128	1.01002528
64	1.01000044
32	1.00989916
16	1.00947547
8	1.00755365
4	0.99410899
2	0.89942096

Even though decent time dependent numerical results indicate that a quadrature order of ~ 32 is sufficient to capture the time dependent results, larger values may be needed for adequate resolution of the angular domain. Unless otherwise noted, all results used in this work use the S_{64} approximation.

CHAPTER 7: 1-D NUMERICAL RESULTS

Using the numerical routines presented, analyses are performed to understand the time dependent non-extinction probability. Unless otherwise noted, all of the results below were generated with the linearized lagged routine. Although this will be examined in detail in the subsequent chapter, there is little difference in the time dependent solutions between the different iteration routines. Rather, differences are seen with the iteration performance. The 1-D slab with static reactivity was the first system investigated. Initially the simulation timestep was examined to determine if the same timestep behavior seen in the 0-D system was also seen in the 1-D case. Next the slab thickness was varied to examine the importance of the non-extinction probability on the slab width. The spatial and angular components of the non-extinction probability were examined. An examination of the spatial solution obtained from the linear eigenvalue value solution is provided relative to the spatial solution for the non-linear problem. For the static plots, the full fission multiplicity was utilized and a slab thickness of $L = 9.421$ cm $\left(k_{eff} = 1.001\right)$. Results are also extended to examination of a dynamic system with an external source.

7.1 Timestep Analysis

The non-extinction probability was solved for a fixed reactivity state. The solution as a function of time was tracked at both the slab midpoint and edge value. The simulation timestep was then varied to determine its importance on the time dependent behavior.

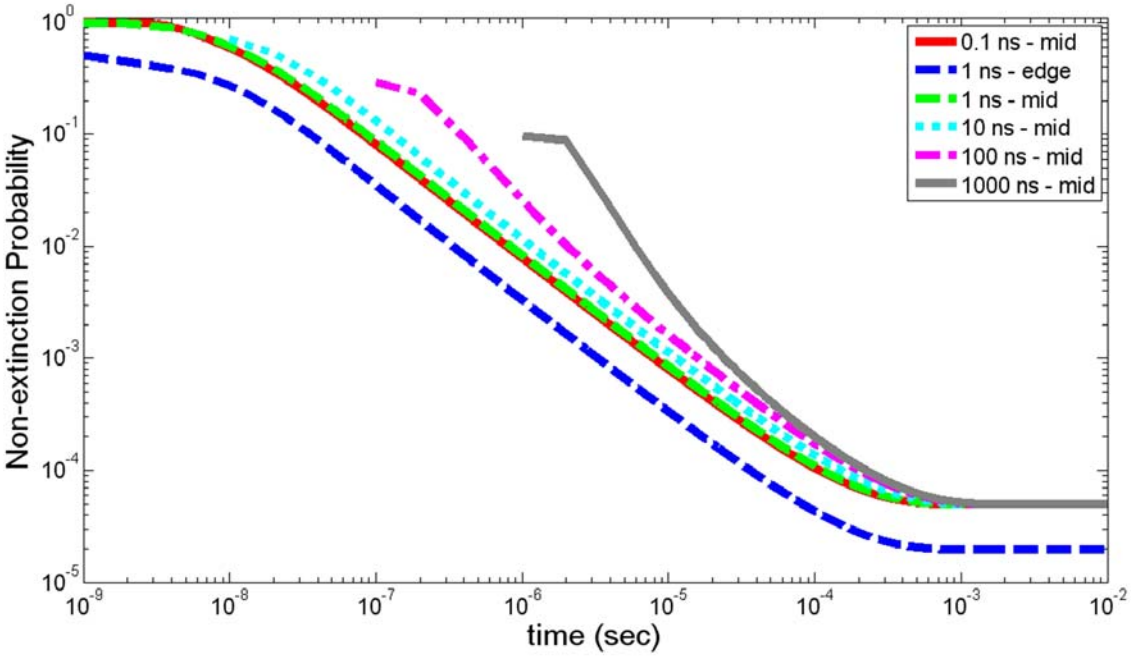

Figure 29: Importance of timestep on time and spatially dependent solution.

The shapes of the curves are quite similar to those presented in Figure 13 for the 0-D analysis. The major difference between the two figures is the magnitude of the non-extinction probability for which the 1-D results are lower due to the spatial mode that develops in the slab geometry. The slab midpoint has the highest probability and the slab edges will have the lowest. In the figure, both the slab midpoint and edge values are shown for a 1ns timestep. Although the shapes of the curves are identical, the resulting magnitude of the slab edges is consistently lower. A spatial mode is shown to develop

for all of the results presented in the 1-D section; unless otherwise noted the non-extinction probabilities presented are always for the slab midpoint.

The timestep behavior seen in 1-D mimics that seen in 0-D. Large timesteps may be taken in order to reach the SS POI. As also shown in the 0-D case, the initial time dependent behavior is incorrect and typically it takes multiple timesteps to correct to the small timestep probability. The necessitated use of multiple timesteps could be corrected if a higher order time differencing scheme is used. Nevertheless any of the timesteps selected yields the same SS POI.

7.2 Importance of Slab Thickness

To highlight the importance of the slab size on the time dependent solution, multiple slab thicknesses are presented. Slab sizes were chosen to be highly subcritical, exactly critical, and highly supercritical for emphasis. These results are shown in the figure below.

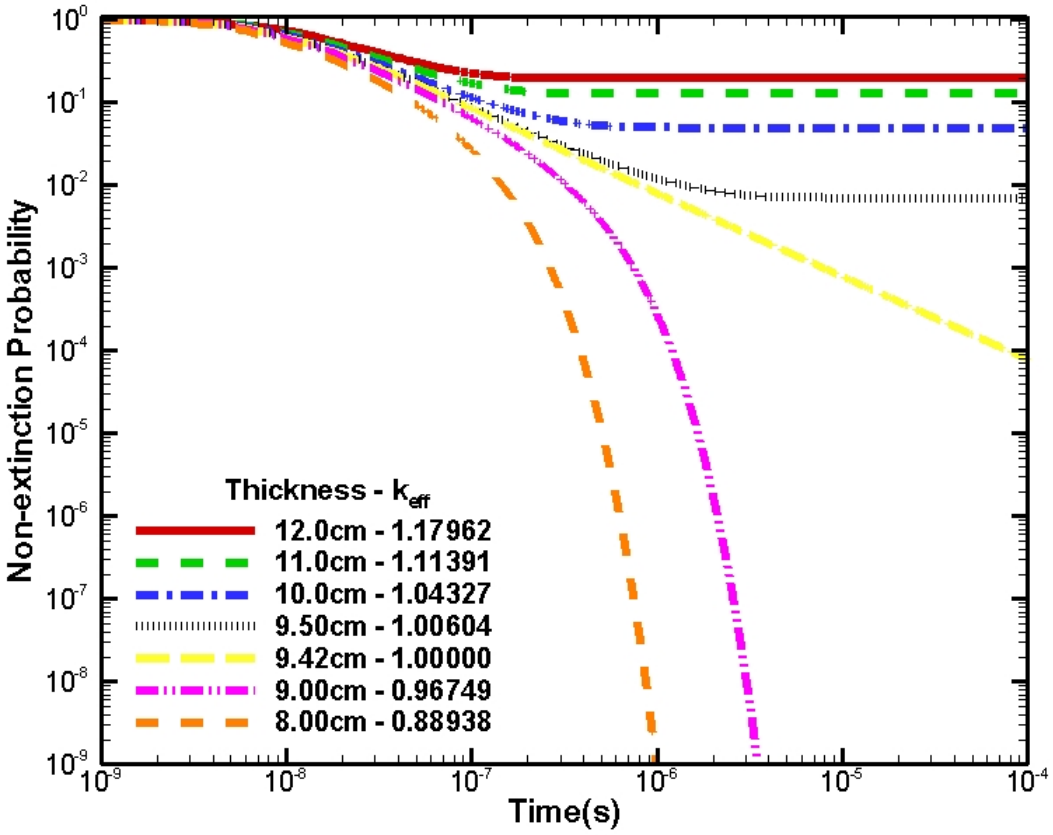

Figure 30: Importance of slab size on the time dependent survival probability.

As seen in 0-D, all neutron progeny in subcritical systems must go to zero at late times. As the slab becomes more subcritical, the descent to extinction is hastened. For a system exactly critical, the time dependent non-extinction probability also dies away as was seen in 0-D. For systems above prompt critical, a SS POI is reached. As the system becomes more prompt critical, the time at which the steady state value is reached diminishes and the overall magnitude of the POI increases.

The non-extinction probability as a function of the injection position, angle, and time was calculated. The resulting 3-D plot provides a graphical depiction of the impact of the injection position and angle on the non-extinction probability. As the time from the

injection increases, the resulting spatial shape is constant and only decreases in magnitude indicating a spatial mode has developed. The figure below only includes times up to the point at which the spatial shape was preserved for a system with $k_{eff} = 1.001$.

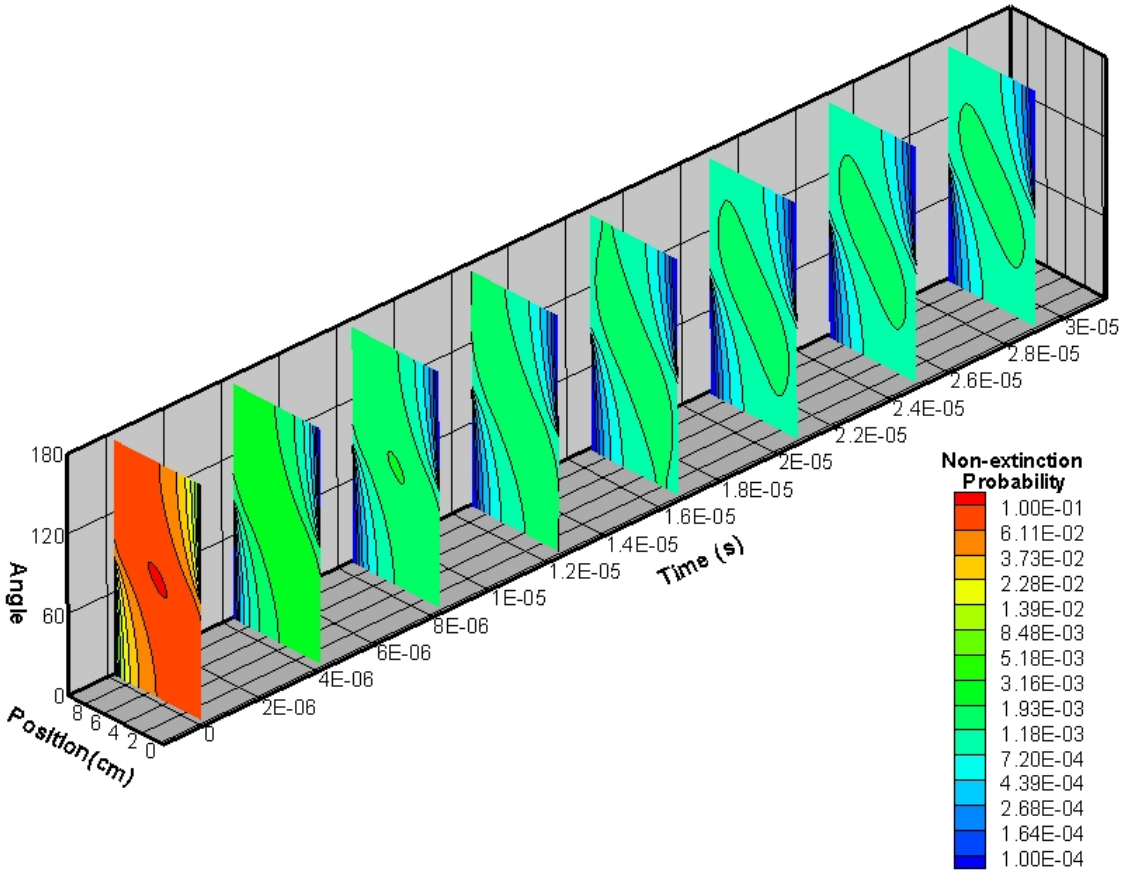

Figure 31: Non-extinction probability as a function of injection point, angle and time.

The non-extinction probability is plotted as a contour for the spatial, angular, and time domains. At times close to the initial condition, the non-extinction probability is at its largest value. The first contour shown corresponds to a time of 10^{-7} seconds. As the time from the initial condition increases, the magnitude of the non-extinction probability significantly decreases. The non-extinction probability is the highest at the center of the

slab and decreases for injection points at the slab edges. Relative to the slab edges, neutrons injected at highly peaked angles into the slab also have higher non-extinction probabilities. As anticipated, neutrons injected in directions traveling towards the slab edges have a significantly lower non-extinction probability. The shapes of the contours after times ~ $2*10^{-5}$ seconds are essentially constant and only begin to decrease in magnitude to the SS POI.

To illustrate the spatial shape of the non-extinction probability within the slab, the figure below plots the non-extinction probability as a function of the slab thickness. The non-extinction probabilities shown are the angular integrated values. Thus the non-extinction probability at any point within the slab represents the non-extinction probability for a neutron injected isotropically at that insertion time.

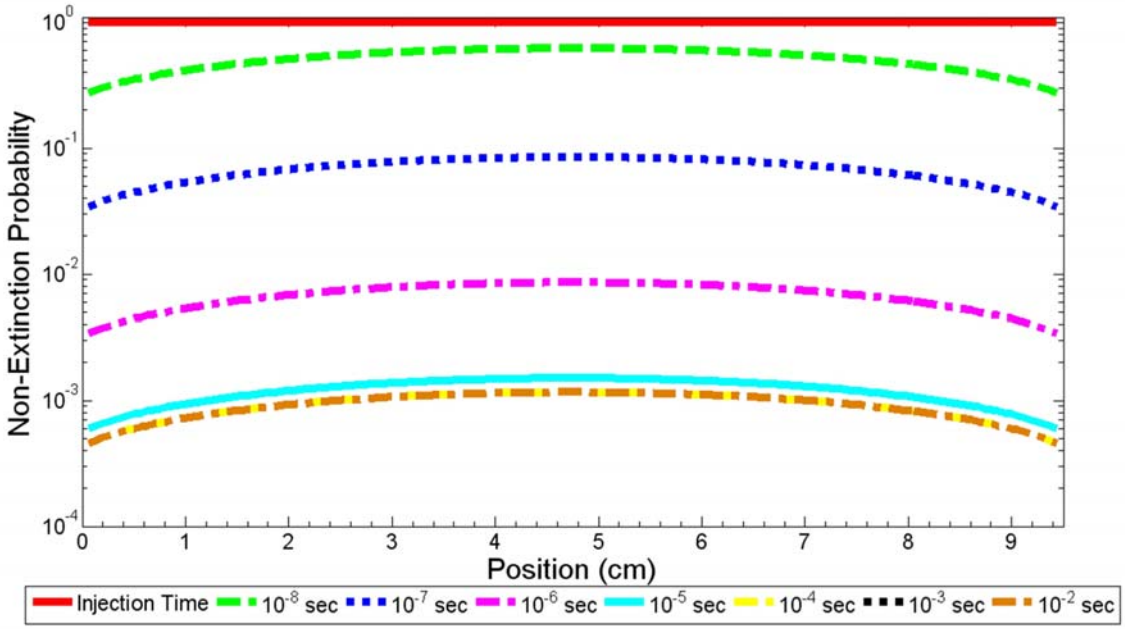

Figure 32: Spatially dependent non-extinction probability at different simulation times.

Almost immediately the solution begins to drop from the initial condition in magnitude and in addition, a spatial mode begins to develop. For sufficiently late times, the steady state profile has developed in the slab and does not change. Once this time has been reached $\left(t \geq 10^{-4}\right)$, the solution has reached the SS POI.

Using multiple slab thicknesses, the 1-D code was run until the SS POI value was reached. Similar to the 0-D results shown in Figure 15, the 1-D calculated SS POI combined with the calculated system multiplication factor is shown in the figure below for different fission truncations.

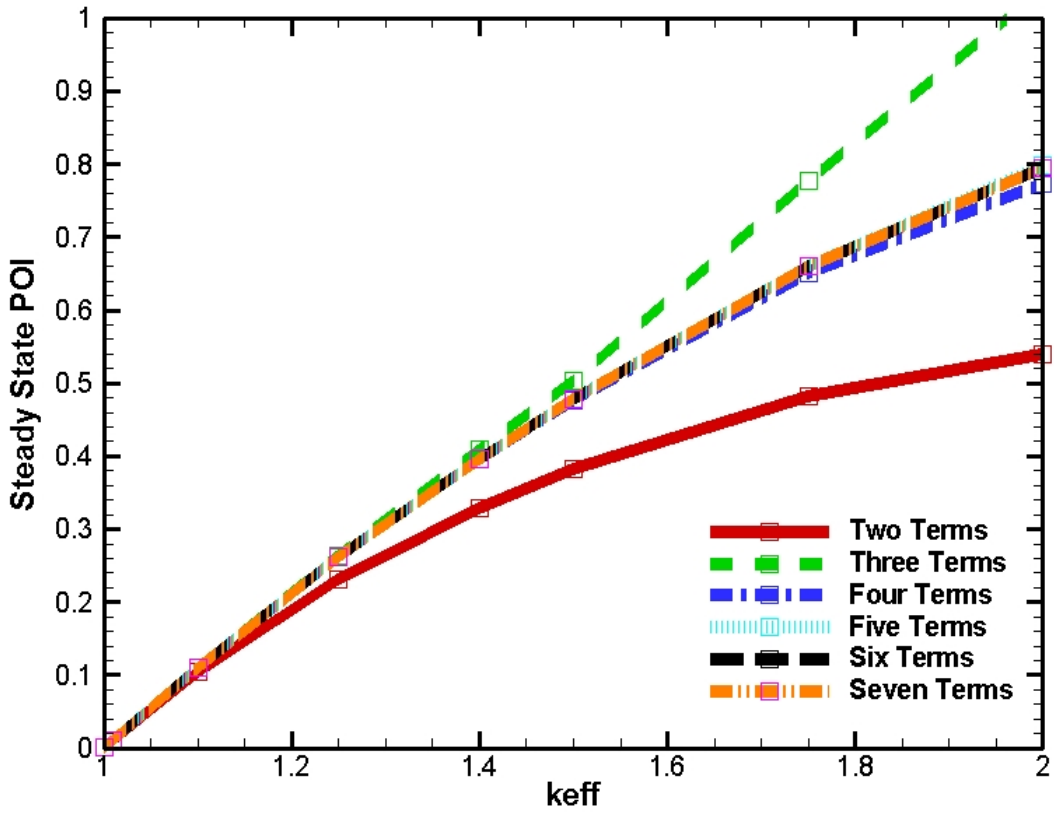

Figure 33: 1-D SS POI versus system multiplication factor.

The different fission truncations exhibit similar behavior to those seen in the 0-D analysis. The quadratic truncation underestimates the POI significantly while the cubic truncation overestimates the POI. For truncations fives terms or higher, little change is seen in the calculated SS POI. Also as expected there is a negligible difference in the fission truncations for small multiplication factor systems.

7.3 Linear vs. Adjoint Spatial Profile

It was noted by Bell and Lee for weakly prompt critical systems that the ratio of the linear solution (obtained from the linear k-eigenvalue search) to that of the non-linear non-extinction probability for an isotropic source is a constant (Bell 1976). As the multiplication factor increases, divergence from a constant should be seen. To test this comparison the angular integrated, spatially dependent non-extinction probability from the k-eigenvalue search is plotted along with the spatial solution from the non-linear problem at various timesteps. Multiple timesteps were plotted primarily due to the fact that the solution over the first few timesteps may be initially different due to the initial condition. The figure below plots the spatial solutions for a system with a multiplication factor of 1.001. As the magnitude of the non-extinction probabilities are all different, each of the curves below was normalized to the slab midpoint value. The goal was to highlight the differences across the length of the slab.

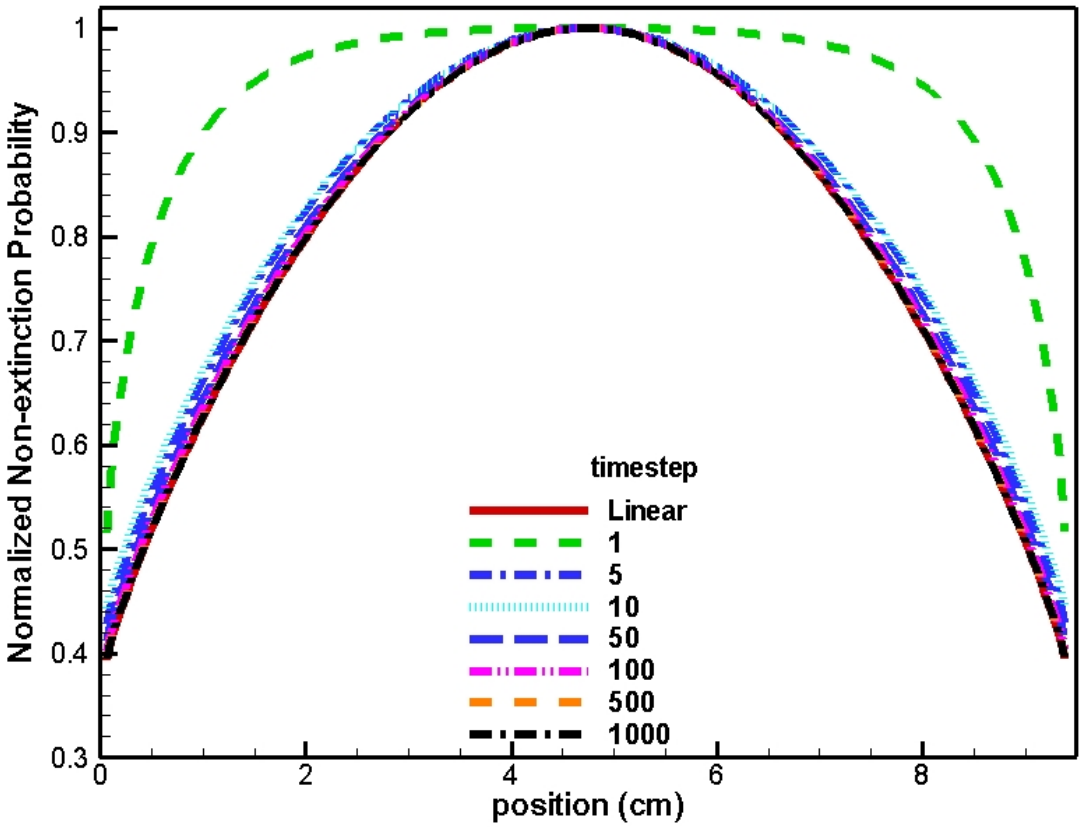

Figure 34: Ratio of k-eigenvalue to non-linear transport solution for k=1.001.

The linear solution is shown with a solid red line. The other curves correspond to the scalar solution at the end of the indicated timestep. The solution after multiple timesteps quickly relaxes to the same spatial shape as the linear problem. This confirms the statement made by Bell and Lee in that the forward equation provides decent solutions to the adjoint equation for small multiplication factors. The similarity between the results may not be much of a surprise as in one group calculations, the solution is self adjoint. The upper range of reactivity applicable to reactor operation is shown below for a multiplication factor of 1.01.

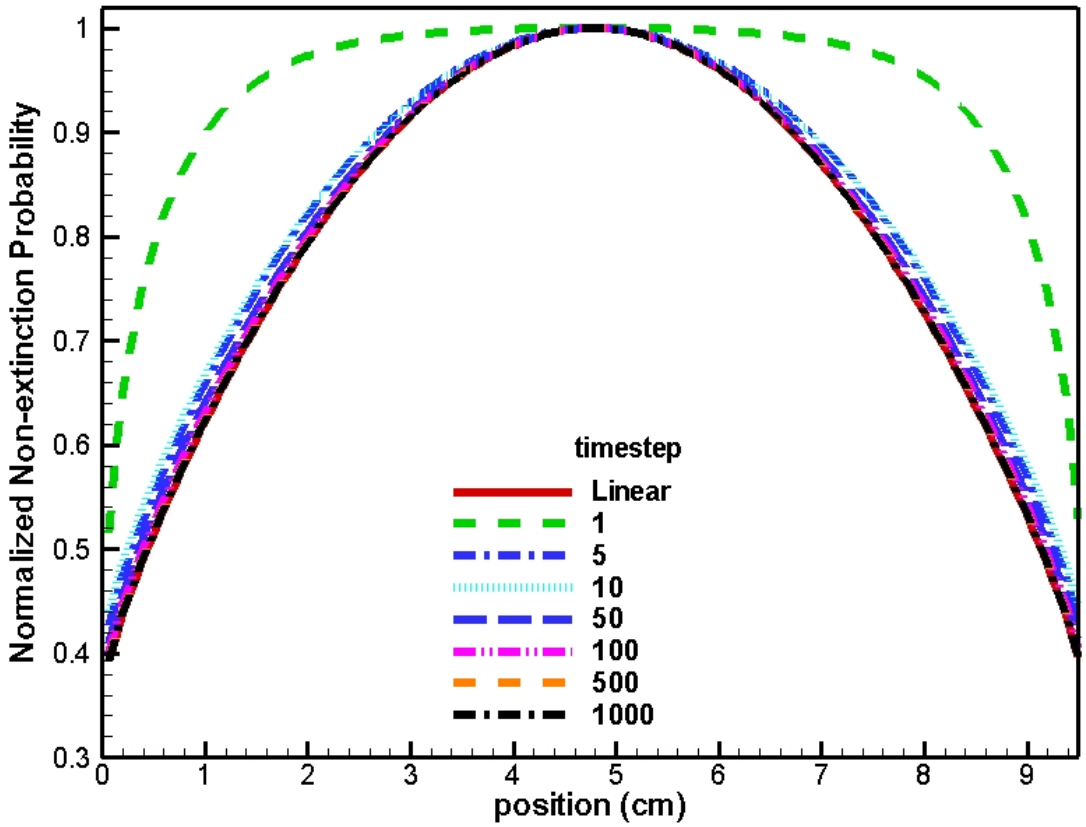

Figure 35: Ratio of k-eigenvalue to non-linear transport solution for k=1.01.

The spatial solution for the higher multiplication factor case still provides a decent match for the converged non-linear problem to the linear eigenvalue solution. As the multiplication factor is increased, a significant deviation develops between the two solutions. However the multiplication factors at which this occurs far exceed those seen in real systems. The benefit seen by the results shown in the two figures above is that it suggests that one may separate out the non-extinction probability, $p(x,\mu,t)$, into a spatial component, $p(x,\mu)$ found from the linear eigenvalue problem and a temporal component, $p(t)$. Thus for weakly prompt critical systems, one may assume that $p(x,\mu,t) = p(x,\mu)\cdot p(t)$. If the separation of variables assumption holds, this opens

windows for further analysis. The spatial solution, $p(x,\mu)$, could be found using a standard production code and then a point kinetics model could be used to describe the temporal component. The hybrid point kinetics model could then be used to quickly, and fairly accurately, describe the time dependent behavior and apply it to reactor systems of interest.

7.4 Dynamic Reactivity:

In an attempt to model a SPR like system in 1-D, a dynamic reactivity insertion was modeled by adding a reflector material adjacent to the reactor slab. Instead of having both sides of the slab being bare, one side of the slab is reflected by an aluminum reflector. There is no direct way to model a reflector insertion in a 1-D slab, an approximation was invoked through a time dependent albedo. The reflector material was assumed to be initially translucent. This is equivalent to making the reactor initially bare. Over time the reflector density is increased such that it becomes fully opaque at the final reflector insertion time. Thus neutrons which leak out of the core initially have a small probability of being reflected back into the reactor and at late times have a much larger probability of being reflected. Monoenergetic cross-sections were taken for aluminum. The values assumed are: $\Sigma_F = 0$ barns, $\Sigma_S = 3.70$ barns, and $\Sigma_T = 3.75$ barns. The figure below graphically shows the reflector transition.

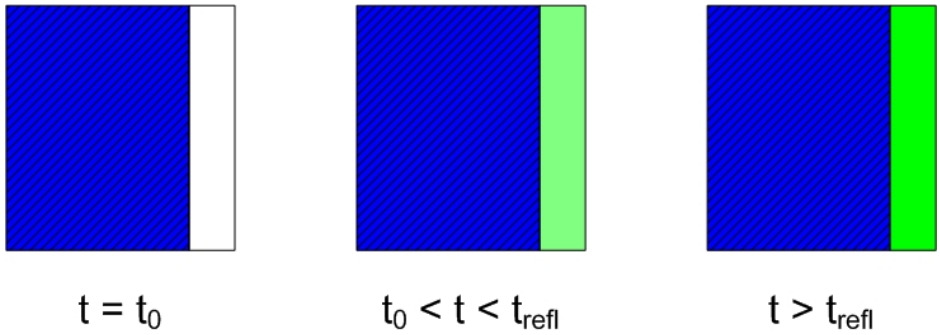

Figure 36: Graphical depiction of reflector insertion in 1-D.

Once the reflector element is completely inserted, it is held opaque for the remainder of the simulation. In order to determine the system multiplication factor, the standard k-eigenvalue search was performed. The system multiplication factor was calculated over the entire time domain of interest. The multiplication factor was initially fixed to 0.9998 and the final multiplication factor of 1.0137 was inserted over 10^{-4} seconds. This insertion is shown below.

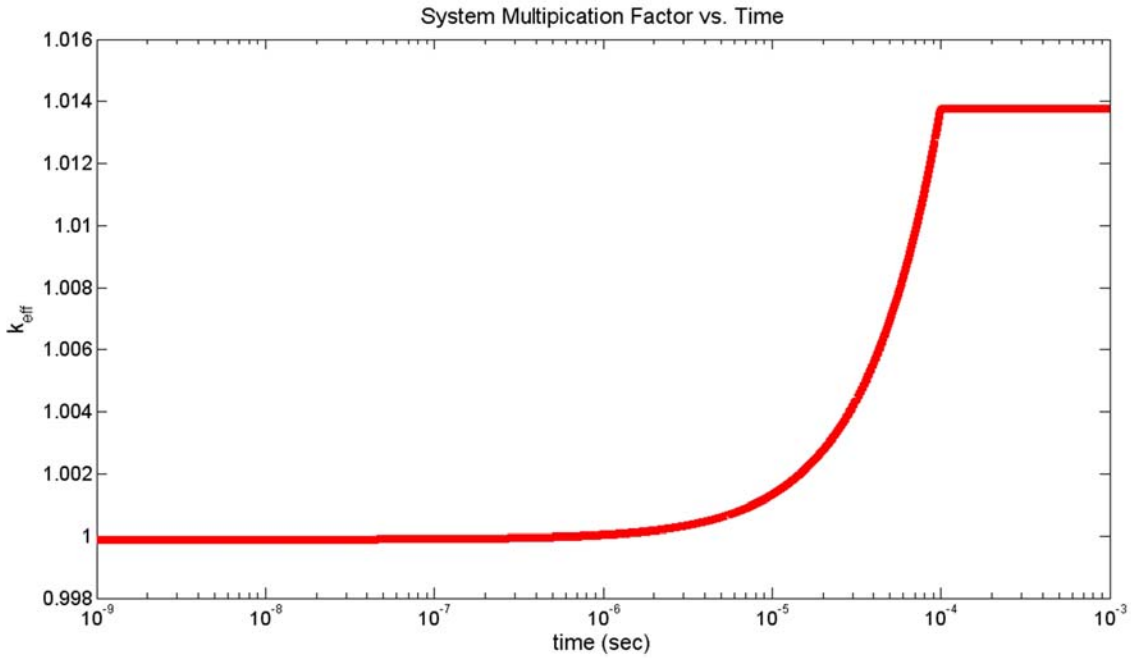

Figure 37: Dynamic reactivity insertion with external reflector element.

The figure shows that the system multiplication factor is inserted linearly over time. The system crosses critical at ~ $9*10^{-7}$ seconds. A 2-D contour plot is shown below at a time of 10^{-7} seconds. The contours represent the non-extinction probability as a function of the injection position and angle.

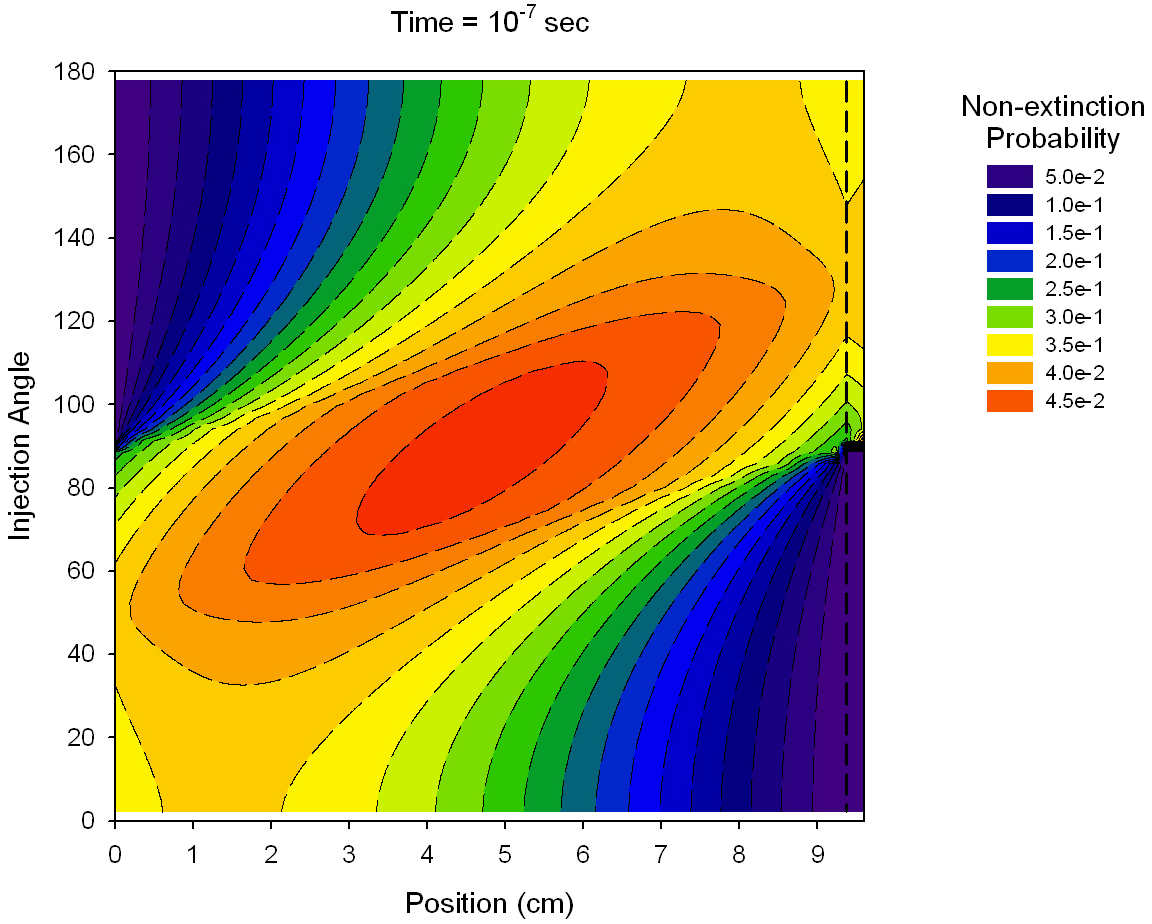

Figure 38: 2-D non-extinction probability contour plot of the injection point and angle at 10^{-7} sec.

For the contour plot shown, the reflector region is only ~ 0.1% opaque (shown by the vertical dotted line on the right hand side). The contour plot spans the spatial and angular domain. In the plot above, position 0 to 9.37 cm was occupied by the reactor fuel, and the remainder was occupied by the reflector. It is noted that for injection points within

the reflector that neutrons traveling away from the reactor lead to non-zero non-extinction probabilities (the zero non-extinction probability is shown in dark purple). The general shapes of the contours in the slab are similar to those seen above for a static system (Figure 31). The edge of the slab closest to the reflector exhibits higher non-extinction probabilities than the bare slab side. The highest non-extinction probability occurs at the middle of the slab at an injection angle of ~90°.

The contours shown above exhibit almost perfect symmetry due to the fact that the reflector was only marginally translucent at the time indicated. To highlight the difference in the contours, the same 2-D contour plot is provided at the full reflector insertion time. The figure below shows the contour at 10^{-4} seconds.

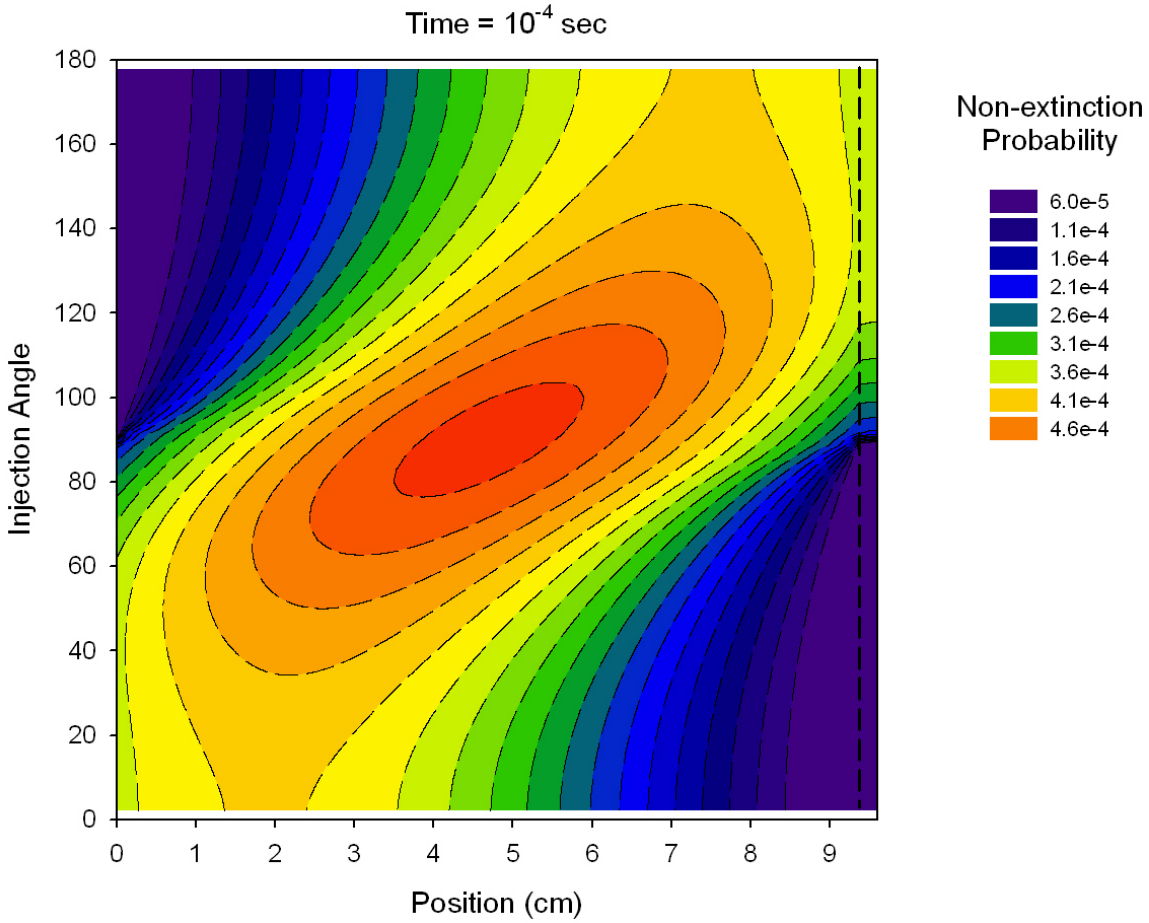

Figure 39: 2-D non-extinction probability contour plot of the injection point and angle at 10^{-4} sec.

Once the reflector is fully inserted localized increases are seen in the non-extinction probability. Even with the reflector fully inserted, small non-extinction probabilities are found for neutrons injected at highly peaked negative angles. The reflector is modeled with aluminum at a density of 2.7 g/cc which is ~ 6.3 times less dense than the uranium fuel. Thus even though the aluminum reduces the amount of leakage on the right face, the contours illustrate its overall effectiveness.

The non-extinction probability at the slab midpoint and the non-extinction probability within the last cell on the edge of the system (where the reflector is located) are plotted below.

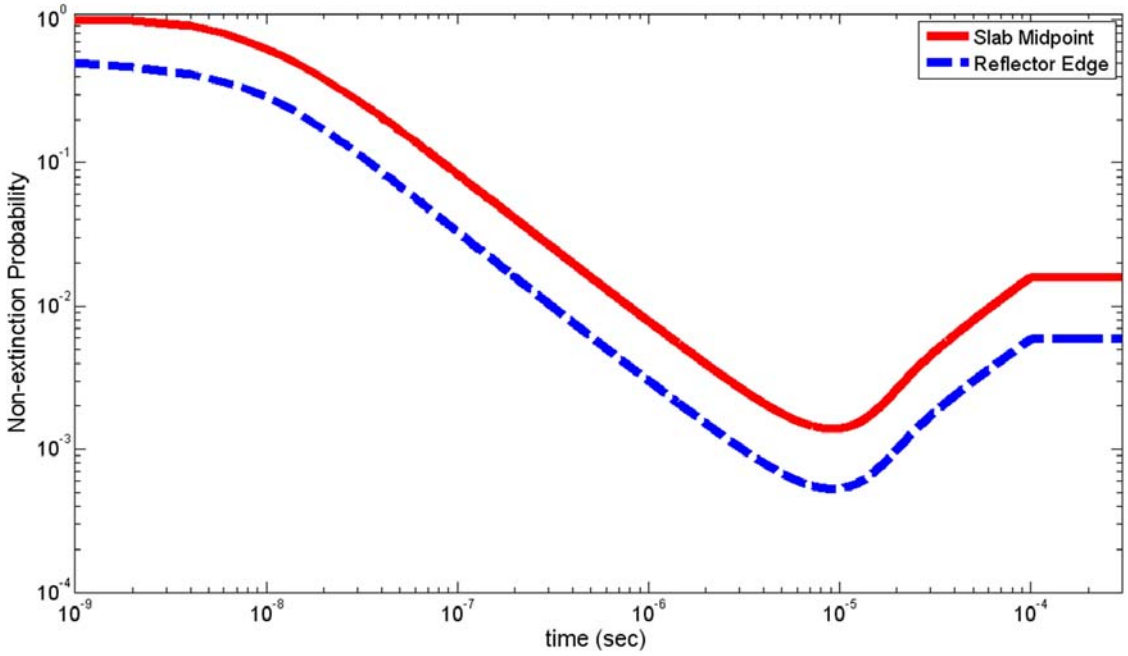

Figure 40: Time dependent non-extinction probability for the slab midpoint and reflector edge.

The slab midpoint curve exhibits a similar shape as those seen in the 0-D analysis section. Once the reflector is fully inserted, the non-extinction probability no longer increases and the POI has been reached. The reflector edge probability is initially one half as only neutrons injected into the direction of the slab can lead to a non-zero non-extinction probability. Neutrons injected into the reflector exhibit similar behavior as those in the slab, only lower in magnitude.

To highlight the importance of a constant internal neutron source, the non-extinction probability results shown above were folded into a constant neutron source. At discrete timesteps, the angular and spatial integrated non-extinction probabilities were tabulated. These were then accrued and post-processed to give the source non-extinction probability. Although presented previously for general systems, the source non-extinction probability for the slab system is calculated through:

$$P_S(t) = 1 - e^{-\frac{L}{2}\cdot\int_{t_0}^{t}\int_{0}^{L}\int_{-1}^{1} S(x',\mu',t')\cdot p(x',\mu',t')\cdot dx'\cdot d\mu'\cdot dt'} \tag{107}$$

Assuming the source emits neutrons uniformly throughout the slab allows it to be pulled out of the integrals. Note, this also implies that the source emits neutrons within the reflector which indicates a physical unreality. The figure below plots the source non-extinction probability for the dynamic reactivity case shown above for various source strengths.

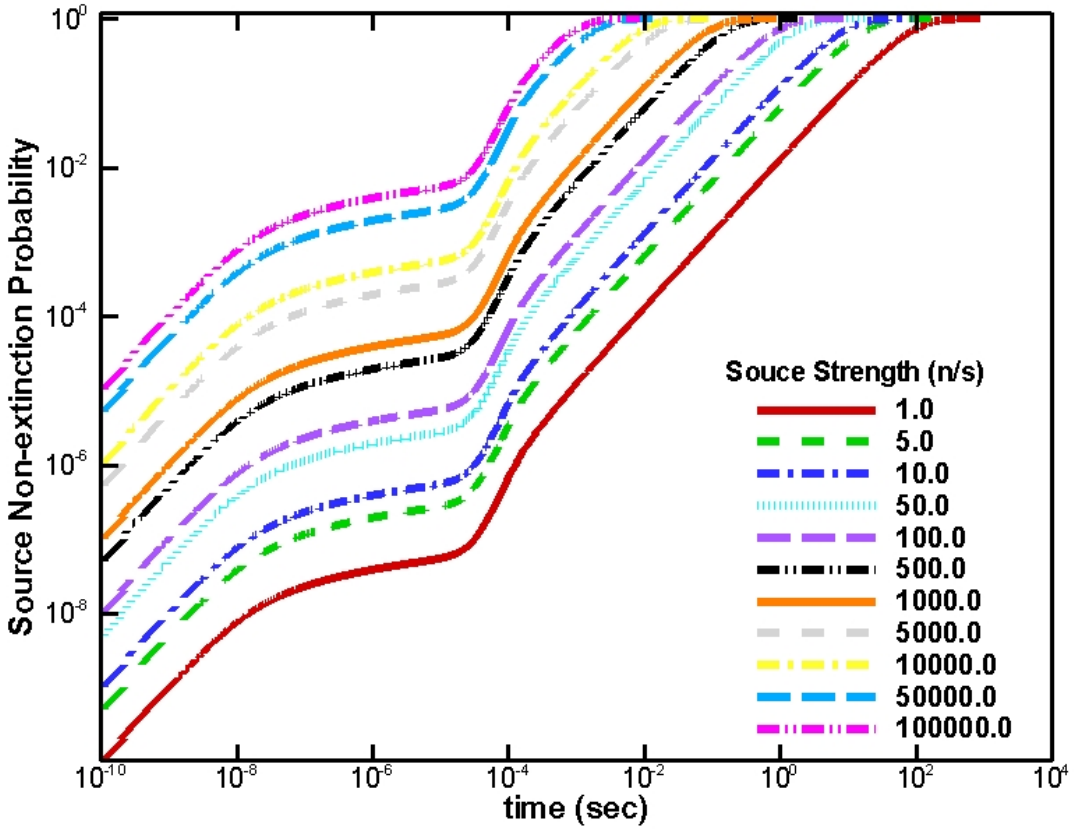

Figure 41: Source non-extinction probability for dynamic reactivity insertion.

The shapes of the curves are similar to those seen in 0-D. The source non-extinction probability increases and then nearly becomes constant. This region corresponds to the non-extinction probability being subcritical. As the POI value is approached, the source non-extinction probability increases. In addition, as the source strength is increased the time to assure divergence also increases. Confirming the results seen in 0-D, marginal increases in the source strength equate to large differences in the time to divergence.

CHAPTER 8: ITERATION PERFORMANCE

So far discussion has only been geared towards the numerical solution of the non-extinction probability without any focus on the numerical performance of the routines. This chapter shifts from a focus on the exact time dependent solution to instead focus on how the solution was obtained numerically; namely the iterations needed to achieve convergence. Details regarding each of the iteration schemes were shown earlier. For the iteration performance analysis only static reactivities are considered. Numerical results were presented previously for the impact of the timestep on the overall non-extinction probability. It was illustrated that in order to resolve the full time dependent non-extinction probability small timesteps must be used. Little focus was presented on the iteration performance of the timestep and how it impacts the iteration behavior. Small timesteps must be used to provide adequate resolution of the time domain. Large timesteps can be used to allow the user to reach the SS POI in a few timesteps. This is desirable for scoping studies where the full time dependent behavior is not needed. Thus even though the SS POI may be always be achieved, how the iteration routines behave while getting to the POI and the value of the POI at that point (when convergence is obtained) will also be discussed.

8.1 Fixed Point Iteration Routine

In the standard fixed point iteration routine, there is only one iteration loop in monoenergetic problems. For the purposes of future comparisons, it will be considered an inner iteration. To illustrate the performance of this routine with the single iteration loop the figure below shows two families of curves; one for a small timestep (1 ns) and the other for a large timestep (1e9 ns). For each timestep presented, multiple cases are shown which range across the entire spectrum of multiplication factors. The intent of the figure is not to trace every single curve (as many overlay one another); rather it is to see general trends.

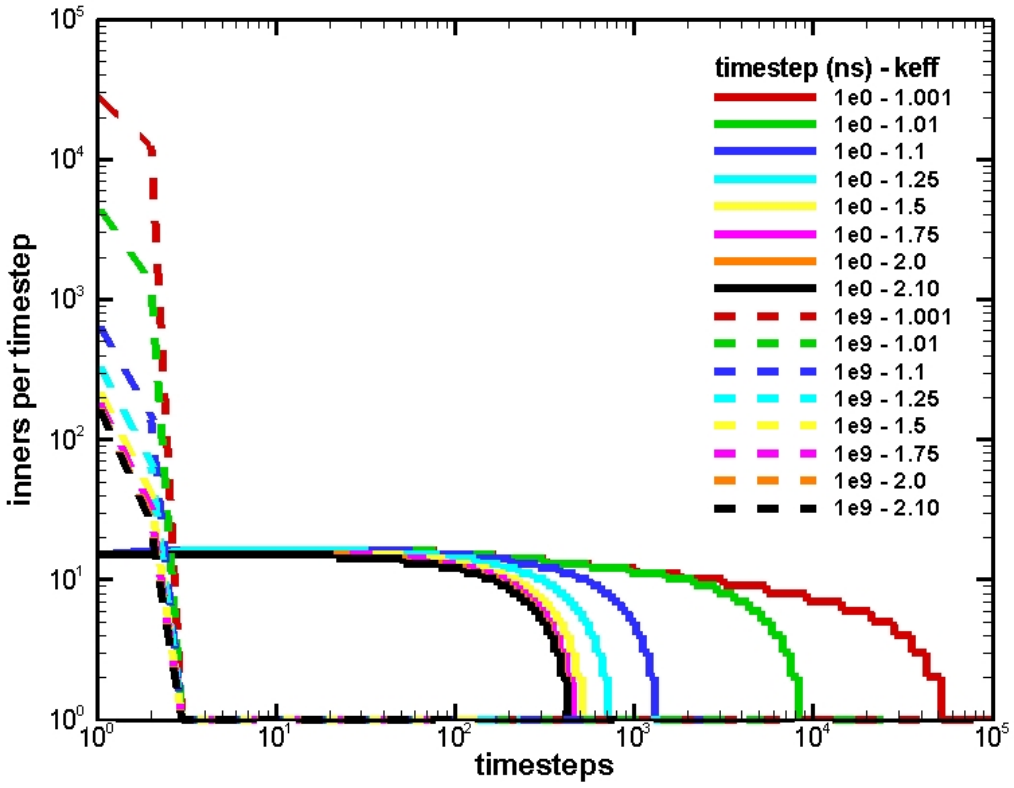

Figure 42: Number of iterations per timestep for the source iteration routine with full multiplicity.

The figure plots the total number of iterations needed to reach SS. The x-axis for the two families of curves may be plotted against one another despite that these refer to different times (since the timesteps were different). The large timestep curves are shown in dashed lines. The lowest system multiplication factor case $(k = 1.001)$ took the longest to reach SS with a total iteration count of 451,961 for a small timestep. In addition for the large timestep cases, the number of iterations needed is quite high. For the lowest multiplication factor case some 40,716 were needed during the first two timesteps. The large number of iterations needed is primarily due to the fact that the non-extinction probability at the initial condition is one. As the source neutron is injected at some point into the distant past, the code is trying to reach the SS POI in one pass. Thus it is spending much time trying to resolve the SS solution. For such small prompt reactivity cases, this can be a formidable challenge as the SS POI values are typically quite small. The fixed point iteration is a standard routine commonly used in iterative numerical problems. The figure above shows that although the routine can solve the non-linear equation, large numbers of iterations may be needed; particularly for large simulation timesteps. The benefit of examination of the fixed point iteration routine is that it highlights that even a rudimentary iteration scheme is able to solve non-linear problem. Results are only presented for the full fission multiplicity as there is little difference seen between the quadratic results and those shown above. Such similarities do not hold for the other iteration routines investigated.

8.2 Outer Iteration Behavior

Given the poor performance of the fixed point iteration routine, focus was diverted to a lagged routine. Removing the fission terms from the inner sweeps allows for rapid convergence of the inner scattering iterations. Issues associated with resolving the fission terms can be borne out in the segregated outer iteration. An examination of the outer iterations is provided. The total number of outers per timestep was examined; similar to that of the inners shown above where both small and large timestep behavior were examined.

8.3 Lagged Fission Source Routine

Using the lagged source routine, plots of the outers to SS are provided. The plot below shows the total number of outers used for each timestep for the full multiplicity using a small timestep. In order to retain some of the detail, small and large timestep cases were unable to be plotted on the same figure. Two figures are provided, the first for the small timestep and the second for the large timestep.

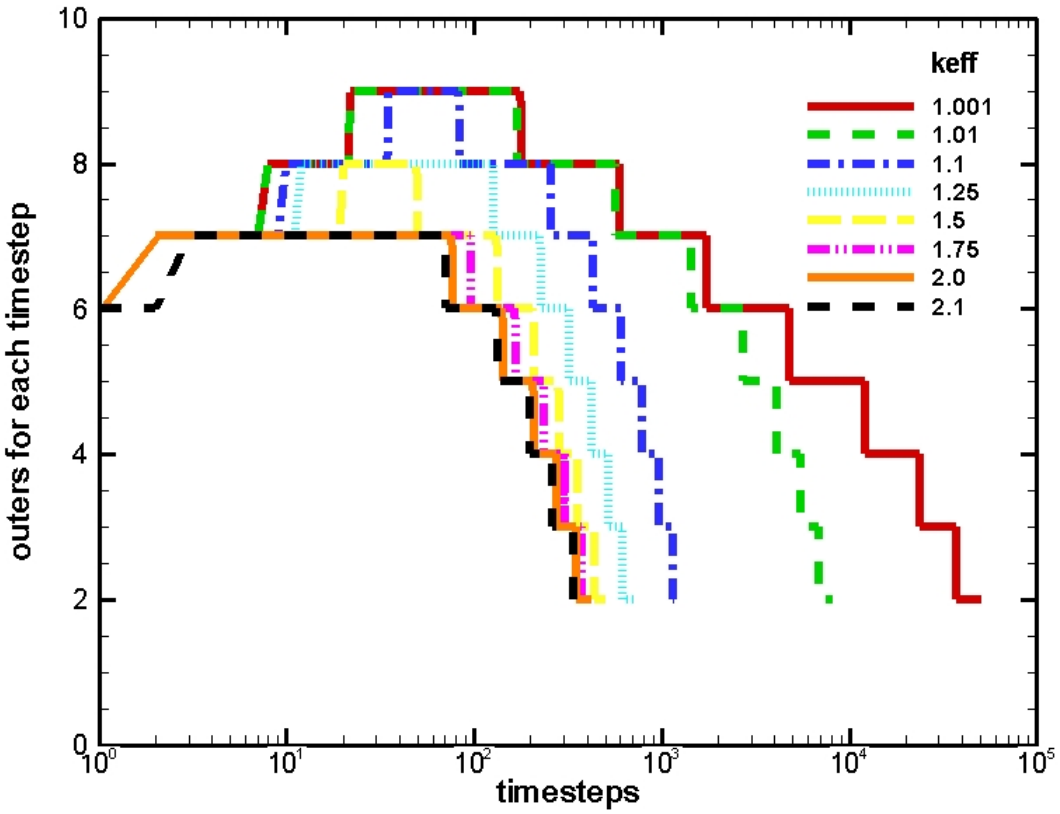

Figure 43: Outers per timestep seven term multiplicity lagged fission source routine, small timestep.

Using the full multiplicity, the total number of outers for each timestep is presented using a timestep of 1 ns. As expected, the low multiplication factor cases took the longest to reach SS. The number of outers for each timestep is essentially constant and small across the entire time domain. As was seen with the source iteration routine, despite the small number of outers for each timestep, there were still a total of 181,884 outer iterations to reach SS for the low multiplication factor case.

The same plot for a large timestep of 1 sec using the full multiplicity are presented below.

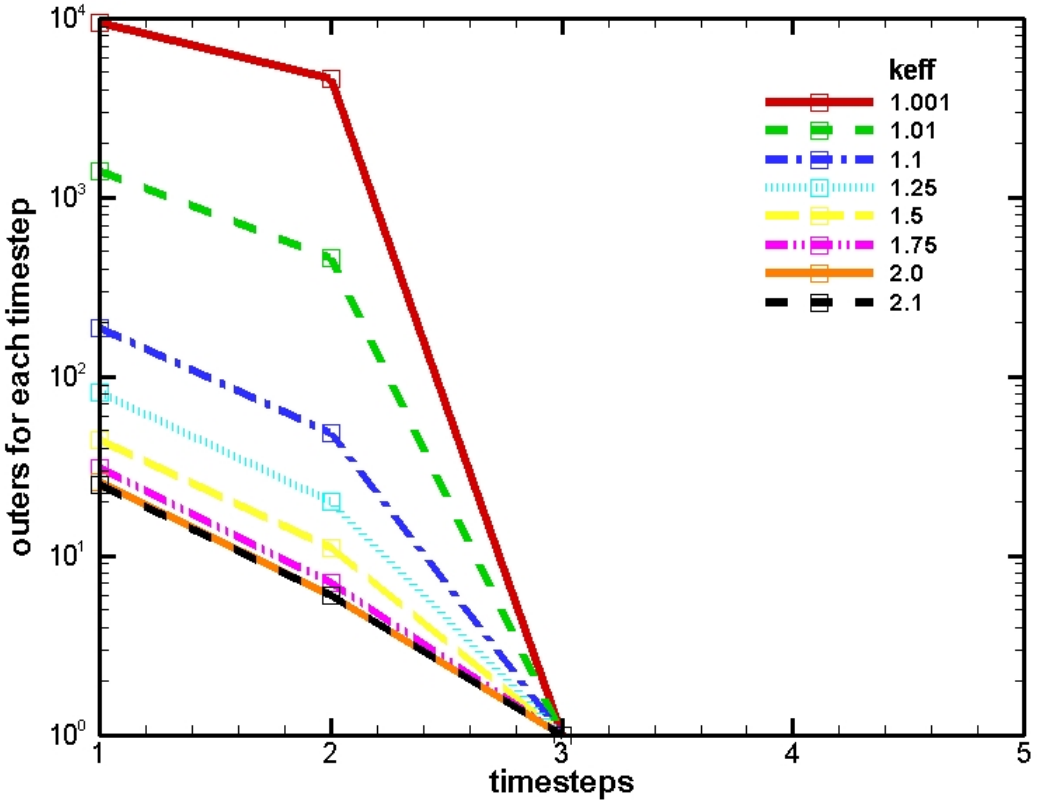

Figure 44: Outers per timestep seven term multiplicity lagged fission source routine, large timestep.

Using a large timestep, similar results are seen with the fixed point iteration routine. Only a few timesteps are needed to reach the SS POI. The small multiplication factor cases exhibit the largest number of outers needed to reach SS. For the $k = 1.001$ case presented above, a total of 14,024 outer iterations were required to reach SS.

The number of outers shown above may be misleading with respect to the non-extinction probability after each of these timesteps. The small multiplication factor cases require more iterations as the SS POI value is much lower than the higher multiplication factor cases. This can be illustrated with the results shown in the table below for the slab midpoint non-extinction probability.

Table 10: Non-extinction probability after each timestep.

k_{eff}	Non-extinction Probability		
	1st timestep	2nd timestep	3rd timestep
1.001	0.0011651427	0.0011566860	0.0011566859
1.01	0.0115420968	0.0115412421	0.0115412420
1.1	0.1109860571	0.1109859677	0.1109859676
1.25	0.2613891479	0.2613891104	0.2613891103
1.5	0.4785057870	0.4785057681	0.4785057680
1.75	0.6602618856	0.6602618745	0.6602618744
2.0	0.7956149506	0.7956149451	0.7956149450
2.1	0.8216860014	0.8216859974	0.8216859974

For most of the multiplication factors shown, the SS POI is nearly reached in the first timestep. Multiple timesteps are needed to increase the accuracy of the calculated POI. Using a higher order scheme (particularly in time) could result in the POI being reached in the first timestep alone; however, the large number of outer iterations would still be present.

Results generated for both the two terms (not presented) and seven terms were combined into a concise format. The total number of outers to reach the SS POI (over the entire time domain) is divided by the number of timesteps to reach the POI. These are then plotted against the system multiplication factor.

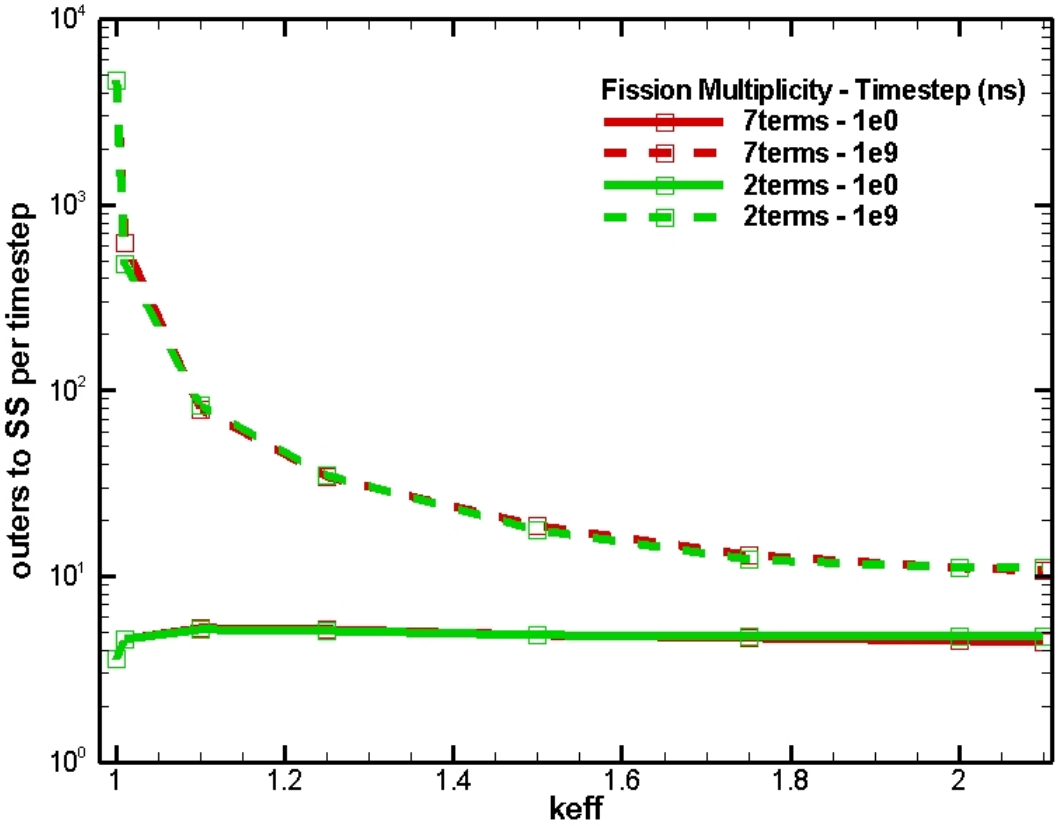

Figure 45: Outers to SS per timestep for the lagged fission source routine.

When the total number of outers to reach SS is divided by the number of timesteps to reach the POI, a proper comparison can be made between the results. For both of the small timestep cases, it takes on average approximately 3-4 outers per timestep to reach SS across the entire multiplication factor domain. For the large timestep case, the number of outers is quite variable. For small system multiplication factors both cases have high numbers of outers per timestep. As the multiplication factor is increased, the number of outers decreases. This large number of outer iterations seen with large timesteps lead to the idea of the linearized routine as a means to speed up the calculation to SS. Acceleration of linear routines (particularly the neutron transport equation) has been addressed for some time now in the literature. Linearizing the routine allows one to

take advantage of such acceleration schemes; in addition, it allows one to perform theoretical analysis of the discretized equation.

8.4 Linearized Lagged Fission Source Routine

In addition to the large iteration counts seen above, the linearized routine was implemented such that a valid comparison to the theory could be made. Linearizing the equation transforms the overall non-linear pde into a linear one. Prior to delving into the theoretical analysis of the routine, numerical performance results are provided. The small timestep case for the linearized routine is not included as the results are nearly identical to the performance of the lagged routine. The results for a large timestep however are shown below.

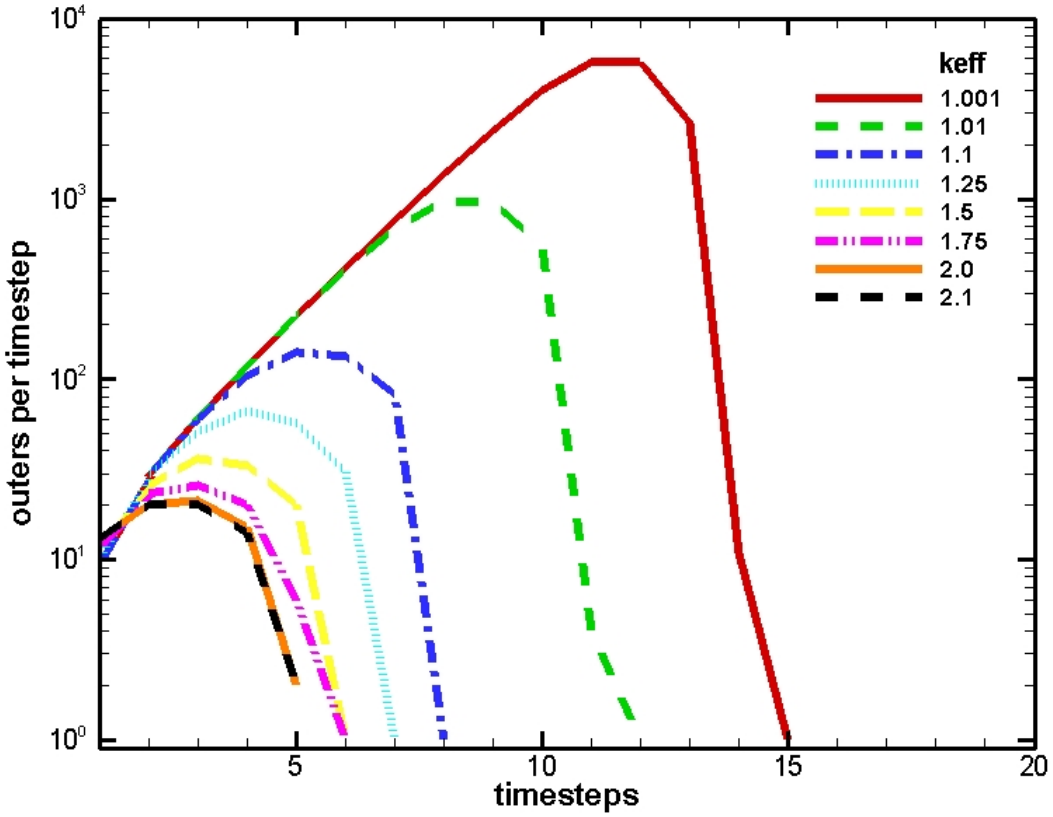

Figure 46: Outers per timestep seven term multiplicity linearized routine, large timestep, linearization about $p_0 = 2$.

Using a large timestep, different results are seen for the number of outers for each timestep. Initially the number of outers was small which was promising. For the small multiplication factor cases the number of outer iterations increases dramatically after several timesteps. The high multiplication factor cases had the lowest number of outers for each timestep. For the low multiplication factor case, the total number of outers to reach the POI was 23,479. Despite the large number of outer iterations, it appears that as the POI is reached convergence becomes more taxing. The increasing behavior for small multiplication factor cases was the driver behind the theoretical analysis to follow. As

was shown for the lagged routine, the non-extinction probability after various timesteps is shown for selected cases.

Table 11: Non-extinction probability after each timestep.

timestep	$k_{eff} = 1.001$	$k_{eff} = 1.01$	$k_{eff} = 1.5$	$k_{eff} = 2.0$
1	0.3999327954	0.4039100712	0.6249198048	0.8202648156
2	0.1857925449	0.1905607674	0.5033448640	0.7966400642
3	0.0895992718	0.0946949770	0.4794958177	0.7956182750
4	0.0441908607	0.0495290023	0.4785074091	0.7956149452
5	0.0221677464	0.0278155184	0.4785057706	0.7956149451
6	0.0113265144	0.0174991608	0.4785057705	
7	0.0059545496	0.0130452834		
8	0.0032942207	0.0116958741		
9	0.0019970467	0.0115432490		
10	0.0014053978	0.0115412425		
11	0.0011940578	0.0115412421		
12	0.0011578195	0.0115412421		
13	0.0011566870			
14	0.0011566859			
15	0.0011566858			

Unlike the lagged routine where the POI was nearly reached in the first timestep, the linearized routine results show a much greater variation. This should not be a surprise as the problem being solved is the linearized linear problem and not the non-linear problem of interest. However, after multiple timesteps the solution to the linear problem tends to that of the non-linear problem. The troublesome feature of the routine is the fact that as the POI is approached the iteration count continues to increase. Take the $k = 1.001$ case for example. At the 10-12 iteration, the POI is nearly reached, yet the iteration count is at its highest. Relaxing the convergence criteria on when the POI is reached can alleviate some of the iteration counts.

Similar results were generated for the quadratic truncation and also small timesteps for both cases. It was interesting to note that when a large timestep was chosen, that a number of the quadratic cases did not converge. For the combined plot shown below, the quadratic large timestep curve only had two points at which the code converged.

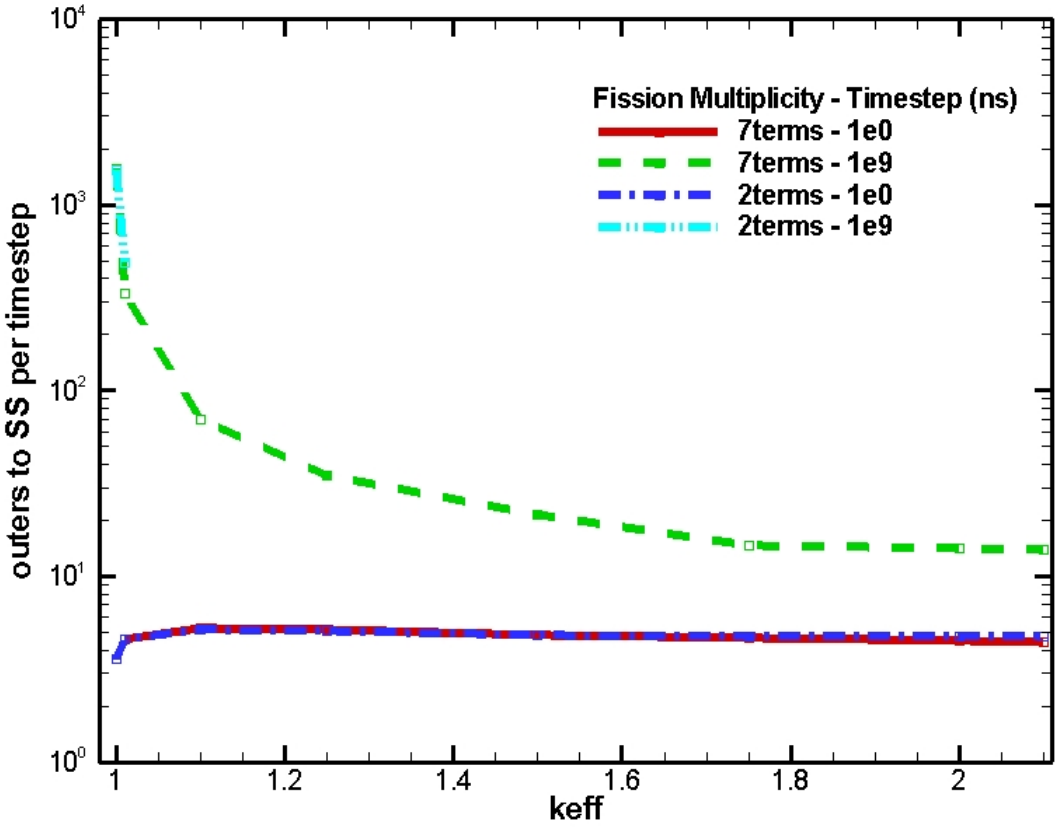

Figure 47: Outers to SS per timestep for the linearized lagged fission routine linearization about $p_0 = 2$.

When the results are combined such that the number of outers to reach SS is divided by the number of timesteps to reach SS, similar results are seen as for the lagged fission source routine. For the small timestep cases small numbers of outers are seen across the entire fission multiplicity. For the large timestep cases, the full multiplicity performance

increases as the multiplication factor increases. For the quadratic truncation where the time absorption term goes to zero only a few of the large timestep cases converged. This will be explained in the theoretical analysis below.

8.4.1 Spectral Radius – Linearized Routine

The numerical performance of the linearized routine has been shown. Given the behavior seen in Figure 47, focus was shifted to a Fourier analysis of the iteration routine. Fourier analysis provides a means to analyze the stability of a linear numerical routine with some implicit assumptions. The most restrictive assumption is that the analysis assumes a time independent infinite homogenous medium. The analysis therefore begins by using the SS form of the equation linearized about the infinite medium constant.

$$\mu \cdot \frac{\partial p(x,\mu)}{\partial x} + \left(\Sigma_T + \frac{1}{v \cdot \Delta t} \right) \cdot p(x,\mu) = \frac{\Sigma_S}{2} \cdot p_0(x) + N'_\infty \cdot p_0(x) + Q(x,\mu) \tag{108}$$

Define the outer iteration error as the difference between the exact equation and the discretized equation:

$$\varepsilon^{(l+1)}(x,\mu) = p(x,\mu) - p^{(l+1)}(x,\mu) \text{ and } \varepsilon_0{}^{(l+1)}(x) = p_0(x) - p_0{}^{(l+1)}(x) \tag{109}$$

Subtracting the iteration equation from the exact equation and using the error definitions:

$$\mu \cdot \frac{\partial \varepsilon^{(l+1)}(x,\mu)}{\partial x} + \left(\Sigma_T + \frac{1}{v \cdot \Delta t} \right) \cdot \varepsilon^{(l+1)}(x,\mu) = \Sigma_S \cdot \frac{\varepsilon_0{}^{(l+1)}(x)}{2} + N'_\infty \cdot \varepsilon_0{}^{(l)}(x) \tag{110}$$

The Fourier analysis assumes that the error iterate takes the following form: $\varepsilon^{(l+1)}(x,\mu) = A^{(l+1)}(\mu)\cdot e^{i\omega x}$ where the first term on the right hand side represents the angular amplitude and the second represents spatial modes where ω is a real wave number.

This form for the error is then plugged into the error equation:

$$i\omega\cdot\mu\cdot A^{(l+1)}(\mu)\cdot e^{i\omega x} + \left(\Sigma_T + \frac{1}{v\cdot\Delta t}\right)\cdot A^{(l+1)}(\mu)\cdot e^{i\omega x} = \frac{\Sigma_S}{2}\cdot A_0^{(l+1)}\cdot e^{i\omega x} + N'_{\infty}\cdot\left(A_0^{(l)}\cdot e^{i\omega x}\right) \tag{111}$$

It is assumed that there is linear independence of each of the ω error modes such that:

$$\left(i\omega\cdot\mu + \left(\Sigma_T + \frac{1}{v\cdot\Delta t}\right)\right)\cdot A^{(l+1)}(\mu) = \frac{\Sigma_S}{2}\cdot A_0^{(l+1)} + N'_{\infty}\cdot\left(A_0^{(l)}\right) \tag{112}$$

A relationship between the error amplitudes at successive iterations is found from:

$$A^{(l+1)}(\mu) = \frac{\Sigma_S}{2}\cdot\frac{A_0^{(l+1)}}{\left(i\omega\cdot\mu + \left(\Sigma_T + \frac{1}{v\cdot\Delta t}\right)\right)} + \frac{N'_{\infty}}{\left(i\omega\cdot\mu + \left(\Sigma_T + \frac{1}{v\cdot\Delta t}\right)\right)}\cdot\left(A_0^{(l)}\right) \tag{113}$$

The quantity on the left hand side is angular dependent, while the terms on the right are scalar. To eliminate this problem, the relationship is then integrated over the angular domain of [-1,1] to yield:

$$A_0^{(l+1)} \cdot \left[1 - \frac{\Sigma_S}{2 \cdot i\omega} \cdot \ln \frac{\left(i\omega + \Sigma_T + \frac{1}{v \cdot \Delta t} \right)}{\left(-i\omega + \Sigma_T + \frac{1}{v \cdot \Delta t} \right)} \right] = A_0^{(l)} \cdot \frac{N'_\infty}{(i\omega)} \cdot \ln \frac{\left(i\omega + \Sigma_T + \frac{1}{v \cdot \Delta t} \right)}{\left(-i\omega + \Sigma_T + \frac{1}{v \cdot \Delta t} \right)} \quad (114)$$

In compact form, the relationship between successive iterations can be expressed as:

$$A_0^{(l+1)} = A_0^{(l)} \cdot \gamma(\omega) \quad (115)$$

where

$$\gamma(\omega) = \frac{\frac{N'_\infty}{(i\omega)} \cdot \ln \frac{\left(i\omega + \left(\Sigma_T + \frac{1}{v \cdot \Delta t} \right) \right)}{\left(-i\omega + \left(\Sigma_T + \frac{1}{v \cdot \Delta t} \right) \right)}}{\left[1 - \frac{\Sigma_S}{2 \cdot i\omega} \cdot \ln \frac{\left(i\omega + \left(\Sigma_T + \frac{1}{v \cdot \Delta t} \right) \right)}{\left(-i\omega + \left(\Sigma_T + \frac{1}{v \cdot \Delta t} \right) \right)} \right]} \quad (116)$$

It is noted that for multiple iterations, the relative change in the error amplitude can be found from:

$$A_0^{(l+1)} = A_0^{(0)} \cdot \gamma^{(l)}(\omega) \text{ or } \gamma^{(l)}(\omega) = \frac{A_0^{(l+1)}}{A_0^{(0)}} \quad (117)$$

To ensure numerical convergence it is necessary to show that $\max_{\omega}|\gamma(\omega)|<1$ for all ω. The value of ω that yields the maximum of $\gamma(\omega)$ is defined as the spectral radius, ρ, such that $\rho=\max_{\omega}|\gamma(\omega)|$. Plugging in the expression for $\gamma(\omega)$ and with some algebra:

$$\rho=\frac{2}{\Sigma_S}\cdot\left|N'_{\infty}\right|\cdot\left|\frac{1}{1-\frac{\Sigma_S}{\omega}\cdot\tan^{-1}\left(\frac{\omega}{\left(\Sigma_T+\frac{1}{v\cdot\Delta t}\right)}\right)}-1\right| \tag{118}$$

A plot of the dispersion function, $\gamma(\omega)$, versus wave number, ω, is provided below for the full fission multiplicity and quadratic truncation.

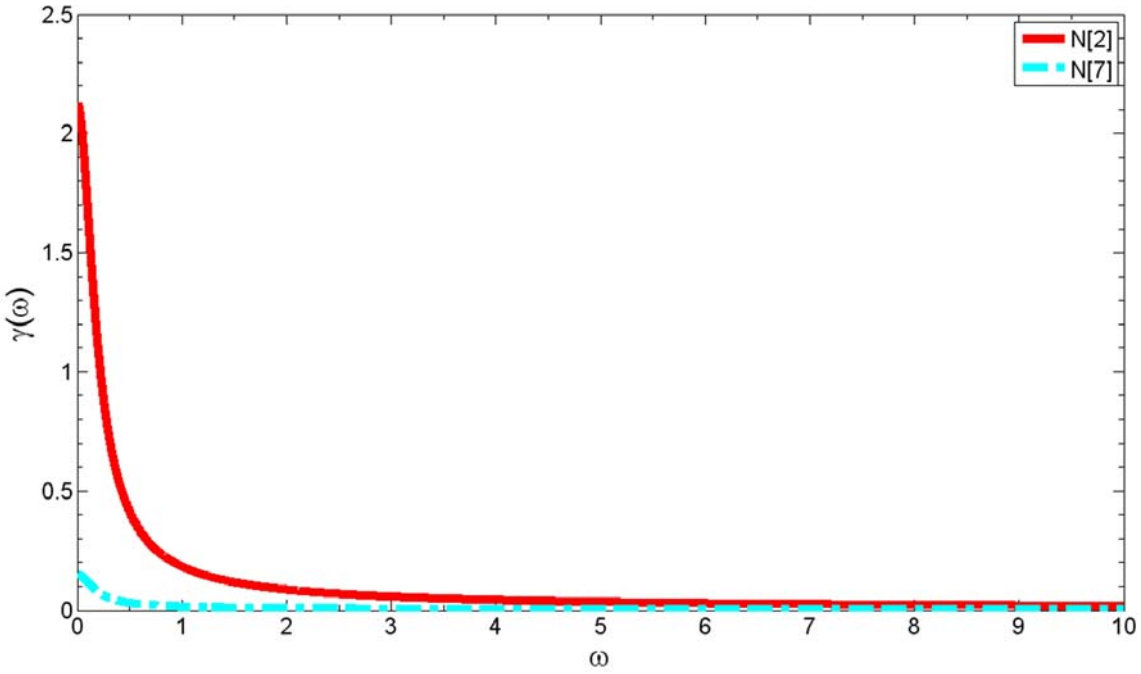

Figure 48: Iteration amplitude as a function of the wave number.

For both cases the largest value of $\gamma(\omega)$ occurs for the $\omega = 0$ mode. For the different fission truncations, the spectral radius will take on different values relative to the infinite multiplication factor. The figure above shows that the spectral radius is greater than one for the quadratic truncation (2.135) and much less than one for the full multiplicity (0.152) at the $\omega = 0$ mode. The fact that the spectral radius is so large provides some clues as to why some of the quadratic cases would not converge. Plugging this into the spectral radius relationship yields:

$$\rho = \frac{2}{\left(\Sigma_A + \frac{1}{v \cdot \Delta t}\right)} \cdot \left|N'_{\infty}\right| \tag{119}$$

The results shown above were provided for a linearization constant equal to 2. This constant corresponds to the linearization performed over the first timestep. Numerically, the linearization constant is taken to be the converged spatial solution obtained from the previous timestep. The Fourier analysis requires the system to be infinite, and thus there is no spatial dependence. Despite this, the magnitude of the spatial profile obtained numerically after successive iterations decreases as the POI is approached. The linearization constants (spatially varying or not) will thus decrease to the POI at late times. Since the linearization constant changes as the simulation progresses it is of interested to examine the impact on the spectral radius. The figure below plots the spectral radius for each of the fission multiplicities as a function of the linearization constant used. Numerical values are also added to the plot. The numerical curves were generated by taking a very large slab size (to approximate an infinite system) and then adjusting the linearization constant initially used over the first timestep (instead of using 2, any desired value may be inserted).

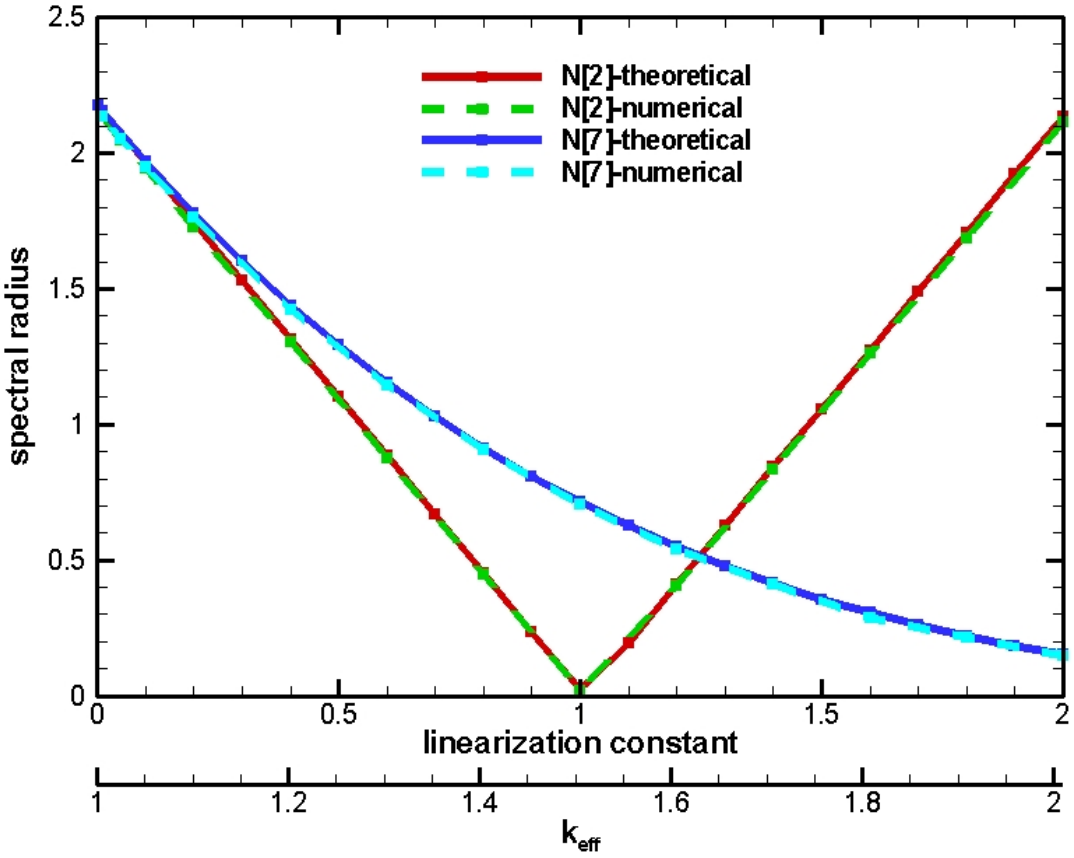

Figure 49: Spectral radius for different multiplicities and linearization constants with a large timestep.

Two sets of curves are provided: one set for the quadratic truncation and the other for the full multiplicity. Two sets of abscissa are shown. The upper axis describes the constant for which the non-linear terms are linearized about. The lower axis shows the linearization constant for the SS POI as a function of the system multiplication factor. This axis is included to highlight what the final POI value (or linearization constant) would be for a given multiplication factor. The figure indicates that the numerical results agree well with the theoretical results across all system multiplication factors. Numerically the simulation begins by setting the linearization constant to 2. The spectral radii at this value match those shown in Figure 48. As the POI is approached, the

spectral radius is found to increase for both multiplicities. This becomes problematic for the systems of interest to this work. As noted by the lower abscissa, systems with multiplication factors near unity have small corresponding POIs which thus result in a large spectral radius. For all the cases where the spectral radius becomes greater than unity shows that the numerical routines should not be able to converge over the first timestep. Some non convergence was previously shown for the quadratic truncation. Why these cases converge at all will be illustrated shortly.

The behavior shown in Figure 49 indicates a significant convergence problem around either the initial condition (quadratic truncation) or as the solution approaches the SS POI (all cases). As systems of interest in this work are finite in nature, there is a considerable amount of leakage from the slab. Leakage from the system will greatly reduce the spectral radius as another loss term is included in the simulation that is not present in the Fourier analysis. To better understand the connection between the theoretical and numerical spectral radius for systems of interest, these two are calculated for comparison.

By adjusting the slab thickness, different system eigenvalues were achieved. For both the quadratic and seven terms cases, the spectral radius calculated over the first timestep is shown below. The first timestep is the only timestep for which the theory is valid (constant spatial solution) as after each timestep the $N(p_0)$ and $N'(p_0)$ are updated from a spatially varying solution. Over the first timestep these terms are linearized about $p_0 = 2$ or $p_0 = p_\infty = POI$ which are flat solutions. A large timestep was used to remove the time absorption term.

Table 12: Numerical and theoretical spectral radius over the first timestep.

k_{eff}	slab thickness (cm)	2 terms		7 terms	
		$p_0 = 2$	$p_0 = p_\infty$	$p_0 = 2$	$p_0 = p_\infty$
1.001	9.3912	0.9816	0.0818	0.0696	0.1294
1.01	9.5094	0.9901	0.0825	0.0703	0.1309
1.1	10.749	1.0787	0.0899	0.0766	0.1422
1.25	13.100	1.2258	0.1022	0.0870	0.1616
1.5	18.274	1.4709	0.1226	0.1044	0.1940
1.75	26.806	1.7165	0.1431	0.1221	0.2264
2.0	48.060	1.9613	0.1635	0.1391	0.2585
2.1	77.355	2.0593	0.1714	0.1456	0.2707
2.129	100.0	2.0880	0.1736	0.1473	0.2743
2.155	150.0	2.1127	0.1755	0.1490	0.2743
2.178	∞	2.1359*	0.1781*	0.1516*	0.2816*

* Theoretical spectral radius.

For the small slab thicknesses which result in low prompt multiplication factors applicable to FBRs, the calculated numerical spectral radius is significantly lower than the theoretical value (shown in the last row). As the slab thickness was increased and the resulting slab eigenvalue approaches the infinite eigenvalue the spectral radius approaches the theoretical value. The results highlight the importance of system leakage on the problem. Leakage is such a prominent loss mechanism that the quadratic cases linearized about the initial condition only converge for marginally prompt critical systems $\left(k_{eff} < 1.1\right)$. This explains why most of the quadratic cases shown previously did not converge for the large timestep. If one is interested in ensuring that the theoretical spectral radius is always smaller than unity, a timestep control could be invoked.

Solving Eq. 119 for time, the following timestep requirement can be invoked to ensure whatever spectral radius is desired:

$$\Delta t = \frac{\dfrac{2'\left|N'_{\infty}\right|}{\rho} - \Sigma_A}{v} \tag{120}$$

There is another important point that can be addressed by the behavior seen in Figure 49. Although it was just previously mentioned that the theoretical result does not apply after subsequent timesteps, the theory can be used to provide an indication of the numerical behavior seen after multiple timesteps. In particular, regardless of the initial linearization constant used, the spatially dependent solution always tends to the SS POI appropriate for the system of interest. It has been shown throughout this work that weak prompt critical systems typically have small values for the POI, roughly $10^{-2} - 10^{-3}$. The curves in Figure 49 show that as the POI value is approached, the spectral radius grows. This indicates that as the POI value is approached, numerical convergence becomes more taxing; in particular for systems with small multiplication factors.

This behavior, where the spectral radius increases, was also found numerically. To highlight this, a case is presented below for the full multiplicity, $k_{eff} = 1.001$, linearized about $p_0 = 2$ for a large timestep. The columns show the simulation timestep, the number of outers in each timestep, the spectral radius over the timestep, and the non-

extinction probability at the slab edge and midpoint. The data shown in the table matches that of the $k_{eff} = 1.001$ case shown in Figure 46.

Table 13: Spectral radius for multiple timesteps.

timestep	outer iterations	spectral radius	$p_0(L/2)/2$	$p_0(L)/2$
1	10	0.0697	0.399933	0.184630
2	29	0.4644	0.185793	0.075090
3	61	0.7181	0.089599	0.035488
4	119	0.8557	0.044191	0.017458
5	224	0.9271	0.022168	0.008755
6	414	0.9633	0.011327	0.004473
7	755	0.9816	0.005955	0.002351
8	1357	0.9908	0.003294	0.001301
9	2385	0.9953	0.001997	0.000789
10	3979	0.9976	0.001405	0.000555
11	5725	0.9986	0.001194	0.000472
12	5753	0.9989	0.001158	0.000457
13	2656	0.9991	0.001157	0.000457
14	11	0.9995	0.001157	0.000457
15	1	-	0.001157	0.000457

Initially the spectral radius is small, which is in agreement with Figure 49 for the seven terms case. As the simulation progresses and the non-extinction probability approaches the SS POI for this system, the outer iteration count significantly increases. This is borne out by the increase in the spectral radius. As was indicated in Figure 49, the spectral radius continues to grow as the POI is approached. Although the theoretical spectral radius at the POI is greater than one, system leakage is the means by which the simulation is able to converge. It is worthwhile to note that for all the cases of interest in this work, no cases were found in which the numerical spectral radius exceeded one as the non-extinction probability approaches the POI for the full multiplicity. The fact that this was observed was merely a matter of chance. As shown in the table above, the

spectral radius is near unity, but it was always less than unity. Although thicker systems with less leakage should have higher spectral radii, the non-extinction probability for these systems is also larger in magnitude. To reiterate what was found numerically, all the combinations of non-extinction probabilities and leakage rates resulted in systems which always converged with the exception of the quadratic case with a large timestep.

8.5 Accelerated Linearized Lagged Fission Source Routine

It was shown above that the spectral radius was defined by the $\omega = 0$ wave number. To try to reduce this mode an acceleration scheme was sought which would dampen the $\omega = 0$ mode without affecting the convergence of the other modes. In other words, one seeks to improve the numerical performance by reducing the importance of the zero'th mode without inadvertently causing one of the other modes to become more dominant and larger than the un-accelerated case. The $\omega = 0$ mode is the flat spatial mode which corresponds to an infinitely long wavelength and suggests that a diffusive estimate of the error may improve the performance. It is known that this offending mode is also found when solving the neutron transport equation (Adams 2002). The time absorption term, can become problematic when very large timesteps are taken since taking an "infinite" timestep results in the worst case spectral radius. When small timesteps are used, the spectral radius decreases significantly in magnitude due to time absorption. It can be shown that by shrinking the simulation timestep to a sufficiently small value that the spectral radius can always be reduced to below unity.

Beyond the iteration techniques described previously, there exists a large class of acceleration techniques commonly employed when solving the neutron transport equation. One method that is widely used is that of diffusion synthetic acceleration. DSA is commonly used not because the solution depends on diffusion theory being a good approximation to transport theory; rather it only makes use of the diffusion solution as an error corrector. Acceleration is performed on the outer iterations by applying an error corrector calculated from a modified diffusion update. Multiple authors have investigated using DSA for solving the standard transport equation. For complete details, the reader is guided to works provided by Alcouffe 1977, Larsen 1982, and Adams 2002.

During the development of this work, it became clear that the performance of the outer iterations could be improved. An accelerated routine was formulated to increase the rate at which the outer iterations would reach the specified convergence criteria. The acceleration scheme on the outer iteration is outlined as follows. The outer iteration shown previously is modified such that the index is shifted:

$$\mu \cdot \frac{\partial p^{(l+1/2)}(x,\mu)}{\partial x} + \left(\Sigma_T + \frac{1}{v \cdot \Delta t} \right) \cdot p^{(l+1/2)}(x,\mu) = \frac{\Sigma_S}{2} \cdot p_0{}^{(l+1/2)}(x) + N'_{\infty} \cdot p_0{}^{(l)}(x) + Q(x,\mu) \tag{121}$$

A half index is used to denote that the error update occurs after the converged inner solution. Define the error as the difference of the iteration equation from the exact equation:

$$\varepsilon^{(l+1/2)}(x,\mu) = p(x,\mu) - p^{(l+1/2)}(x,\mu) \text{ and } \varepsilon_0^{(l+1/2)}(x) = p_0(x) - p_0^{(l+1/2)}(x) \tag{122}$$

Subtracting the iteration equation from the exact equation yields:

$$\mu \cdot \frac{\partial \varepsilon^{(l+1/2)}(x,\mu)}{\partial x} + \left(\Sigma_T + \frac{1}{v \cdot \Delta t}\right) \cdot \varepsilon^{(l+1/2)}(x,\mu) = \frac{\Sigma_S}{2} \cdot \varepsilon_0{}^{(l+1/2)}(x) + N'_\infty \cdot \left(p_0(x) - p_0{}^{(l)}(x)\right) \tag{123}$$

The bracketed difference in the second term on the right hand side can be rewritten as:

$$p_0(x) - p_0{}^{(l)}(x) = p_0(x) - p_0{}^{(l+1/2)}(x) + p_0{}^{(l+1/2)}(x) - p_0{}^{(l)}(x) = \varepsilon_0{}^{(l+1/2)}(x) + \left(p_0{}^{(l+1/2)}(x) - p_0{}^{(l)}(x)\right) \tag{124}$$

Plugging this into the error equation:

$$\mu \cdot \frac{\partial \varepsilon^{(l+1/2)}(x,\mu)}{\partial x} + \left(\Sigma_T + \frac{1}{v \cdot \Delta t}\right) \cdot \varepsilon^{(l+1/2)}(x,\mu) = \frac{\Sigma_S}{2} \cdot \varepsilon_0{}^{(l+1/2)}(x) + N'_\infty \cdot \left[\varepsilon_0{}^{(l+1/2)}(x) + \left(p_0{}^{(l+1/2)}(x) - p_0{}^{(l)}(x)\right)\right] \tag{125}$$

For simplification, let R_o represent a residual such that:

$$R_o(x) = N'_\infty \cdot \left(p_0{}^{(l+1/2)}(x) - p_0{}^{(l)}(x)\right) \tag{126}$$

The error equation then becomes:

$$\mu \cdot \frac{\partial \varepsilon^{(l+1/2)}(x,\mu)}{\partial x} + \left(\Sigma_T + \frac{1}{v \cdot \Delta t}\right) \cdot \varepsilon^{(l+1/2)}(x,\mu) = \left(\frac{\Sigma_S}{2} + N'_\infty\right) \cdot \varepsilon_0{}^{(l+1/2)}(x) + R_o(x) \tag{127}$$

Upon solution of the above equation for $\varepsilon^{(l+1/2)}(x,\mu)$ an update to the original outer iteration can be obtained from: $p_0^{(l+1)} = p_0^{(l)} + \varepsilon_0^{(l+1/2)}$ where $p_0^{(l)}$ is the solution from the converged inner iteration and $\varepsilon_0^{(l+1/2)}$ is the solution from the error update.

Given that solution of the error equation is just as complicated as the original outer iteration equation, a low order diffusive approximation is used for the error update.

To define this new equation, the error equation is integrated over the angular domain [-1,1] to obtain to obtain the first moment:

$$\frac{d\varepsilon_1^{(l+1/2)}(x)}{dx} + \left(\Sigma_T + \frac{1}{v\cdot\Delta t}\right)\cdot\varepsilon_0^{(l+1/2)}(x) = \left(\Sigma_S + 2\cdot N'_\infty\right)\cdot\varepsilon_0{}^{(l+1/2)}(x) + 2\cdot R_o(x) \tag{128}$$

where $\varepsilon_1^{(l+1/2)}(x) = \int_{-1}^{1}\mu\cdot\varepsilon^{(l+1/2)}(x,\mu)\cdot d\mu$ or (129)

$$\frac{d\varepsilon_1^{(l+1/2)}(x)}{dx} + \left(\Sigma_A + \frac{1}{v\cdot\Delta t}\right)\cdot\varepsilon_0^{(l+1/2)}(x) = 2\cdot N'_\infty\cdot\varepsilon_0{}^{(l+1/2)}(x) + 2\cdot R_o(x) \tag{130}$$

Integrating the error equation over the angular domain once again to obtain the second moment:

$$\frac{d\varepsilon_2^{(l+1/2)}(x)}{dx} + \Sigma_T \cdot \varepsilon_1^{(l+1/2)}(x) = 0 \tag{131}$$

where $\varepsilon_2^{(l+1/2)}(x) = \int_{-1}^{1} \mu \cdot \varepsilon_1^{(l+1/2)} \cdot d\mu$. Since the error equation is isotropic, a diffusion ansatz is introduced:

$$\varepsilon^{(l+1/2)}(x,\mu) = \frac{1}{2} \cdot \varepsilon_0^{(l+1/2)}(x) + \frac{3}{2} \cdot \mu \cdot \varepsilon_1^{(l+1/2)}(x) \tag{132}$$

Inserting this expression into the angular integrated equation yields:

$$\frac{d}{dx}\left[\frac{1}{3} \cdot \varepsilon_0^{(l+1/2)}(x)\right] + \left(\Sigma_T + \frac{1}{v \cdot \Delta t}\right) \cdot \varepsilon_1^{(l+1/2)}(x) = 0 \tag{133}$$

or

$$\varepsilon_1^{(l+1/2)}(x) = -\frac{1}{3 \cdot \left(\Sigma_T + \frac{1}{v \cdot \Delta t}\right)} \cdot \frac{d}{dx}\left[\varepsilon_0^{(l+1/2)}(x)\right] \tag{134}$$

The low order approximation for the error can thus be found through solution of:

$$-\frac{d}{dx}\left[D\cdot\frac{d\varepsilon_0^{(l+1/2)}(x)}{dx}\right]+\left(\Sigma_A+\frac{1}{v\cdot\Delta t}\right)\cdot\varepsilon_0^{(l+1/2)}(x)=2\cdot N'_{\infty}\cdot\varepsilon_0^{(l+1/2)}(x)+2R_o \tag{135}$$

where $D=\dfrac{1}{3\cdot\left(\Sigma_T+\dfrac{1}{v\cdot\Delta t}\right)}$

The consistent discretization with the cell averaged diamond difference non-extinction probability is provided below for the low order diffusion update utilizing Marshek boundary conditions:

The error update on the slab edges:

For the i = 1 cell:

$$\begin{aligned}&\left(\frac{2}{3\cdot\left(\Sigma_T+\dfrac{1}{v\cdot\Delta t}\right)\cdot\Delta x}+\frac{\left(\Sigma_A+\dfrac{1}{v\cdot\Delta t}-2\cdot N'_{\infty}\right)\cdot\Delta x}{2}+\alpha\right)\cdot\varepsilon_{0,1/2}+\\&\left(-\frac{2}{3\cdot\left(\Sigma_T+\dfrac{1}{v\cdot\Delta t}\right)\cdot\Delta x}+\frac{\left(\Sigma_A+\dfrac{1}{v\cdot\Delta t}-2\cdot N'_{\infty}\right)\cdot\Delta x}{2}\right)\cdot\varepsilon_{0,3/2}=\Delta x\cdot R_{0,1}\end{aligned} \tag{136}$$

where $\alpha=\dfrac{2}{3}\cdot\dfrac{\sum_{m=1}^{S_N/2}\mu_m\cdot w_m}{\sum_{m=1}^{S_N/2}\mu_m^2\cdot w_m}\approx 1$ which is evaluated for $\mu>0$.

For the i = I cell

$$\left(-\frac{2}{3\cdot\left(\Sigma_T+\frac{1}{v\cdot\Delta t}\right)\cdot\Delta x}+\frac{\left(\Sigma_A+\frac{1}{v\cdot\Delta t}-2\cdot N'_{\infty}\right)\cdot\Delta x}{2}\right)\cdot\varepsilon_{0,I-1/2}+$$
$$\left(\frac{2}{3\cdot\left(\Sigma_T+\frac{1}{v\cdot\Delta t}\right)\cdot\Delta x}+\frac{\left(\Sigma_A+\frac{1}{v\cdot\Delta t}-2\cdot N'_{\infty}\right)\cdot\Delta x}{2}+\alpha\right)\cdot\varepsilon_{0,I+1/2}=\Delta x\cdot R_{0,I} \tag{137}$$

The error update on the slab interior is:

$$\left(-\frac{2}{3\cdot\left(\Sigma_T+\frac{1}{v\cdot\Delta t}\right)\cdot\Delta x}+\frac{\left(\Sigma_A+\frac{1}{v\cdot\Delta t}-2\cdot N'_{\infty}\right)\cdot\Delta x}{2}\right)\cdot\varepsilon_{0,i-1/2}+$$
$$\left(\frac{4}{3\cdot\left(\Sigma_T+\frac{1}{v\cdot\Delta t}\right)\cdot\Delta x}+\left(\Sigma_A+\frac{1}{v\cdot\Delta t}-2\cdot N'_{\infty}\right)\cdot\Delta x\right)\cdot\varepsilon_{0,i+1/2}+ \tag{138}$$
$$\left(-\frac{2}{3\cdot\left(\Sigma_T+\frac{1}{v\cdot\Delta t}\right)\cdot\Delta x}+\frac{\left(\Sigma_A+\frac{1}{v\cdot\Delta t}-2\cdot N'_{\infty}\right)\cdot\Delta x}{2}\right)\cdot\varepsilon_{0,i+3/2}=\Delta x\cdot\left(R_{0,i}+R_{0,i+1}\right)$$

When written in matrix format, the resulting matrix is tridiagonal. A standard tridiagonal matrix solver is invoked to solve the error update at the slab edges.

$$\begin{bmatrix} A & B & 0 & 0 & \dots & 0 \\ B & C & B & 0 & \dots & 0 \\ \dots & B & C & B & \dots & 0 \\ \dots & \dots & \dots & \dots & \dots & \dots \\ 0 & \dots & 0 & B & C & B \\ 0 & \dots & 0 & 0 & B & A \end{bmatrix} \cdot \begin{bmatrix} \varepsilon_{0,1/2} \\ \varepsilon_{0,3/2} \\ \varepsilon_{0,5/2} \\ \vdots \\ \varepsilon_{0,I-1/2} \\ \varepsilon_{0,I+1/2} \end{bmatrix} = 2 \cdot \Delta x \cdot \begin{bmatrix} N'_{\infty,1} \cdot \left(p_{0,1}^{l+1/2} - p_{0,1}^{l} \right) \\ N'_{\infty,2} \cdot \left(p_{0,2}^{l+1/2} - p_{0,2}^{l} \right) + N'_{\infty,1} \cdot \left(p_{0,1}^{l+1/2} - p_{0,1}^{l} \right) \\ N'_{\infty,3} \cdot \left(p_{0,3}^{l+1/2} - p_{0,3}^{l} \right) + N'_{\infty,2} \cdot \left(p_{0,2}^{l+1/2} - p_{0,2}^{l} \right) \\ \vdots \\ N'_{\infty,I} \cdot \left(p_{0,I}^{l+1/2} - p_{0,I}^{l} \right) + N'_{\infty,I-1} \cdot \left(p_{0,I-1}^{l+1/2} - p_{0,I-1}^{l} \right) \\ N'_{\infty,I} \cdot \left(p_{0,I}^{l+1/2} - p_{0,I}^{l} \right) \end{bmatrix}$$

where:

$$A = \left[\frac{2}{3 \cdot \left(\Sigma_T + \dfrac{1}{v \cdot \Delta t} \right) \cdot \Delta x} + \frac{\left(\Sigma_A + \dfrac{1}{v \cdot \Delta t} - 2 \cdot N'_{\infty} \right) \cdot \Delta x}{2} + \alpha \right] \tag{139}$$

$$B = \left[-\frac{2}{3 \cdot \left(\Sigma_T + \dfrac{1}{v \cdot \Delta t} \right) \cdot \Delta x} + \frac{\left(\Sigma_A + \dfrac{1}{v \cdot \Delta t} - 2 \cdot N'_{\infty} \right) \cdot \Delta x}{2} \right] \tag{140}$$

$$C = \left[\frac{4}{3 \cdot \left(\Sigma_T + \dfrac{1}{v \cdot \Delta t} \right) \cdot \Delta x} + \left(\Sigma_A + \frac{1}{v \cdot \Delta t} - 2 \cdot N'_{\infty} \right) \cdot \Delta x \right] \tag{141}$$

Solution of $\varepsilon_0^{l+1/2}$ provides the error update with each term being defined at the cell edges. In order to convert from cell edge to cell averages the diamond closure relationship was used where $\varepsilon_{0,i}^{l+1/2} = \frac{1}{2} \cdot \left(\varepsilon_{0,i-1/2}^{l+1/2} + \varepsilon_{0,i+1/2}^{l+1/2} \right)$. Upon evaluation of the cell average error, an update to the angular integrated probability values was performed. The

updated $p_{0,j}^{l+1}$ was then used in the next outer iteration (assuming convergence was not obtained) for calculating $N'_{\infty,j} \cdot p_{0,j}^{(l)}$.

8.5.1 Spectral Radius – Accelerated Linearized Routine

To examine the performance of the diffusion acceleration scheme, a Fourier analysis was also performed. The following are the equations of interest for the analysis:

1. Non-extinction probability outer iteration from Eq. 121:

$$\mu \cdot \frac{\partial p^{(l+1/2)}(x,\mu)}{\partial x} + \left(\Sigma_T + \frac{1}{v \cdot \Delta t}\right) \cdot p^{(l+1/2)}(x,\mu) = \frac{\Sigma_S}{2} \cdot p_0{}^{(l+1/2)}(x) + N'_{\infty} \cdot p_0{}^{(l)}(x) + Q(x,\mu) \tag{142}$$

2. Diffusion low order error approximation from Eq. 135:

$$-D \cdot \frac{d^2 \varepsilon_0^{(l+1/2)}(x)}{dx^2} + \left(\left(\Sigma_A + \frac{1}{v \cdot \Delta t}\right) - 2 \cdot N'_{\infty}\right) \cdot \varepsilon_0^{(l+1/2)}(x) = 2 \cdot N'_{\infty} \cdot \left(p_0{}^{(l+1/2)}(x) - p_0{}^{(l)}(x)\right) \tag{143}$$

3. Update equation:

$$p_0^{(l+1)}(x) = p_0^{(l+1/2)}(x) + \varepsilon_0^{(l+1/2)}(x) \tag{144}$$

Introduce the following:

$$p^{(l+1/2)}(x,\mu) = A^{(l+1/2)}(\mu)\cdot e^{i\omega x} \tag{145}$$

$$p_0^{(l)}(x) = A_0^{(l)}\cdot e^{i\omega x} \tag{146}$$

$$\varepsilon_0^{(l+1/2)}(x) = E_0^{(l+1/2)}\cdot e^{i\omega x} \tag{147}$$

Insert these into the outer iteration equation to yield:

$$\begin{aligned} &i\omega\cdot\mu\cdot A^{(l+1/2)}(\mu)\cdot e^{i\omega x} + \left(\Sigma_T + \frac{1}{v\cdot\Delta t}\right)\cdot A^{(l+1/2)}(\mu)\cdot e^{i\omega x} = \\ &\frac{\Sigma_S}{2}\cdot A_0^{(l+1/2)}\cdot e^{i\omega x} + N'_{\infty}\cdot A_0^{(l)}\cdot e^{i\omega x} \end{aligned} \tag{148}$$

Again assuming the linear independence of each of the ω modes such that:

$$\left(i\omega\cdot\mu + \left(\Sigma_T + \frac{1}{v\cdot\Delta t}\right)\right)\cdot A^{(l+1/2)}(\mu) = \frac{\Sigma_S}{2}\cdot A_0^{(l+1/2)} + N'_{\infty}\cdot A_0^{(l)} \tag{149}$$

Rearranging:

$$A^{(l+1/2)}(\mu) = \frac{\Sigma_S}{2}\cdot\frac{1}{i\omega\cdot\mu + \left(\Sigma_T + \frac{1}{v\cdot\Delta t}\right)}\cdot A_0^{(l+1/2)} + \frac{N'_{\infty}}{i\omega\cdot\mu + \left(\Sigma_T + \frac{1}{v\cdot\Delta t}\right)}\cdot A_0^{(l)} \tag{150}$$

Integrating this equation over the angular domain [-1,1]

$$A_0^{(l+1/2)} = \frac{\Sigma_S}{2\cdot i\omega}\cdot \ln\left(\frac{i\omega+\left(\Sigma_T+\frac{1}{v\cdot\Delta t}\right)}{-i\omega+\left(\Sigma_T+\frac{1}{v\cdot\Delta t}\right)}\right)\cdot A_0^{(l+1/2)} + \frac{N'_\infty}{i\omega}\cdot \ln\left(\frac{i\omega+\left(\Sigma_T+\frac{1}{v\cdot\Delta t}\right)}{-i\omega+\left(\Sigma_T+\frac{1}{v\cdot\Delta t}\right)}\right)\cdot A_0^{(l)} \tag{151}$$

Rearranging:

$$A_0^{(l+1/2)}\cdot\left[1-\frac{\Sigma_S}{2\cdot i\omega}\cdot \ln\left(\frac{i\omega+\left(\Sigma_T+\frac{1}{v\cdot\Delta t}\right)}{-i\omega+\left(\Sigma_T+\frac{1}{v\cdot\Delta t}\right)}\right)\right] = \frac{N'_\infty}{i\omega}\cdot \ln\left(\frac{i\omega+\left(\Sigma_T+\frac{1}{v\cdot\Delta t}\right)}{-i\omega+\left(\Sigma_T+\frac{1}{v\cdot\Delta t}\right)}\right)\cdot A_0^{(l)} \tag{152}$$

or

$$A_0^{(l+1/2)} = \frac{\frac{N'_\infty}{i\omega}\cdot \ln\left(\frac{i\omega+\Sigma_T}{-i\omega+\Sigma_T}\right)}{\left[1-\frac{\Sigma_S}{2\cdot i\omega}\cdot \ln\left(\frac{i\omega+\Sigma_T}{-i\omega+\Sigma_T}\right)\right]}\cdot A_0^{(l)} = \gamma(\omega)\cdot A_0^{(l)} \tag{153}$$

Note that $\gamma(\omega)$ is the same as that shown in the previous Fourier analysis. Repeating the process for the low order diffusion equation yields:

$$-D\cdot(i\omega)^2\cdot E_0^{(l+1/2)}\cdot e^{i\omega x}+\left(\left(\Sigma_A+\frac{1}{v\cdot\Delta t}\right)-2\cdot N'_{\infty}\right)\cdot E_0^{(l+1/2)}\cdot e^{i\omega x}= \\ 2\cdot N'_{\infty}\cdot e^{i\omega x}\cdot\left(A_0{}^{(l+1/2)}-A_0{}^{(l)}\right) \tag{154}$$

which simplifies to:

$$\left(D\cdot\omega^2+\left(\Sigma_A+\frac{1}{v\cdot\Delta t}\right)-2\cdot N'_{\infty}\right)\cdot E_0^{(l+1/2)}=2\cdot N'_{\infty}\cdot\left(A_0{}^{(l+1/2)}-A_0{}^{(l)}\right) \tag{155}$$

Using the equation above, $A_0^{(l+1/2)}$ can be eliminated, yielding:

$$E_0^{(l+1/2)}=\frac{2\cdot N'_{\infty}\cdot[\gamma(\omega)-1]}{\left(D\cdot\omega^2+\left(\Sigma_A+\frac{1}{v\cdot\Delta t}\right)-2\cdot N'_{\infty}\right)}\cdot A_0{}^{(l)} \tag{156}$$

The solutions from the two equations can be combined through:

$$A_0^{(l+1)}=A_0^{(l+1/2)}+E_0^{(l+1/2)} \tag{157}$$

Performing the combination yields:

$$A_0^{(l+1)}=\left[2\cdot N'_{\infty}\cdot\left(\frac{\gamma(\omega)-1}{D\cdot\omega^2+\left(\Sigma_A+\frac{1}{v\cdot\Delta t}\right)-2N'_{\infty}}\right)+\gamma(\omega)\right]\cdot A_0^{(l)}\equiv\Gamma(\omega)\cdot A_0^{(l)} \tag{158}$$

The spectral radius for the accelerated scheme is then defined from:

$$\rho = \max_{\omega} |\Gamma(\omega)| \tag{159}$$

As was noted for the unaccelerated case, to ensure conditional convergence it was necessary to show that $\max_{\omega} |\Gamma(\omega)| < 1$ for all ω. The figure below plots the dispersion functions, $\Gamma(\omega)$ and repeats $\gamma(\omega)$, as a function of the wave number for parameters of interest.

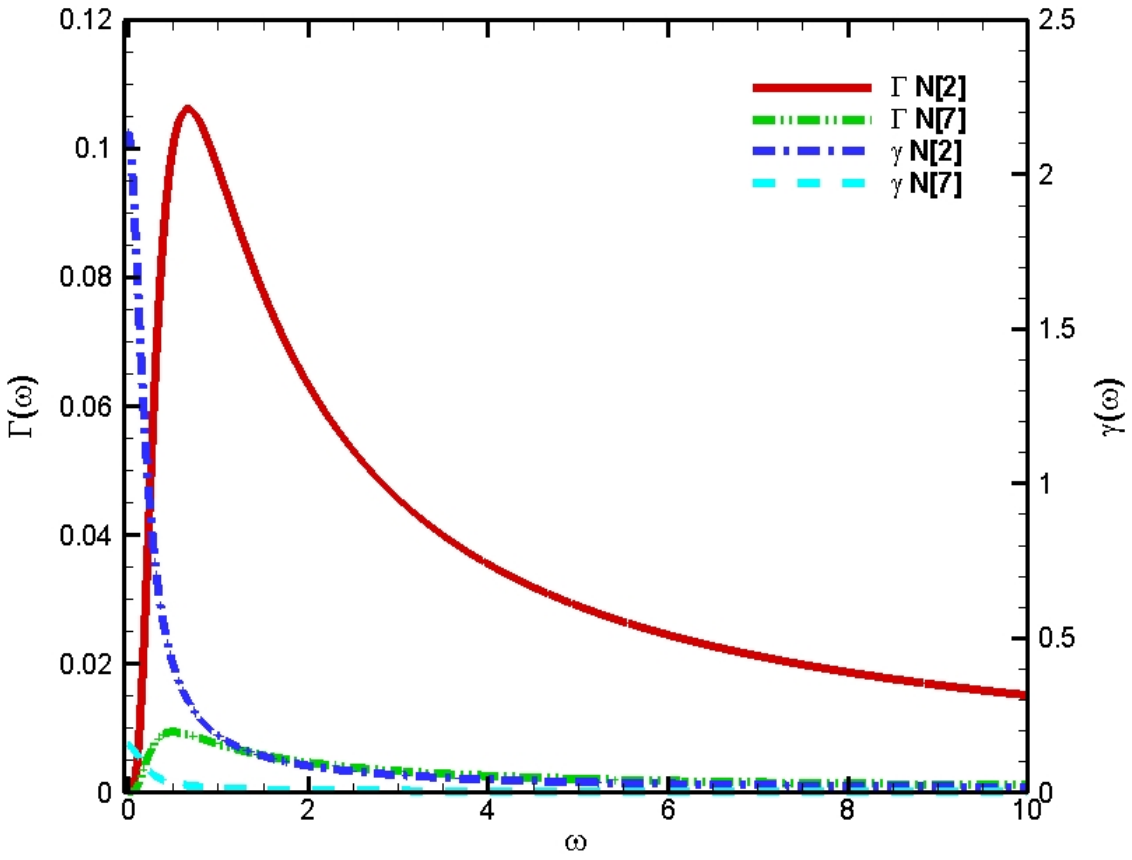

Figure 50: Dispersion functions versus wave number for the accelerated scheme linearizing about $p_0 = 2$.

For both the quadratic and full multiplicity, it is noted that the amplitude of the $\omega = 0$ error mode is zero in the accelerated case and the corresponding spectral radius is small. The acceleration scheme has eliminated the offending mode without deleteriously affecting the convergence of the other modes. For the unaccelerated cases the largest iteration amplitude for the quadratic multiplicity was ~2.135, while the accelerated scheme shows the largest amplitude is 0.1061 for the quadratic and 0.0093 for the seven terms. The accelerated scheme shifts the spectral radius to a slightly greater wave number, yet there is a remarkable decrease in the iteration amplitude. The acceleration effectively suppresses the error modes corresponding to strong angular and spatial dependence (as seen in the unaccelerated case above) and modes that have weak angular and spatial dependence (where the unaccelerated case struggled). Thus the acceleration should significantly improve the iteration performance.

8.5.2 Reflected Spectral Radius – Accelerated and Unaccelerated

As a means to ensure that the acceleration was working properly, a simplistic case was evaluated where reflective boundary conditions were put on the slab edge. For this case the system eigenvalue becomes identical to the infinite eigenvalue. To develop systems with a wide class of eigenvalues, the capture density was increased to lower the infinite medium eigenvalue. Results are presented below for the quadratic truncation when linearizing about the initial condition and the POI.

Table 14: Comparison of accelerated vs. unaccelerated results for reflecting boundary conditions when linearizing about $p_0 = 2$.

k_∞	Unaccelerated			Accelerated		
	outers	theoretical ρ	numerical ρ	outers	theoretical ρ	numerical ρ
1.001	733	0.9816	0.9816	2	0.1070	-
1.01	1346	0.9905	0.9905	2	0.1078	-
1.10	dnf	1.0787	1.0787	2	0.1155	-
1.25	dnf	1.2258	1.2258	2	0.1265	-
1.50	dnf	1.4710	1.4709	2	0.1414	-
1.75	dnf	1.7162	1.7161	2	0.1529	-
2.00	dnf	1.9613	1.9613	3	0.1620	0.1134
2.10	dnf	2.0594	2.0594	3	0.1652	0.1159

Table 15: Comparison of accelerated vs. unaccelerated results for reflecting boundary conditions when linearizing about $p_0 = p_\infty$.

k_∞	Unaccelerated			Accelerated		
	outers	theoretical ρ	numerical ρ	outers	theoretical ρ	numerical ρ
1.001	11658	0.9990	0.9990	2	0.1095	-
1.01	1390	0.9900	0.9900	2	0.1078	-
1.10	155	0.9000	0.9000	2	0.0916	-
1.25	61	0.7500	0.7500	2	0.0691	-
1.50	27	0.5000	0.5000	2	0.0399	-
1.75	14	0.2500	0.2500	3	0.0176	0.3716
2.00	3	0.0000	0.0027	3	0.0000	0.3495
2.10	8	0.1000	0.0999	3	0.0062	0.0888

With reflective boundary conditions the numerical values match the theoretical ones quite well. Numerical spectral radii are not provided for the all accelerated cases as at least three iterations are necessary for a spectral radius to be calculated. With these results in hand, as well as the plots of the dispersion function, the acceleration should be more efficient; in particular since it agreed well with the theoretical results. To examine the behavior of the acceleration with the linearization constant, the dispersion function for the acceleration was plotted against different linearization constants.

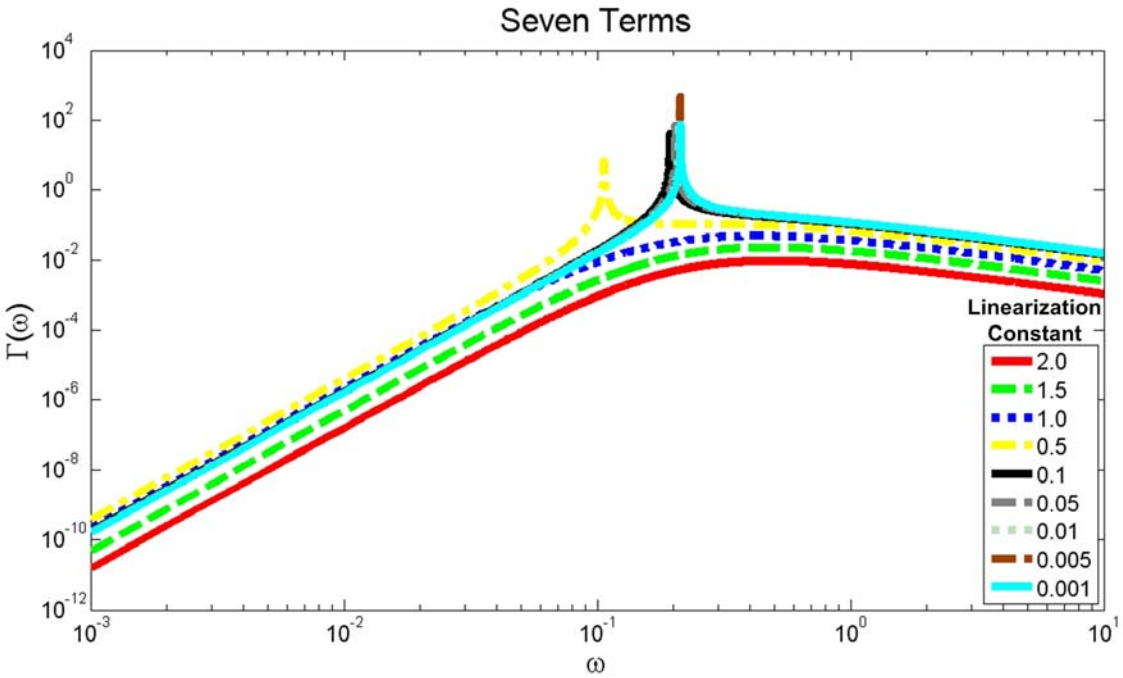

Figure 51: Iteration amplitude versus wave number for different linearization constants.

For linearization constants greater than one, the maximum value of $\Gamma(\omega)$ is always less than unity. As the linearization constant continues to decrease, it is observed that the amplitude of a mode with wave numbers very close to zero suddenly grow significantly and reduces the effectiveness of the acceleration scheme. As the linearization constant decreases, different "resonances" appear. These resonances at quite large in magnitude and also appear at different wave numbers. Thus the acceleration does an effective job at reducing the offending mode for large linearization constants, but appears to excite another mode for small linearization constants.

To highlight the regions where the resonances appear, the spectral radius was plotted against the range of linearization constants.

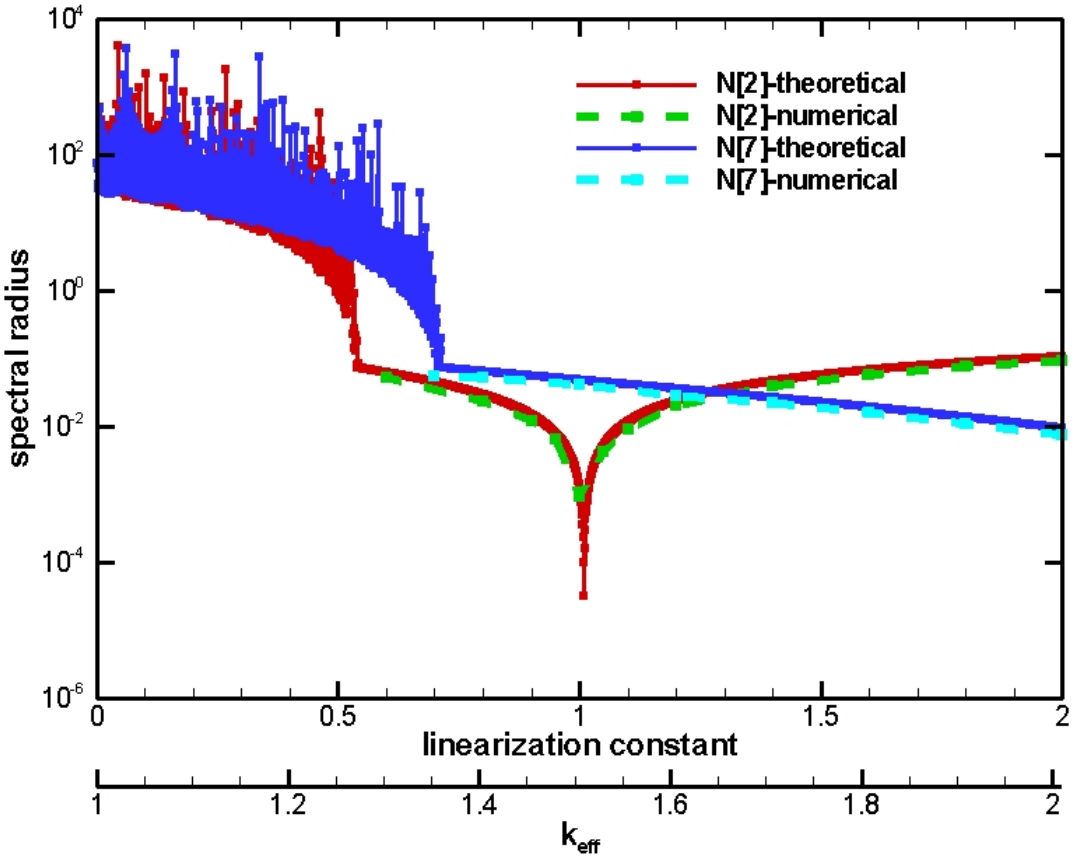

Figure 52: Spectral radius for the accelerated routine for different linearization constants.

As a function of the spectral radius, the breakdown in the acceleration can be readily seen for different linearization constants. For the range of area where the theoretical values could be compared to the numerical ones, excellent agreement was found.

To highlight where the acceleration breaks down, one must revisit the update equation Eq. 135:

$$-D\cdot\frac{d^2\varepsilon_0^{(l+1/2)}(x)}{dx^2}+\left(\left(\Sigma_A+\frac{1}{v\cdot\Delta t}\right)-2\cdot N'_{\infty}\right)\cdot\varepsilon_0^{(l+1/2)}(x)=2\cdot N'_{\infty}\cdot\left(p_0{}^{(l+1/2)}(x)-p_0{}^{(l)}(x)\right)$$

As all of the cross-sections are treated as time independent, the only parameter that is varying as a function of time is N'_{∞}. Problems can arise if the second term on the LHS becomes negative. To understand when this occurs, this term is plotted in the figure below for both a small and large timestep for the range of applicable linearization constants.

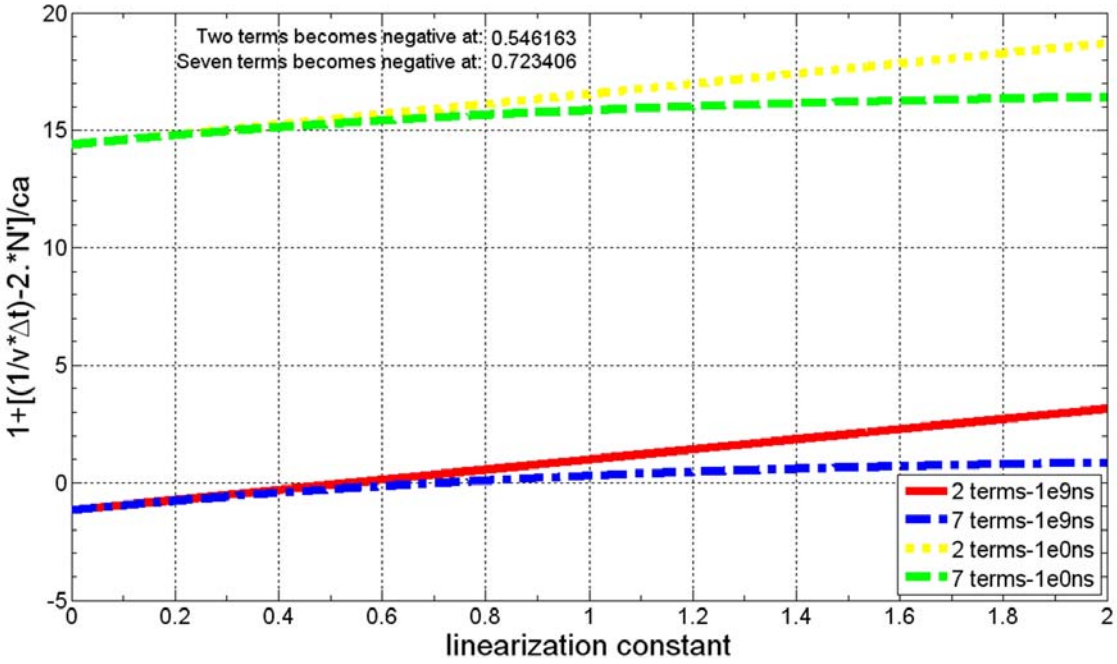

Figure 53: Diffusion update breakdown.

The two curves corresponding to a small timestep indicate that this term is always positive regardless of the linearization constant. As the timestep is increased the time absorption term approaches zero and the term becomes negative. The constants for which these cases become negative are noted in the figure. The problem with the error update can be attributed to the fact that systems of interest ultimately have small linearization constants. Since most of the cases of interest have SS POI values that are

much lower than 0.54, the breakdown in the spectral radius will be present for almost all cases.

The time absorption term was just shown to prevent the error update from breaking down. Given this, the minimum timestep required to prevent the update from breaking down can be found. The minimum timestep requirement can be invoked to prevent the term $1+\frac{\frac{1}{v\cdot\Delta t}-2\cdot N'_{\infty}}{c_A}$ from becoming negative. Rearranging the term, the timestep requirement becomes: $\Delta t < \frac{1}{v\cdot\left[2'N_{\infty}-c_A\right]}$. This expression is plotted as a function of the linearization constants for which the term was negative.

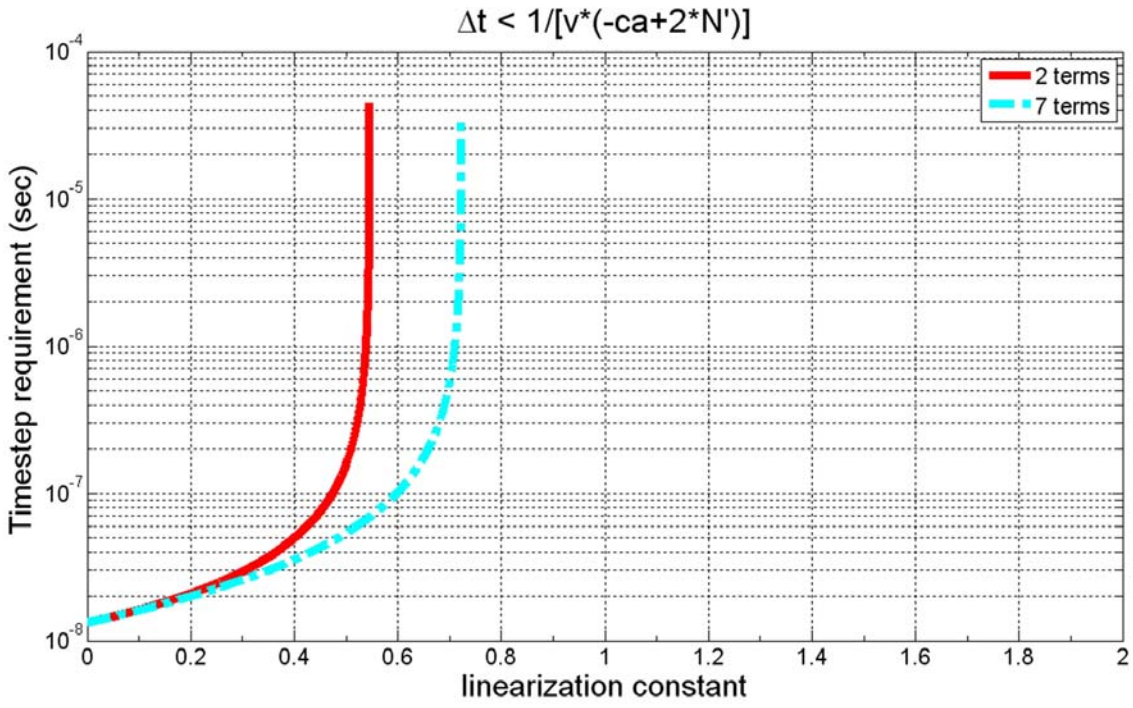

Figure 54: Timestep requirement for acceleration surety.

For large linearization constants, there is no minimum timestep required. As the linearization constant decreases, the timestep required to ensure the acceleration scheme does not breakdown decreases significantly. The slope of the curves in the above figure shows that the timestep required decreases significantly with modest decreases in the linearization constants. As the constant approaches the SS POI value, the minimum timestep approaches a value of ~13 ns. As a proof of principle, the timestep logic was built into the linearized code. As the simulation progressed forward in time, the timestep would decrease in value. Ultimately the timestep would get to such a small value ~13 ns that it was faster to simply leave the acceleration on and resort to the large timestep than to try to keep the term positive.

8.6 1-D Numerical Performance

The results presented above indicated that the spectral radius could be reduced by using an error update on the outers; however, the acceleration would eventually breakdown as the POI is reached. To illustrate the performance of the accelerated scheme against the unaccelerated case, the results presented previously are combined in a concise format for comparison.

The number of outer iterations to reach SS is shown below when first linearizing about $p_0 = 2$ and a large timestep and the full multiplicity. Small timestep cases are not included as there were only a few iterations per timestep for the unaccelerated case and acceleration was unnecessary.

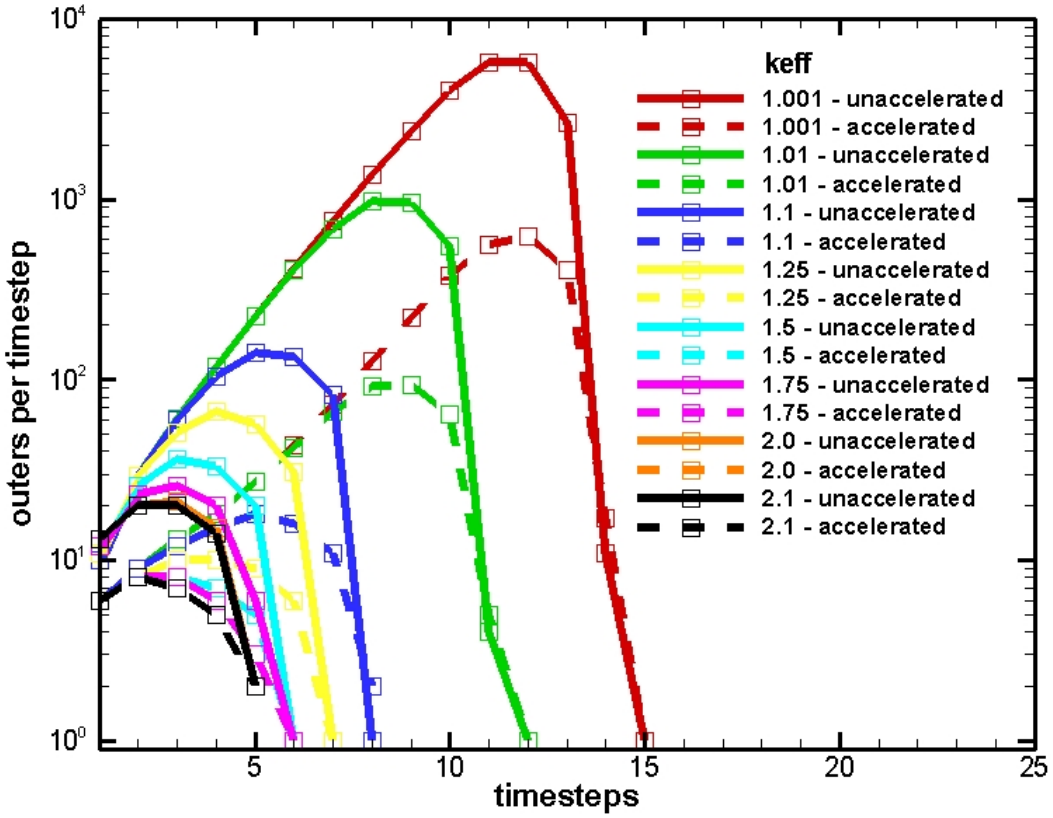

Figure 55: Combined outers to SS for accelerated and unaccelerated cases linearizing about $p_0 = 2$ with full multiplicity.

The combined plot highlights the outer iteration count for both the accelerated and unaccelerated cases. For large multiplication factors, the acceleration provides some relief; yet the overall iteration count is low. For weak prompt critical systems, both cases suffer from large iteration counts. As the iteration proceeds closer and closer to the SS POI, convergence becomes more challenging even with the acceleration turned on.

In addition to the full multiplicity plot shown above, the quadratic truncation plot is also of interest.

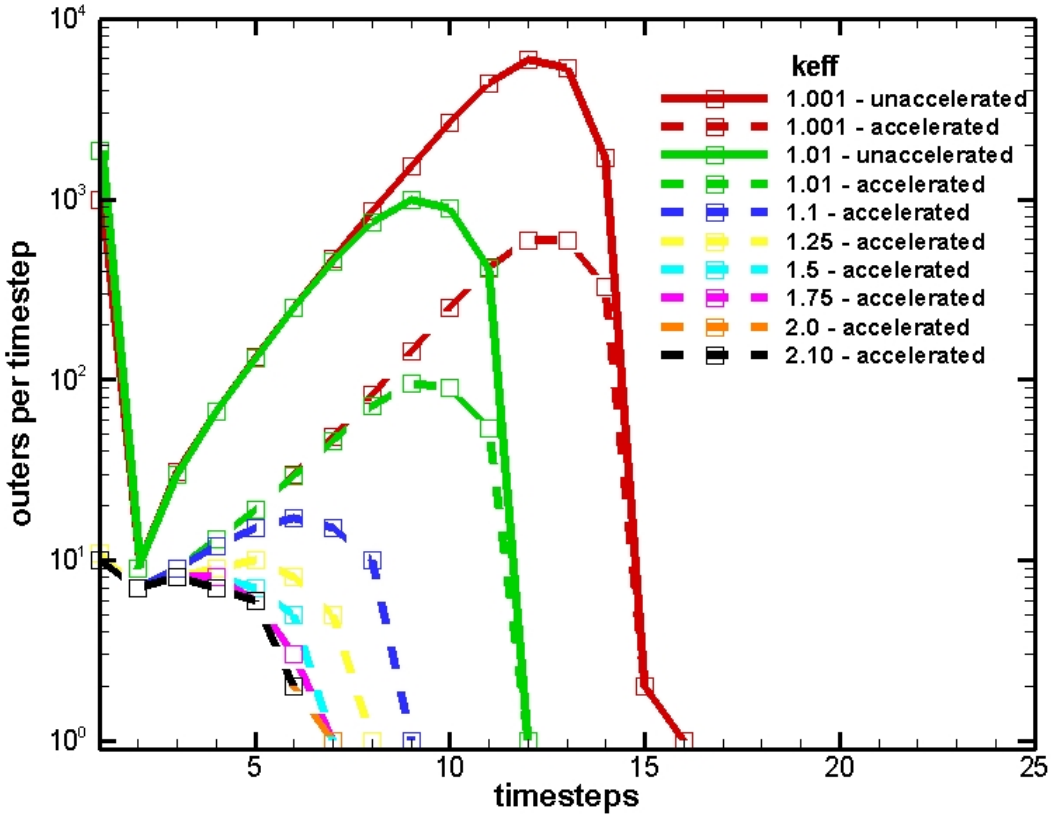

Figure 56: Combined outers to SS for accelerated and unaccelerated cases linearizing about $p_0 = 2$ with quadratic truncation.

The accelerated cases for the quadratic truncation show that the iteration count is similar to that of the full multiplicity case. Only two unaccelerated cases are shown as the spectral radius was shown previously to become greater than one for the higher multiplicity cases. For this figure, the acceleration clearly helps the initial iteration behavior allowing the higher multiplication factor cases to converge.

Cases are not presented for linearizing about the infinite medium constant as the results are quite similar to the full multiplicity case when linearizing about $p_0 = 2$. This holds

true for both the quadratic and full multiplicity cases as one would expect based on the behavior seen in the figure of the spectral radius plotted against the linearization constant.

To better understand what is numerically occurring, it is useful to show the functional shape and magnitude of the DSA error update. It is challenging to plot as there is an error update in each outer iteration and the figures above show that there are many outer iterations per timestep. To circumvent this problem, only the error update in the first outer iteration is provided for the indicated timestep using the small multiplication factor case of 1.001. The figure below plots the angular integrated spatially dependent error update profile.

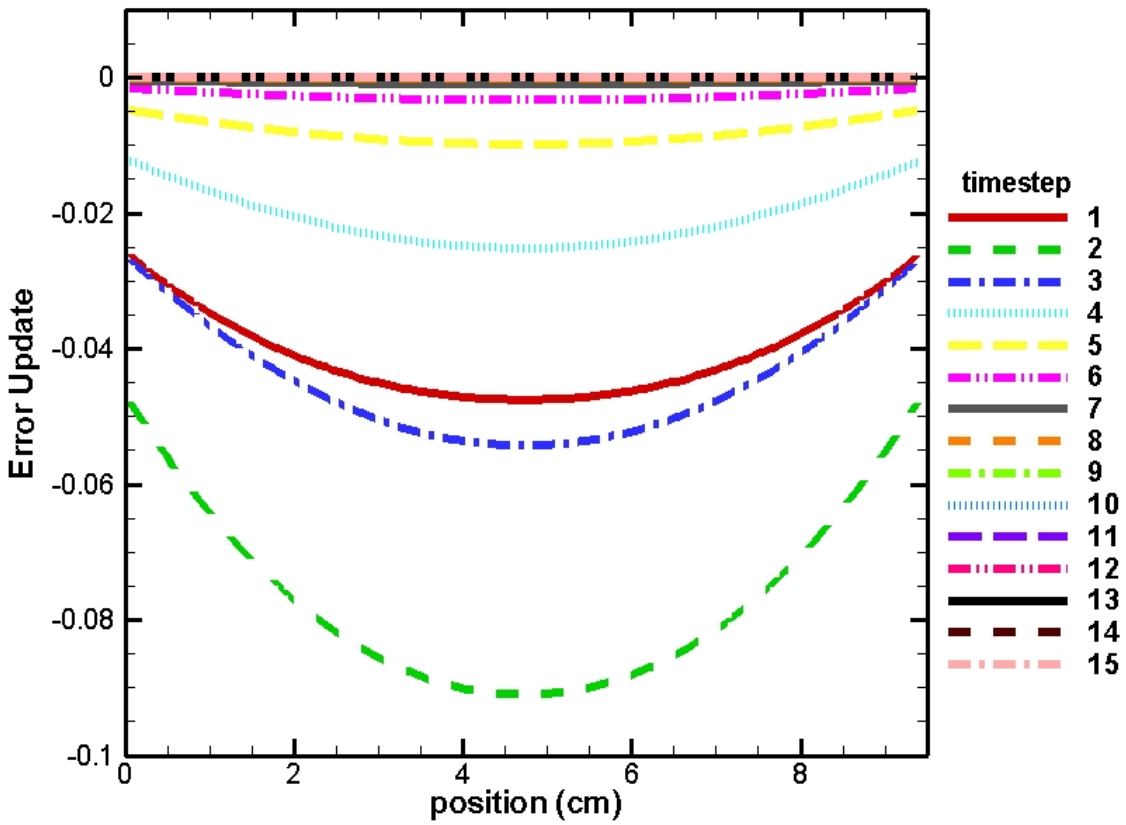

Figure 57: Error update in the first outer iteration vs. timestep.

The error updates for the large timestep case are all negative in sign for the first outer iteration and thus act to dampen the solution. After multiple timesteps, the resulting error correction becomes negligibly small. Thus the large correction seen in the first few timesteps helps explain why the error update does an effective job at accelerating the outers. After multiple timesteps the error update is small and only marginally improves the converged non-extinction probability from the inner iterations. Since the update breaks down after the first few timesteps, the error update appears to still be beneficial as the overall update is still small and negative. If the resulting update had been positive, the numerical routine would have likely lost stability.

8.7 Simulation Time

Iteration counts are useful to understand the total number of operations the computer is performing. All things being equal, the different iteration routines presented do not perform the same amount of work for each iteration. Users of transport codes are not typically interested in iteration counts; rather, interest lies in the computer run time. Due to the large difference in run times for each of the schemes shown earlier some discussion is warranted. The table below provides the computer runtime for a wide array of cases. These cases were run on a dedicated 2.4 GHz laptop with no compiler optimizations.

Table 16: Computer runtime (sec) for small timestep cases full multiplicity.

k_{eff}	Fixed Point Iteration	Lagged Routine	Linearized $p_0=2$		Linearized $p_0=p_\infty$	
			unaccel	accel	unaccel	accel
1.001	352.64	537.28	708.38	281.86	711.98	279.88
1.01	73.20	140.17	182.25	60.61	193.22	60.11
1.1	14.00	30.59	40.03	12.58	40.56	12.63
1.25	7.86	17.02	22.42	7.40	22.47	7.38
1.5	5.58	11.72	15.44	5.44	15.53	5.59
1.75	4.91	9.88	13.06	4.72	13.22	4.84
2	4.58	8.97	11.93	4.42	12.06	4.42
2.1	4.70	8.78	12.00	4.36	11.75	4.61

The unaccelerated linearized routine resulted in the poorest performance. Including the acceleration proved to be the fastest routine. Similar results are provided for the large timestep cases.

Table 17: Computer runtime (sec) for large timestep cases full multiplicity.

k_{eff}	Fixed Point Iteration	Lagged Routine	Linearized $p_0=2$		Linearized $p_0=p_\infty$	
			unaccel	accel	unaccel	accel
1.001	49.56	141.80	314.11	9.00	519.09	11.41
1.01	6.97	27.59	77.09	2.20	83.86	1.98
1.1	1.02	4.86	15.08	0.81	14.78	0.53
1.25	0.55	2.53	7.67	0.50	7.59	0.41
1.5	0.39	1.66	4.80	0.42	5.00	0.41
1.75	0.34	1.36	3.78	0.47	4.05	0.44
2	0.42	1.31	3.53	0.56	3.72	0.53
2.1	0.61	1.47	3.53	0.63	3.63	0.67

The acceleration appears to significantly reduce the computer time needed to reach SS, in particular for the low multiplication factors of interest. For large timestep cases, the error update shows its utility. In particular for the weak prompt critical systems of interest, run times decreased from many minutes to a few seconds. Despite the breakdown in the acceleration which would have rendered it even more effective, the significant decrease in run time highlights its effectiveness.

8.8 Sources of Error

Throughout the linearization analysis, there have been two sources of error. The first corresponds to the time discretization error, which is $o(\Delta t)$. The second corresponds to the linearization error. As the simulation timestep is increased, both of these error terms become more dominant. The time discretization error is more obvious and can be easily handled by implementing a higher order scheme.

The linearization error should be at its highest when the linearization is performed about the initial condition for large timesteps. Physically, the system is linearized about a value that is identical to the initial condition but far away from the SS POI. The role of the linearization error can be seen by examining the non-extinction probability between the lagged source routine (where there was no linearization) and the linearized source routine. The figure below plots all three cases for several multiplication factors, seven terms, and a large timestep.

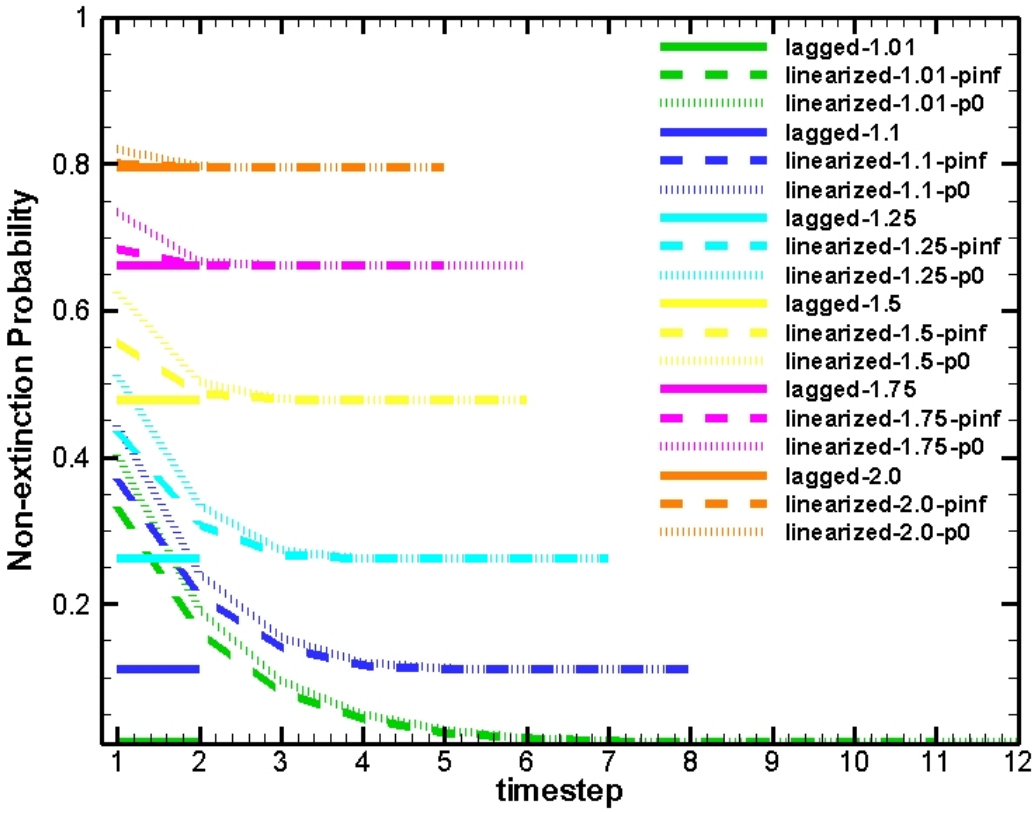

Figure 58: Non-extinction probability comparison between the linearized and lagged iteration routine.

The lagged source routine reaches SS in a few iterations. In fact, after the first iteration the SS POI is almost obtained. For the linearized routine one can see that both linearizations require multiple timesteps to reach the SS POI. The linearization about $p_0 = 2$ is the furthest from the SS POI and takes more iterations to reach the same non-extinction probability as the other cases. One can see that as the multiplication factor gets large, there is little difference between either linearization or between either iteration routine.

The results shown in the above figure indicate that the lagged routine and the linearized routine ultimately yield the same SS POI. This is only partially correct. As the linearized routine is solving a different, linear equation, the time dependent results are understandably different. The fact that the linearized routine ultimately yields values close to the SS POI highlights the capability of the routine. The table below provides results for the SS POI from the different iteration routines tried in this work.

Table 18: SS non-extinction probability from different iteration routines with a small timestep.

k_{eff}	Fixed Point Iteration	Lagged Routine	Linearized $p_0=2$		Linearized $p_0=p_\infty$	
			unaccel	accel	unaccel	accel
1.001	0.0011565	0.0011572	0.0011572	0.0011572	0.0011572	0.0011572
1.01	0.0115412	0.0115413	0.0115413	0.0115413	0.0115413	0.0115413
1.1	0.1109860	0.1109860	0.1109860	0.1109860	0.1109860	0.1109860
1.25	0.2613891	0.2613891	0.2613891	0.2613891	0.2613891	0.2613891
1.5	0.4785058	0.4785058	0.4785058	0.4785058	0.4785058	0.4785058
1.75	0.6602619	0.6602619	0.6602619	0.6602619	0.6602619	0.6602619
2	0.7956149	0.7956149	0.7956149	0.7956149	0.7956149	0.7956149
2.1	0.8216860	0.8216860	0.8216860	0.8216860	0.8216860	0.8216860

The small timestep results show that the standard source iteration and lagged iteration routine yield identical SS POI values. The linearized cases, both accelerated and unaccelerated, yield excellent agreement with the lagged routine. Results for the large timestep are also presented.

Table 19: SS non-extinction probability from different iteration routines with a large timestep.

k_{eff}	Fixed Point Iteration	Lagged Routine	Linearized p0=2		Linearized $p_0=p_\infty$	
			unaccel	accel	unaccel	accel
1.001	0.0011565	0.0011567	0.0011567	0.0011565	0.0011567	0.0011565
1.01	0.0115412	0.0115412	0.0115412	0.0115412	0.0115412	0.0115412
1.1	0.1109860	0.1109860	0.1109860	0.1109860	0.1109860	0.1109860
1.25	0.2613891	0.2613891	0.2613891	0.2613891	0.2613891	0.2613891
1.5	0.4785058	0.4785058	0.4785058	0.4785058	0.4785058	0.4785058
1.75	0.6602619	0.6602619	0.6602619	0.6602619	0.6602619	0.6602619
2	0.7956149	0.7956149	0.7956149	0.7956149	0.7956149	0.7956149
2.1	0.8216860	0.8216860	0.8216860	0.8216860	0.8216860	0.8216860

The large timestep cases also show excellent agreement between all of the cases analyzed. Thus even though the linearized cases take more timesteps to reach SS, the ability to use acceleration to speed up the simulation and to still achieve the SS POI again highlights its utility.

CONCLUSIONS

Efforts have been extended to develop the theory surrounding stochastic neutron chains as well as divergent chain buildup. Solutions were developed for a 0-D system to understand divergent chain buildup and eventually how long it takes for this buildup to occur. The fundamental quantity of interest, the non-extinction probability, has been thoroughly investigated for systems of interest as well as those outside of the desired phase space. The importance of the dynamic reactivity insertion was investigated, including the impact of a source. When the 0-D results were extended to a SPR type of system, parameters such as source strength, insertion time, and the maximum over-pulse were investigated. The theory shows that with some assumptions it can be used to determine the maximum pulse achievable on the fast burst type of reactor.

A 0-D Monte Carlo code was written to allow for divergent chain buildup. Excellent agreement is found between the results and the theory. In addition, the Monte Carlo results were able to provide additional time dependent behavior that the deterministic results could not. Although the code was viable for allowing divergent chains to buildup, computational time proved to be a daunting task.

The deterministic work was extended to examination of a 1-D slab system. Time dependent solutions were found for both static and dynamic reactivity. Multiple iteration routines were developed for investigation of numerical convergence. The standard fixed point iteration routine was robust to solve the problems of interest, yet suffered large

iteration counts. A modified lagged routine was developed which pulled the non-linear terms into an outer iteration and then held them fixed over the inner sweep. The iteration count was shown to improve for certain regions. To examine the numerical performance and to investigate the potential for an acceleration scheme, a linearized routine was developed. The spectral radius for the standard cases was shown to be very close to one for the systems of interest. Given this, an acceleration scheme was developed. The theoretical spectral radius showed that offending mode was sufficiently suppressed such that acceleration should be guaranteed. For the first few timesteps this was generally true. It was found that while suppressing the offending mode in turn excited another mode causing the acceleration scheme to break down as the POI was approached. Once the acceleration loses its effectiveness, only marginal improvement was found in iteration counts, yet the decrease in simulation time was notable. While iteration counts are of interest, the real metric is the simulation run time. The acceleration of the linearized routine provided the fastest runtime and allowed all of the quadratic cases to converge which highlights the utility of the routine.

FUTURE WORK

It was shown previously that the acceleration scheme for the linearized routine lost effectiveness after multiple timesteps. The diffusion update should be further examined to see if the update can maintain its effectiveness. In addition, investigation of other acceleration routines should be pursued to see if unconditional convergence can be found. Since most production transport codes use similar routines to those outlined in this work, there is potential that such codes could be simply modified to solve a new class of problems. Although the non-extinction probability is non-linear, it was shown that by linearizing the equation that a modified source iteration routine could effectively solve the non-extinction equation.

Another area which warrants further investigation is to revisit the ratio of the linear to non-linear spatial solutions. Since the linear spatial solution well approximates the non-linear solution for marginally prompt critical systems, a systematic method to derive a 0-D equation from the 1-D solution at long times where the fundamental adjoint mode has developed is of interest. It was shown that the non-linear spatial mode is quickly developed such that solution of the spatial solution at each timestep may not be necessary. In other words, the mode does not change shape as a function of time, it merely relaxes to the SS POI. The time dependent importance may then be addressed through an enhanced point model which will allow for very fast simulation time.

Finally, a more extensive comparison should be provided to the SPR reactor. Some of the historical operating data gathered is presented in the subsequent appendix. Relating the experimental data to the solution for $P_N(t)$ can be performed by summing over N large enough to the point where an experimental pre-initiation occurs. Further efforts are warranted to relate the non-extinction probability to solutions for $P_N(t)$ and to understand the limitations of the relationship. In conclusion, an investigation is warranted for determining how well analytical and numerical solutions can be used to support future reactor designs with respect to pre-initiation to ensure safety while operating in the prompt critical regime.

LIST OF APPENDICES:

APPENDIX A: SPR OPERATIONS AND EXPERIMENT RECORDS

APPENDIX A: SPR OPERATIONS AND EXPERIMENT RECORDS

To support the theoretical analysis presented in this document, data mining efforts were performed for previous SPR-III operations. A number of data points were collected for free field operations as well as some with experiments. This appendix highlights a portion of the experimental information extracted from the operational history. As controlled experiments could not be performed due to reactor availability, the data should only be used to provide an indication of the behaviors presented. Unfortunately, there is too much uncertainty with the data for it to be a viable benchmark against the previous numerical results. Prior to examining the experimental data, some discussion is warranted.

A.1 Safety Basis Treatment

For relatively recent fast reactor machines, a safety basis document which authorized the operation of these machines was required to be developed to meet Department of Energy requirements. For both SPR and Super Kukla, the probability of initiation was addressed in the safety basis documents. Subsequent treatment in these documents is dramatically different and warrants some discussion. For SPR-III the pre-initiation rate described in the authorization basis document (Ford 2005) is treated through Hansen's paper and is only included to illustrate the phenomena (Hansen 1960). It is noted in the safety analysis report for SPR that with a ~ $32/sec addition rate, it could be feasible (assuming there is sufficient excess reactivity) to get a few dollars above prompt before the

likelihood of pre-initiation becomes dominant. The administratively controlled maximum pulse at SPR is limited to $1.126 which results in a temperature rise of 450°C with a cavity fluence of $6*10^{14}$ n/cm^2 (Ford 2005). The maximum over pulse as cited in the SPR safety basis is taken to be 40¢ above prompt (ρ = $1.40). At this large of a reactivity addition, certain portions of the core are assumed to vaporize; some becomes liquid while others stay solid. Nevertheless, a 40¢ pulse deposits ~132 MJ of energy locally in the fuel and results in significant core damage and potential down wind dispersal of fission products. It takes a reactivity insertion of ~$1.226 to reach the melting temperature of U-10Mo at 1130°C (Ford 2005). Development of a rock solid basis for the maximum over pulse is difficult. Even though the reactor could achieve over pulses worth several dollars of reactivity, it only takes a few cents of reactivity over the maximum yield to exceed both the thermal and shock limitations of these machines.

A.1.1 Super Kukla

Due to its tie to this work, it is useful to describe Super Kukla. The Super Kukla reactor was built to serve as an irradiation source using low enriched fuel. It consisted of an annular shell with additional optional end reflectors on the annulus. The reactor is nominally 37 inches tall, 6 inches thick, with an outer diameter of 30 inches. The fuel was built of 20% enriched uranium of 10% molybdenum alloy. The overall mass of the assembled reactor was approximately 4,500 kg. Reactivity adjustment on the reactor was offered by six fuel rods that fit into holes in the core. The maximum pulse was ~$4x10^{16}$ fissions in the core with a 500 μsec full-width at half-maximum which caused a peak

temperature rise in the fuel of ~280°C. The nominal pulse regime was ~5-15¢ prompt (Gilbert 1964).

During burst operation, the ganged rods could be inserted at speeds of 120 in/sec. In addition, the machine was able to accommodate experiments from -$10 to +$4. If there was insufficiently reactivity available, additional fuel could be added to the reactor to compensate (Gilbert 1964).

Super Kukla was operated by Lawrence Livermore National Laboratory (LLNL) at the Nevada Test Site from 1965-1978 (LLNL 2003). Due to its lower enrichment, the overall fissile mass needed to achieve the reactivity swings and pulse characteristics was rather large. Due to its large size Super Kukla had several issues. The first of these was that during a successful pulse, the reactor temperature rise was sufficient that it would take a long time to cool the massive core. Typically only one pulse per day was realized on the machine. In addition, it is known that Super Kukla suffered from a large pre-initiation problem. It is anticipated that this was due to the physical size of the system (rapid movement of heavy masses) as well as the background neutron source strength.

The Super Kukla safety basis document (Gilbert 1964) treats the pre-initiation probability as a simple decaying exponential with modified coefficients derived from Godiva. Discussion of Super Kukla is included in this work since the maximum over pulse is determined by a pre-initiation probability of 99.999%. At that high of a rate of pre-initiation, the largest over pulse credible for accident analysis was selected. This over

pulse, worth 52¢, determines the maximum energy input into the reactor and hence the amount of U-10Mo vaporized from the excursion. It should be pointed out that the pre-initiation probability was derived for free field conditions for the machine. It is readily known that irradiating objects can drastically change the behavior of the system as well as the pre-initiation probability. While the pre-initiation treatment for SPR was more geared towards supplying information about how the reactor operates, it is interesting that the safety case for Super Kukla was built around the pre-initiation probability. In order to support the large number of significant digits for the Super Kukla pre-initiation probability requirement, the safety basis document forces the machine to have a neutron source present of different magnitudes depending on the reactivity insertion rate that is in excess of the large background neutron source from spontaneous fission. The required source strength varied from $3\text{-}5*10^5$ n/s unmultiplied. With subcritical prompt multiplications of ~150, it is clear that neutron source strengths of 10^7 n/s were be realized.

A.2 SPR Experimental Results

It was already discussed that if a significant reactor power was reached prior to the limit switch being contacted, a pre-initiation is said to have occurred. At SPR this power limit is set to ~50 W. Operations staff set this as an upper limit which provides a clear indication of a pre-initiation. The overall magnitude of the power level is not important for operations. A high level was set to ensure that the reactor did indeed begin an excursion prior to full burst element insertion.

During a successful pulse operation, the burst element is fully inserted before the upper power level is reached. The reactor will stay assembled for a finite period of time prior to one of the neutrons in the assembly leading to a divergent chain. The length of time the reactor stays assembled is stochastic and depends on the level of neutrons originally in the machine and the system reactivity. If no neutrons were present, the reactor would stay assembled at this prompt critical state indefinitely until a "stray" neutron(s) would set it off. The background neutron rate for SPR is sufficiently high such that there are enough neutrons present to preclude the reactor staying assembled for any appreciable amount of time and are sufficiently low such that the full reactivity insertion can be realized without a pre-initiation. The longest recorded time for the reactor fully assembled and not reaching ~50 W at free field conditions was ~ 1.5 seconds. Once the prompt critical excursion has begun, the reactor ramps up in power very rapidly. A typical e-folding time for large insertions is ~30 μs. Upon ramping up in power, the fuel mass begins to expand radially. It is this radial expansion, temperature increase in the fuel, and subsequent increase in neutron leakage that causes the initial shutdown of the core. Subsequently the pulse element and safety block are also dropped via gravity to ensure an adequate shutdown margin. It should be noted that for large pulses, the axial expansion of the reactor core has been shown to initiate the safety block breakaway prior to the breakaway signal reaching the core. Thus for large insertions, the safety block "falls" faster than the pulse element.

These machines typically accommodate experiments of varying worths; the reactor must have available sufficient excess reactivity to overcome negative worth experiments. Although not credited as a safety feature of the SPR reactor, it has been questioned in the past if it is possible to design a reactor system such that there is an upper limit on the reactivity state that can be achieved before the reactor pre-initiates (similar to how Super Kukla was treated). Experience has shown that for past FBR designs (Godiva and SPR-II specifically), the reactor is able to achieve significantly high powers such that some reactor disassembly occurs prior to pre-initiation becoming a dominant player (Wimett 1956, Jefferson 1969). For the SPR-II reactor, the machine was taken to excess power levels in an attempt to determine the maximum operating range for the machine. A burst yielding a ΔT of 606°C was sufficient to cause fracturing of the fuel plates. Typical large yield pulses on SPR-III of \$1.10 result in a ΔT of ~300°C. It is well known that systems with appreciable reactivity insertions that additional excess reactivity could be added to mechanically stress the machines. The primary means of then precluding an over insertion of reactivity would be to either limit the excess reactivity or from a pre-initiation perspective slow the insertion down, and/or increase the effective background source.

A.2.1 Free Field Experiments

Limited values derived from SPR operation are presented in the table below for free field pulses. The mean time to initiate the pulse (from all pulses in the range) as well as the standard deviation are shown. The mean time represents the length of time the reactor sat at prompt critical prior to the pulse ensuing.

Table 20: Mean time to initiate a pulse v. pulse size.

Pulse Size	Number	Mean Time (ms)	Standard Deviation (ms)
100.0-100.9	19	498.7	317.3
101.0-101.9	9	512.9	452.6
102.0-102.9	15	342.2	303.2
103.0-103.9	29	395.6	316.5
104.0-104.9	7	309.7	247.7
105.0-105.9	18	221.8	198.7
106.0-106.9	18	237.0	178.5
107.0-107.9	13	339.2	243.3
108.0-108.9	33	240.3	240.0
109.0-109.9	77	151.5	187.4
110.0-110.9	13	263.5	305.1
Total	251		

Even pulse ranges that had a large number of entries (i.e. the 9¢ pulse range) had a standard deviation that was sufficiently large (in fact larger than the mean). Due to the limited number of data points it is difficult to assess whether the standard deviation is a good value. Namely with an infinite number of data points it is known that there will still be a substantial variance about the mean (particularly at low reactivity states). One cannot tell if the large standard deviation presented is due to the true variance or simply due to limited data points. A general trend can be observed from the data such that the mean time to initiate a pulse is larger for slightly prompt critical pulses compared to the

larger pulses. Given that the insertion speed and reflector worth are fixed, the decrease in mean time can be attributed to the fact that the reactor is initially more subcritical for the smaller pulses and that there is substantially more multiplication for higher reactivity states.

As a part of the effort to better understand the pre-initiation probability at SPR, efforts were extended to examine previous operating histories for free field conditions. A significant amount of data has been recorded for the > 13,000 operations on the reactor. Due to the low number of pre-initiations in the reactor for free field conditions it was not feasible to derive an experimental pre-initiation probability for free field conditions for all operating reactivity states. For the entire set of free field pulses performed for SPR from 1985-2008, the figure below plots the reactivity state of the reactor as well as the assembly time at that reactivity state for free field conditions.

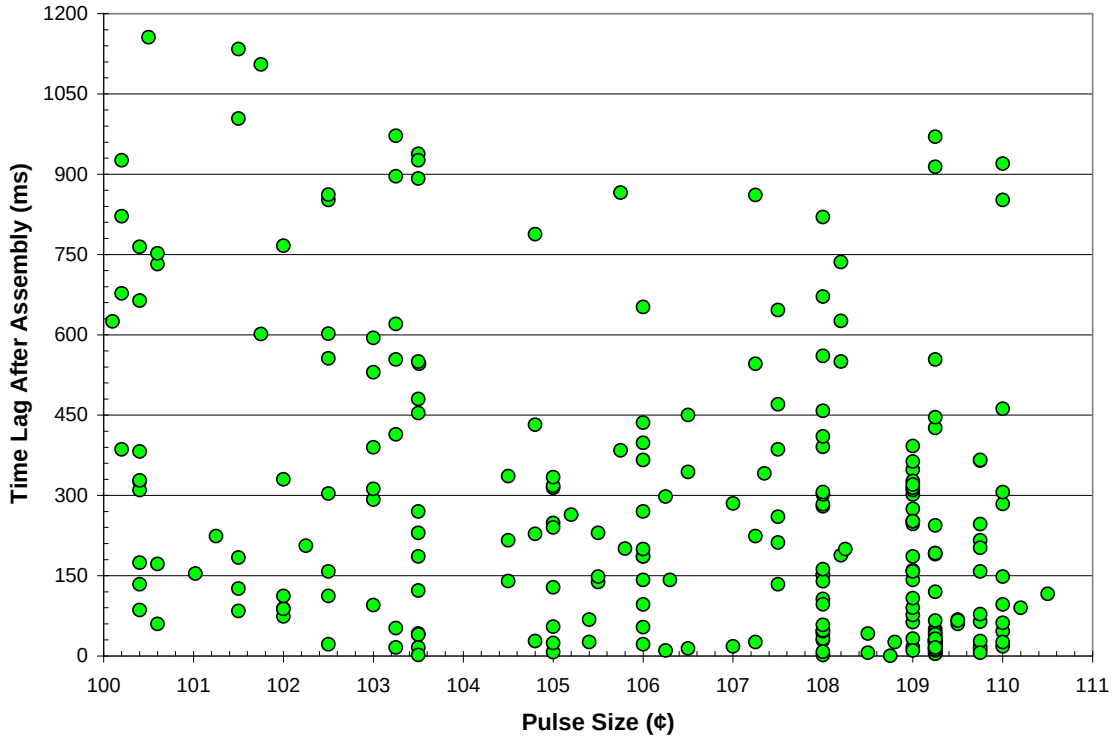

Figure 59: Pulse size v. time lag after assembly for free field conditions.

It can be seen by the scatter plot above that the data are spread over various reactivity states. For examination of the data in Figure 59, the pulse data was broken into 1¢ intervals. The columns with experiment descriptions will be addressed later in further detail and are included here for organization.

Table 21: Group binning for assembly time distribution curves.

Group Number	Pulse Size (cents)	Number in Bin			
		Free Field	Exp. Type I w/ Poly	Exp. Type I w/o Poly	Exp. Type II
1	100.0 – 100.9	19	1	0	0
2	101.0 – 101.9	9	0	0	0
3	102.0 – 102.9	15	0	0	0
4	103.0 – 103.9	29	29	4	0
5	104.0 – 104.9	7	55	20	0
6	105.0 – 105.9	18	172	21	0
7	106.0 – 106.9	18	99	23	0
8	107.0 – 107.9	13	91	45	0
9	108.0 – 108.9	33	20	36	0
10	109.0 – 109.9	77	33	13	155
11	110.0 – 110.9	13	13	79	0
12	111.0 – 111.9	0	6	94	0
13	112.0 – 112.9	0	7	101	0
14	113.0 – 113.9	0	25	4	0
15	114.0 – 114.9	0	62	6	0
16	115.0 – 115.9	0	1	75	0
17	116.0 – 116.9	0	9	0	0
18	117.0 – 117.9	0	1	0	0
19	118.0 – 118.9	0	2	0	0
TOTAL:		251	626	521	155

With the available data for free field pulses, one is able to determine the probability that the reactor did not pre-initiate for a given reactivity state during the pulse element insertion time. As the reactivity state of the reactor increases, the probability that the reactor will pre-initiate increases. To some extent this trend can be observed in the data presented above. Of the available data, these have been translated to normalized probability distribution curves for different reactivity states. For time frames of interest, multiple bins were selected. The number of pulses that resided in that bin was recorded. Each bin was then normalized to the total number of points (area under the curve is one). It was determined that about 7 time bins spread over 1200 ms was sufficient to capture

enough detail. Of the data presented in Figure 59, there are only a few reactivity states which contain sufficient information to be useful.

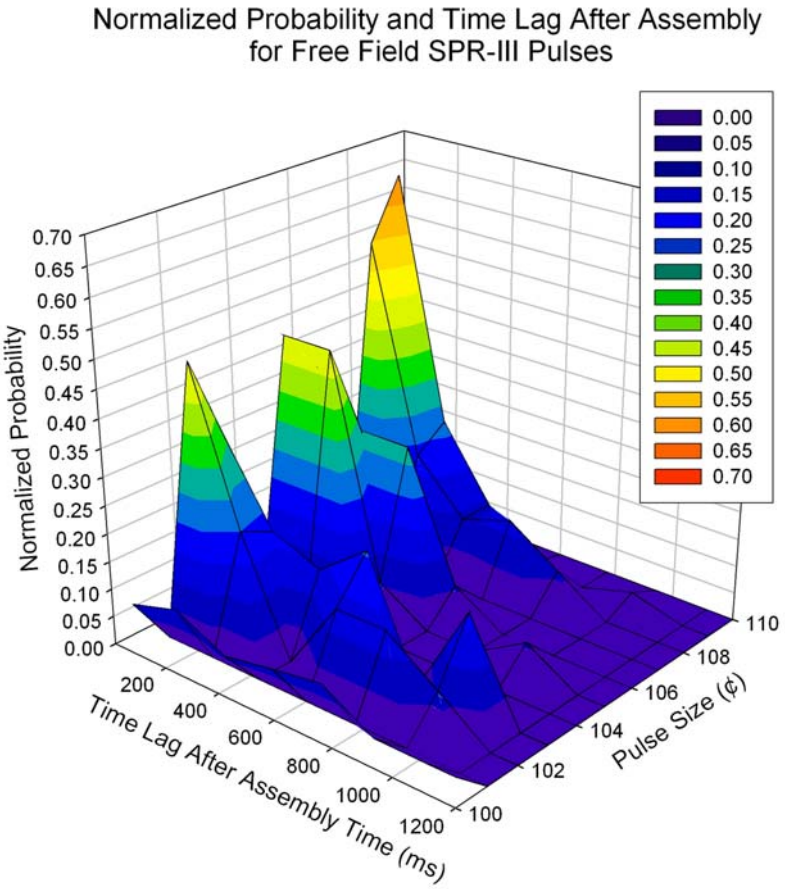

Figure 60: Normalized probability time lag after assembly v. reactivity state for free field conditions.

The vertical axis, Normalized Probability, refers to the normalized probability that for a given reactivity state how long the reactor sat before the ~50 W power limit was reached. For the reactivity states that are shown, a few interesting details can be deciphered. In particular, at low reactivity states, it appears that the normalized probability has an exponential shape with a long decaying tail. As the system reactivity increases, this tail rapidly drops off and the probability of the machine staying assembled for long periods of

time drops off quickly. In addition, for short time frames, it appears that there is a dependence on the probability from the reactivity state. As the reactivity goes up, this probability becomes much sharper and implies that for large insertions (similar to that assumed in the safety basis document of $1.40) that it would be exceedingly difficult to reach that reactivity state before the machine would pre-initiate and terminate the pulse.

A.2.2 Generic Experiments

For the discussion to be complete, it is of interest to examine the large bodies of experiments that were performed as well. Although this information does not describe free field conditions, it does relate how the reactor behaves under experimental conditions. If future systems are built, free field conditions may not be indicative of the reactor performance and hence the pre-initiation probability. In fact, as indicated previously, most operations on these machines do not meet free field conditions. The focus of this section is to show that with pre-initiation probabilities derived for free field conditions, additional efforts are required for bounding experiments. The details of the experiments presented below are unimportant; however, there were two types of experiments that were performed in large numbers over various reactivity states. One type of experiment, named Type I, had two variations with similar test setups. One case involved the use of a large piece of polyethylene and the other did not. As such, these experiments are valid for comparison. The overall worth of the experiment without the poly was ~ 130-160¢ and the experiment with the poly was worth ~ -210-240¢. The other configuration, named Type II, was worth ~ 45-85¢ and involved a completely

separate experiment setup and materials. There is no relation between Type I and Type II experiments. The distribution of data for these experiments is shown in Figure 60 above.

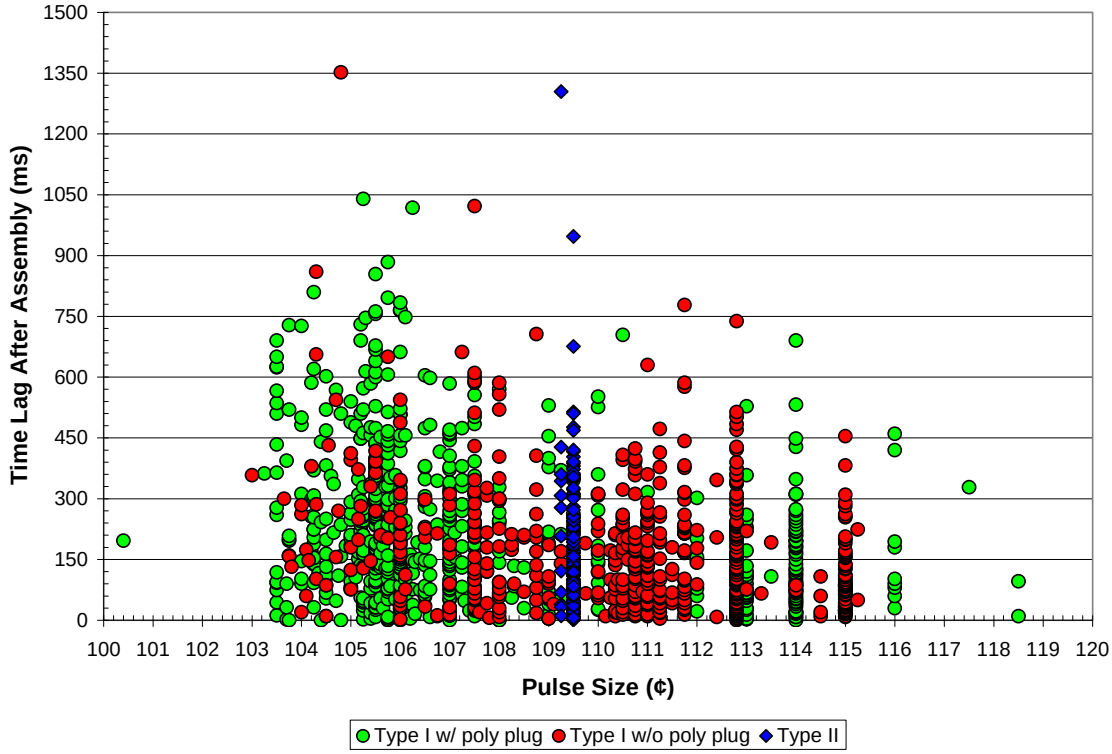

Figure 61: Pulse size v. time lag after assembly for experiments with a large repetition rate.

Each data point above was an individual pulse operation; for details on the grouping see Table 21. To illustrate the difference between free field and experiment conditions, 2-D contour plots are presented below. For bins that had few data points (like bin 100-100.9 for the Type I experiments) they have been removed.

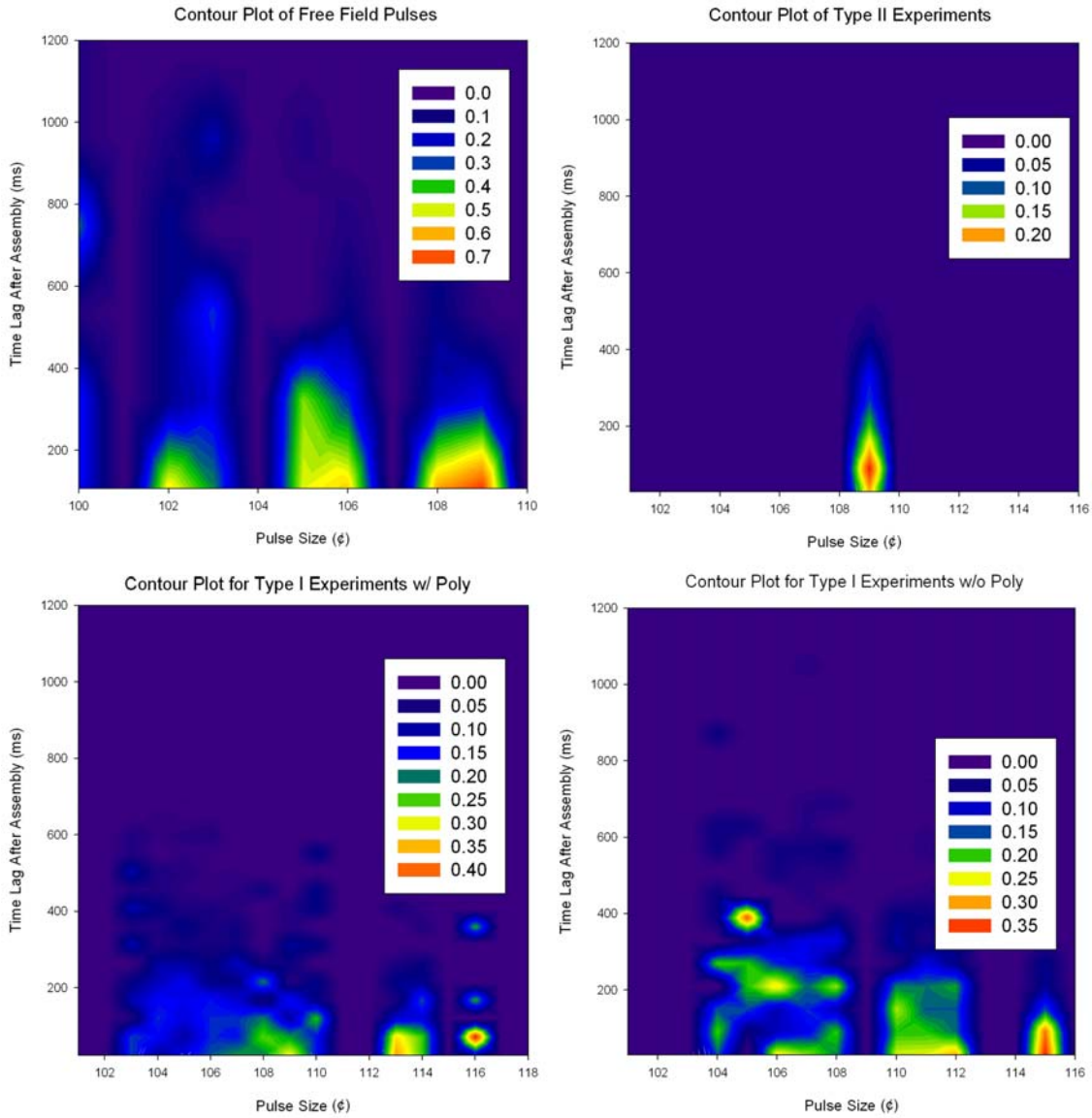

Figure 62: 2-D contour plots of the time lag after assembly for various experiments.

From the contour plots, a discernable difference between the free field results and the three experiments shown. For free field conditions, the assembly time distribution appears to have a decaying exponential shape as reactivity increases. For the Type II experiment plot, there appears to be a less subtle shift in probabilities as reactivity increases. For the two experiments with and without poly, there are striking differences.

The case without the poly has a longer probability tail at higher reactivities states and the case with poly has a gentler shift.

The important feature to gather from the plots is that there differences between themselves. This was not a large surprise as items irradiated with the reactor tend to modify the operational characteristics (neutron lifetime, pulse size, reactor period). Take for example the large pulse sizes seen for the bottom two experiments in Figure 62. Notice the change between the Type I experiments with and without the polyethylene. As low Z materials act as neutron moderators, it is anticipated that higher reactivities could be achieved due to the longer neutron lifetimes. The difference amongst the plots illustrates the point that if reactor designers are concerned with pre-initiation (especially for developing the safety case for it), examining the free field condition may not be indicative of how the reactor will operate with an experiment.

A.3 Experimental Data Conclusions

During the development of this work, it was desired to develop an experimental benchmark for SPR-III operation to compare it against theoretical results. Due to limited reactor availability, these measurements could not be performed. The data presented above were included to provide the reader with an overall understanding of how the theoretical results could be used to compare against reactor measurements. Since controlled experiments could not be performed to compare the theory against, no attempt was made to correlate the two.

REFERENCES

Adams, Marvin L., and Larsen, Edward W., "Fast Iterative Methods for Discrete-Ordinates Particle Transport Calculations", *Progress in Nuclear Energy*, Vol. 40, No. 1, pg 3-159, 2002.

Alcouffe, R. E., "Diffusion Synthetic Acceleration Methods for Diamond-Differenced Discrete-Ordinates Equations", *Nuclear Science and Engineering*, Vol. 65, pg 344-355, 1977.

Baker, R., "Probability of Initiation (POI)", LA-UR-04-6589, June 1, 2005.

Barlett, M. S., An Introduction to Stochastic Processes with Special Reference to Methods and Applications, 3rd ed., Cambridge University Press, Cambridge, 1978.

Bell, George I., "Probability Distribution of Neutrons and Precursors in a Multiplying Assembly", *Annals of Physics*, Vol. 21, pg. 243-283, 1963.

Bell, George, I., "On the Stochastic Theory of Neutron Transport", *Nuclear Science and Engineering*, Vol. 21, pg. 390-401, 1965.

Bell, George, I, and Lee, Clarence E., "On the Probability of Initiating a Persistent Fission Chain", LA-2608, April 1976.

Bell, George, and Glasstone, Samuel, Nuclear Reactor Theory, Reinhold Company, New York, 1970.

Brown, Forrest B., "Fundamentals of Monte Carlo Transport – Collision Physics – Lecture 5", February 2006.

Brown, Forrest B., "Fundamentals of Monte Carlo Transport – Tallies and Statistics – Lecture 6", February 2006.

Courant, E. D., and Wallace, P.R., "Fluctuations of the Number of Neutrons in a Pile", *Physical Review*, Vol 72, No. 11, December 1947.

Diven, B.C., et. al., "Multiplicities of Fission Neutrons", *Physical Review*, Vol. 101, No. 3, February 1, 1956.

Duderstadt, James J., and Hamilton, Louis, J., Nuclear Reactor Analysis, John Wiley & Sons, New York, 1976.

Etherington, H., Nuclear Engineering Handbook, McGraw-Hill Book Company, New York, 1958.

Feller, William, An Introduction to Probability Theory and Its Applications, Vol. 1, 3rd Ed., New York, John Wiley & Sons, 1968.

Feynman, R.P., "Statistical Behavior of Neutron Chains", LA-591(DEL), Los Alamos Scientific Laboratory July 26, 1946.

Ford, J.T, et. al., "Safety Analysis Report (SAR) for the Sandia Pulsed Reactor Facility (SPRF)", SAND2005-4187, Official Use Only, July 2005.

Ford, J. T., private communication, 2008.

Frehaut, J., "Neutron Multiplicity Distribution in Fast Neutron-Induced Fission", *IAEA Consultants Meeting on Physics of Neutron Emission in Fission*, Mito, Japan, May 1988.

Frisch, O. R., "The Dragon Experiment", *Fast Burst Reactors, Proceedings of the National Topical Meeting on Fast Burst Reactors*, American Nuclear Society, host at The University of New Mexico, Albuquerque, January 1969.

Gilbert, W.S., et. al., "Revised Safety Analysis Report for the Super Kukla Prompt Burst Reactor", Lawrence Radiation Laboratory, Livermore CA, UCRL-7695, Rev. I, February 4, 1964.

Greenman, Gregory, et. al., "A Monte Carlo Method for Calculating Initiation Probability", *Joint International Topical Meeting on Mathematics & Computation and Supercomputing in Nuclear Applications*, 2007.

Gregson, Michael, and Prinja, Anil, "Time Dependent Non-Extinction Probability for Fast Burst Reactors", *Transactions of the American Nuclear Society*, Vol. 98, pg. 533, 2008.

Hansen, G. E., "Assembly of Fissional Material in the Presence of a Weak Neutron Source", *Nuclear Science and Engineering*, Vol. 8, pg. 709-719, 1960.

Harris, D.R.**,** Analysis of Reactor Fluctuations. American Nuclear Society. Volume 4, Number2, November 1961

Harris, T.E., Branching Phenomena, Springer-Verlag, Berlin, 1963.

Harris, T.E., The Theory of Branching Processes, 1989

Holden, Norman E. and Zucker, Martin S., "Prompt Neutron Emission Multiplicity Distribution and Average Values (Nubar) at 2200 m/s for the Fissile Nuclides", *Nuclear Science and Engineering*, 98, pg 174-181, 1988.

Humbert, Philippe, "Stochastic Neutrons with PANDA Deterministic Code", *Nuclear Mathematical and Computational Sciences: A Century in Review, A Century Anew*, American Nuclear Society, Gatlinburg, Tennessee, April 6-11, 2003.

Humbert, Philippe, "Numerical Solution for Stochastic Neutronic Point Model", *Transactions of the American Nuclear Society*, Vol. 83, 2000.

Humbert, Philippe & Méchitoua, Boukhmes**, "**Simulation of Caliban Reactor Burst Wait Time and Initiation Probability Using a Point Reactor Model and PANDA code", *PHYSOR 2004 – The Physics of Fuel Cycles and Advanced Nuclear Systems: Global Developments*, Chicago, IL, 2004.

Jefferson, R.M., "Sandia Pulse Reactor II", *Fast Burst Reactors, Proceedings of the National Topical Meeting on Fast Burst Reactors*, American Nuclear Society, host at The University of New Mexico, Albuquerque, January 1969.

LA-UR-03-1987, MCNP – A General Monte Carlo N-Particle Transport Code, Version 5, X-5 Monte Carlo Team, April 2003.

Lamarsh, John R, and Baratta, Anthony J., Introduction to Nuclear Engineering, 3rd Ed., Prentice Hall, New Jersey, 2001.

Jefferson, R.M., "Sandia Pulse Reactor II", *Fast Burst Reactors, Proceedings of the National Topical Meeting on Fast Burst Reactors*, American Nuclear Society, host at The University of New Mexico, Albuquerque, January 1969.

Larsen, Edward W., "Diffusion-Synthetic Acceleration Methods for the Discrete-Ordinates Equations", (LA-UR-82-3581), *Mathematics and Computation Division Topical Meeting, American Nuclear Society*, Salt Lake City, Utah, March 28-31, 1983.

Larsen, Edward W., "Unconditionally Stable Diffusion-Synthetic Acceleration Methods for the Slab Geometry Discrete Ordinates Equations. Part I: Theory", *Nuclear Science and Engineering*, vol. 82, pg. 47-63, 1982.

Lawrence Livermore National Laboratory, "Knowing the Enemy, Anticipating the Threat", UCRL-WEB-147539, July 8, 2003.
http://www.llnl.gov/50science/threat.html

Lewins, Jeffrey, "The Time-Dependent Importance of Neutrons and Precursors", *Nuclear Science and Engineering*, Vol 7., pg 268-274, 1960.

Lewins, Jeffrey, "Variation Representations in Reactor Physics Derived from a Physical Principle", *Nuclear Science and Engineering*, Vol. 8, pg 95-104, 1960.

Lewins, Jeffrey, "Variational Method in Neutron Stochastics", *Annals of Nuclear Energy*, Vol. 5, pg 141-157, 1978.

Lewins, J. D, "Stochastic Distribution of Prompt Neutrons in a Super-Critical Reactor", *Journal of Nuclear Energy*, Vol 8, p 15-28, 1981.

MacMillan D. B., "Probability Distribution of Neutron Populations in a Multiplying Assembly", *Nuclear Science and Engineering*, Vol. 39, pg. 329-336, 1970.

Méchitoua, Boukhmes, "Monte Carlo Estimation of Nonextinction Probabilities", *Transactions of the American Nuclear Society*, Vol. 82, 2000.

Nolen, Steven, "The Chain-Length Distribution in Subcritical Systems", LA-13721-T, June 2000.

Ott, K.O., et. al., Introductory Nuclear Reactor Dynamics, American Nuclear Society, La Grange Park, IL, 1985.

Pal, L., Statistical Theory of Chain. Acta Physica Academia, Vol 14, pg 345, 1962.

Press, William H., et. al., Numerical Recipes in FORTRAN 77, The Art of Scientific Computing, Volume 1, 2nd Ed., Cambridge University Press, 1986.

Reactor Physics Constants, ANL-5800.

Terrell, J., "Distributions of Fission Neutron Numbers," *Physical Review*, Vol. 108., pg. 783, 1957.

Williams, M.M.R., Random Processes in Nuclear Reactors, Pergamon Press, Oxford, New York, 1974.

Williams, M. M. R., "An Exact Solution of the Extinction Problem in Supercritical Multiplying Systems", *Annals of Nuclear Energy*, Vol. 6., pg 463-472, 1979.

Williams, M.M.R., "The extinction problem in a super-critical sphere of fissile material", Annals of Nuclear Energy, Vol. 31, pg 933, 2004.

Warsa, J.S., et. al, "Diffusion Synthetic Acceleration – Part 1: Deficiencies in Multi-Dimensional Heterogeneous Problems", LA-UR-02-0345.

Wimett, T.F., “Time Behavior of Godiva Through Prompt Critical”, LA-2029, May 1, 1956.

Wimett, T.F., “Godiva II-An Unmoderated Pulse-Irradiation Reactor”, *Nuclear Science and Engineering*, Vol 8, pg. 691-708, 1960.